



Real-time, experimental characterization/investigation of hot-spots in shocked heterogeneous materials

**Hergen Eilers
WASHINGTON STATE UNIVERSITY**

**12/13/2019
Final Report**

DISTRIBUTION A: Distribution approved for public release.

**Air Force Research Laboratory
AF Office Of Scientific Research (AFOSR)/ RTA1
Arlington, Virginia 22203
Air Force Materiel Command**

DISTRIBUTION A: Distribution approved for public release

REPORT DOCUMENTATION PAGE			<i>Form Approved</i> <i>OMB No. 0704-0188</i>		
<p>The public reporting burden for this collection of information is estimated to average 1 hour per response, including the time for reviewing instructions, searching existing data sources, gathering and maintaining the data needed, and completing and reviewing the collection of information. Send comments regarding this burden estimate or any other aspect of this collection of information, including suggestions for reducing the burden, to Department of Defense, Executive Services, Directorate (0704-0188). Respondents should be aware that notwithstanding any other provision of law, no person shall be subject to any penalty for failing to comply with a collection of information if it does not display a currently valid OMB control number.</p> <p>PLEASE DO NOT RETURN YOUR FORM TO THE ABOVE ORGANIZATION.</p>					
1. REPORT DATE (DD-MM-YYYY) 16-06-2020		2. REPORT TYPE Final Performance		3. DATES COVERED (From - To) 30 Sep 2015 to 29 Sep 2019	
4. TITLE AND SUBTITLE Real-time, experimental characterization/investigation of hot-spots in shocked heterogeneous materials			5a. CONTRACT NUMBER		
			5b. GRANT NUMBER FA9550-15-1-0309		
			5c. PROGRAM ELEMENT NUMBER 61102F		
6. AUTHOR(S) Hergen Eilers			5d. PROJECT NUMBER		
			5e. TASK NUMBER		
			5f. WORK UNIT NUMBER		
7. PERFORMING ORGANIZATION NAME(S) AND ADDRESS(ES) WASHINGTON STATE UNIVERSITY 240 FRENCH ADMINISTRATION BLDG PULLMAN, WA 99164-2752 US				8. PERFORMING ORGANIZATION REPORT NUMBER	
9. SPONSORING/MONITORING AGENCY NAME(S) AND ADDRESS(ES) AF Office of Scientific Research 875 N. Randolph St. Room 3112 Arlington, VA 22203				10. SPONSOR/MONITOR'S ACRONYM(S) AFRL/AFOSR RTA1	
				11. SPONSOR/MONITOR'S REPORT NUMBER(S) AFRL-AFOSR-VA-TR-2020-0014	
12. DISTRIBUTION/AVAILABILITY STATEMENT A DISTRIBUTION UNLIMITED: PB Public Release					
13. SUPPLEMENTARY NOTES					
14. ABSTRACT To determine the feasibility of temperature measurements in heterogeneous materials under dynamic compression, we designed and synthesized various sensor materials and investigated their properties. The sensors consist of molecular complexes containing trivalent lanthanide ions such as Dy3+ and various organic ligands. The 2-color fluorescence properties of Dy3+ provide the temperature sensing capability. The ligands serve to: enhance the absorption of UV light; allow for the growth of molecular crystals; and allow for dispersion in a polymer matrix. The sensors have been designed so that they can easily be excited by 355 nm laser light, have a high emission intensity over a wide range of temperatures, and have a fluorescence lifetime of at least 10 s. Such a lifetime allows us to excite the sensor with a single laser shot and transfer all the energy to the lanthanide ion right before the shock hits and deforms the molecular ligand structure					
15. SUBJECT TERMS explosive, mesoscale temperature measurement					
16. SECURITY CLASSIFICATION OF:			17. LIMITATION OF ABSTRACT UU	18. NUMBER OF PAGES	19a. NAME OF RESPONSIBLE PERSON SCHMIDT, MARTIN
a. REPORT Unclassified	b. ABSTRACT Unclassified	c. THIS PAGE Unclassified			19b. TELEPHONE NUMBER (include area code) 703-588-8436

FINAL REPORT

Real-time, experimental characterization/investigation of hot-spots in shocked heterogeneous materials

FA9550-15-1-0309

Principle Investigator:

Dr. Hergen Eilers
Washington State University
ISP/Applied Sciences Laboratory
Department of Physics and
Astronomy
PO Box 1495
Spokane, WA 99210-1495
Tel.: 509-358-7681
Fax: 509-358-7728
Eilers@wsu.edu

Prepared for:

Dr. Martin J. Schmidt
martin.schmidt@us.af.mil
850-883-2686

Submission Date: 12/13/2019

Contributors to this work include Benjamin R. Anderson, Natalie Gese, Ray Gunawidjaja, Yogendra Gupta, Michael Mark, Yoshimasa Toyoda, Mike Winey, and Kurt Zimmerman.

I. ABSTRACT

To determine the feasibility of temperature measurements in heterogeneous materials under dynamic compression, we designed and synthesized various sensor materials and investigated their properties. The sensors consist of molecular complexes containing trivalent lanthanide ions such as Dy^{3+} and various organic ligands. The 2-color fluorescence properties of Dy^{3+} provide the temperature sensing capability. The ligands serve to: enhance the absorption of UV light; allow for the growth of molecular crystals; and allow for dispersion in a polymer matrix. The sensors have been designed so that they can easily be excited by 355 nm laser light, have a high emission intensity over a wide range of temperatures, and have a fluorescence lifetime of at least 10 μs . Such a lifetime allows us to excite the sensor with a single laser shot and transfer all the energy to the lanthanide ion right before the shock hits and deforms the molecular ligand structure. Shock compression experiments were performed using a single-stage gas gun (2.5" bore), designed to reach peak stresses of up to 9 GPa. We observed photoluminescence and were able to determine the 2-color intensity ratios for about 2 μs after the shock entered the sample, which is long enough for the proposed application of these temperature sensors. Converting the intensity ratios into absolute temperatures is currently limited by the unknown effect of dynamic pressure on the population of the two excited states. However, relative temperature comparisons might be possible in locations that are subject to the same pressure.

TABLE OF CONTENTS

I. ABSTRACT.....	2
II. BACKGROUND.....	10
III. OBJECTIVES.....	11
IV. APPROACH.....	11
V. ACCOMPLISHMENTS.....	13
A. Overview.....	13
B. Binders.....	14
C. Molecular Crystal Sensors.....	15
Dy(acac) ₃ (phen).....	15
Dy(Acac) ₃ (DPEPO).....	20
Dy(4-BBA) ₃ (TPPO) ₂	22
Dy(PBI) ₃ (DPEPO).....	24
Dy:Y(hfa) ₃ (DPEPO).....	24
D. Molecular Dye Sensors.....	27
Sm(acac) ₃ (TOPO) ₂	27
Sm(acac) ₃	29
Dy(acac) ₃	31
Sm(2-ethyl hexanoate) ₃	32
Sm(hfa) ₃ (TOPO).....	32
Dy(acac) ₃ (TOPO) ₂ and Dy(hfa) ₃ (TOPO) ₂	35
E. Initial Temperature Measurements.....	40
F. Initial Imaging.....	40
G. Two-Color Thermometry Imaging.....	41
System Setup.....	41
Room Temperature Imaging.....	43
Laser Heating Tests.....	45
H. Upgraded TCTI system.....	49
Pulsed Laser TCTI Demonstration.....	49
I. Shock Measurements.....	56
2017 Shots.....	56
Developing Alternative Materials for Shock Experiments.....	61
2018 Shock Experiments.....	70

2019 Shock Experiments.....	76
J. Project Publications and Presentations.....	83
VI. SUMMARY.....	84
VII. APPENDECIES.....	86
A. CCl ₄ Raman Measurement Tests Notes.....	86
VIII. REFERENCES.....	89

TABLE OF FIGURES

Figure 1. Transparent samples of all three binders (top left), Clear Flex 50 samples containing temperature sensors (bottom left), and magnified image of molecular crystal sensors embedded in binder (right).....	14
Figure 2. Optical absorption of potential binder materials.....	15
Figure 3. UV (254 nm) illuminated epoxy and HTPB/IPDI/DOA binder samples containing thermosensors.	15
Figure 4. Molecular structure of Dy(acac) ₃ (phen).....	15
Figure 5. Optical image (left) and x-ray diffraction pattern of Dy(acac) ₃ (phen).....	16
Figure 6. FTIR spectra of acac, phen, and Dy(acac) ₃ (phen).	16
Figure 7. Optical image of Dy(acac) ₃ (phen) illuminated by 254 nm light.	16
Figure 8. Absorbance of HTPB and Dy(acac) ₃ (phen) in HTPB (left), and Dy(acac) ₃ (phen) (right).....	17
Figure 9. Temperature-dependent emission spectra of Dy(acac) ₃ (phen) (left) and of Dy(acac) ₃ (phen) in HTPB (center). Normalized emission spectrum of Y(acac) ₃ (phen) showing the ligand background emission for 355 nm excitation.....	17
Figure 10. Temperature-dependent fluorescence lifetimes of pure Dy(acac) ₃ (phen) in HTPB at 481 nm.....	18
Figure 11. Emission intensity of Dy _{0.1} Y _{0.9} (acac) ₃ (phen) at 575 nm as a function of UV exposure time at room-temperature.	18
Figure 12. Emission spectra of Dy/Y(acac) ₃ (phen) for different concentrations, without (left) and with (right) gated detection.....	18
Figure 13. Time-resolved emission of Dy/Y(acac) ₃ (phen) at 482 nm (left) and 575 nm (center) for different concentrations. Also shown are the relative intensities and lifetimes at 482 nm as a function of Dy concentration (right).....	19
Figure 14. Temperature dependent emission intensity (left) at 484 nm, normalized to T = 293 K value, and ratio of integrated peak intensities (center) for peaks centered at 453 nm (450 nm - 460 nm) and 481 nm (462 nm – 504 nm). Fluorescence lifetimes of 10:90 Dy/Y(acac) ₃ (phen) at 482 nm and 575 nm.	19
Figure 15. Molecular structure of Dy(acac) ₃ (DPEPO).	20
Figure 16. Microscope image (left) and optical image for illumination with 254 nm (right) of Dy(acac) ₃ (DPEPO).....	21
Figure 17. Temperature-dependent emission spectra (left), emission intensities (center), and integrated ratio (right) of Dy(acac) ₃ (DPEPO).....	21
Figure 18. Molecular structure of Dy(4-BBA) ₃ (TPPO) ₂	22
Figure 19. Optical image (left) and x-ray diffraction pattern of Dy(acac) ₃ (phen).	22
Figure 20. FTIR spectra of 4-BBA, TPPO, and Dy(4-BBA) ₃ (TPPO) ₂	23
Figure 21. Optical image of Dy(4-BBA) ₃ (TPPO) ₂ illuminated by 254 nm light.	23
Figure 22. Temperature-dependent emission spectra (left), emission intensities (center), and integrated ration of Dy(4-BBA) ₃ (TPPO) ₂	23
Figure 23. Schematic of Dy:Y(hfa) ₃ (DPEPO)'s chemical structure.....	24
Figure 24. Emission spectra of Dy:Y(hfa) ₃ (DPEPO) at different temperatures.....	25
Figure 25. Normalized intensity at 482 nm as a function of time for Dy:Y(hfa) ₃ (DPEPO) and	25

Figure 26. Intensity at 482 nm as a function of temperature for Dy:Y(hfa) ₃ (DPEPO) with the intensity normalized such that the room temperature intensity is unity.....	26
Figure 27. Integrated intensity ratio (455 nm/482 nm) as a function of inverse temperature with an exponential fit.....	27
Figure 28. Molecular structure of Sm(acac) ₃ (TOPO) ₂	27
Figure 29. Microscope image of Sm(acac) ₃ (TOPO) ₂	27
Figure 30. FTIR of Sm(acac) ₃ (TOPO) ₂	28
Figure 31. Sm(acac) ₃ (TOPO) ₂ illuminated by 254 nm radiation.....	28
Figure 32. Temperature dependent emission spectra (left), emission intensities at 566 nm (center), and integrated 535 nm/566 nm ratio (right) of pure Sm(acac) ₃ (TOPO) ₂ ...	28
Figure 33. Temperature dependent emission spectra (left), emission intensities (center), and integrated ratio (right) of Sm(acac) ₃ (TOPO) ₂ dissolved in HTPB.	29
Figure 34. Molecular structure of Sm(acac) ₃	30
Figure 35. Microscope image of Sm(acac) ₃	30
Figure 36. FTIR of Sm(acac) ₃	30
Figure 37. Image of Sm(acac) ₃ irradiated by 254 nm light.....	30
Figure 38. Temperature-dependent emission spectra (left), emission intensities (center), and integrated 535 nm/566 nm ratio (right) of Sm(acac) ₃ in HTPB.	30
Figure 39. Molecular structure of Dy(acac) ₃	31
Figure 40. Microscope image of Dy(acac) ₃	31
Figure 41. FTIR of Dy(acac) ₃	31
Figure 42. Image of Dy(acac) ₃ irradiated by 254 nm light.....	31
Figure 43. Temperature-dependent emission spectra (left), emission intensities (center), and integrated ratio (right) of Dy(acac) ₃ in HTPB.	32
Figure 44. Schematic of Sm(acac) ₃ (TOPO).	32
Figure 45. Normalized intensity at 648 nm as a function of time for Sm(hfa) ₃ (TOPO) ₂ and Sm(acac) ₃ (TOPO) ₂	33
Figure 46. Emission spectra of SHT/HTPB for different temperatures.	34
Figure 47. (a) Normalized intensity as a function of temperature and (b) the integrated intensity ratio (545/650) as a function of inverse temperature.....	34
Figure 48. Schematic of the chemical structure of DAT (a) and DHT (b).....	35
Figure 49. FTIR spectra of: (a) insoluble part and (b) soluble part of Dy(Acac) _x (TOPO) _y	36
Figure 50. (a) SHT, rgAFOSR77-45 (left), and DHT, rgAFOSR124-101 (right) samples. (b) The corresponding FTIR spectra.	36
Figure 51. PL spectra (excited using 355 nm) of different Dy dyes doped into CCl ₄ with a concentration of 5 wt%.	37
Figure 52. PL spectra (using 355 nm excitation) for different concentrations of DAT in CCl ₄ . Inset: Intensity at 579 nm as a function of concentration.	38
Figure 53. Temperature dependent PL Spectra of DAT/HTPB.....	39
Figure 54. Emission spectra of Dy(4-BBA) ₃ (TPPO) ₂ as the sample is heated up over time.	40
Figure 55. Calculated and measured temperature of Dy(4-BBA) ₃ (TPPO) ₂ . Also shown is the emission intensity.	40
Figure 56. Microscope images of Dy(acac) ₃ in HTPB under different conditions: Daylight illumination (top left), 355 nm irradiation (top right), 355 nm irradiation and 460 nm filter	

(bottom left), and 355 nm irradiation and 485 nm filter (bottom right). The structure in the upper right part of the sample is an air bubble. 41

Figure 57. Laser heating and TCT imaging setup schematic. 42

Figure 58. Schematic of TCTI trigger timing. 43

Figure 59. Raw images for 460 nm filter (a) and 480 nm filter (b). 44

Figure 60. Room temperature image for 460 nm (a) and spatially transformed 480 nm filter image (b). 44

Figure 61. Images of laser heated sample for the 460 nm filter (a) and 480 nm filter (b). 45

Figure 62. 460 nm/480 nm image ratio for sample at room temperature (a) and for 1.795 ms laser heating (b). 46

Figure 63. Difference between heated ratio and room temperature ratio for laser heating with a duration of 1.795 ms. 46

Figure 64. Difference between heated and room temperature ratios for laser heating with a duration of 1 ms. 47

Figure 65. Fluorescence image (through 460 nm filter) for Dy:Y(acac)₃ (DPEPO) in HTPB with a loading concentration of 5 wt%. 47

Figure 66. Difference between heated and room temperature ratios, with particle outlines and beam outline. 48

Figure 67. Image (a) and schematic (b) of TCTI setup using the Splitcam system and PI-Max 4 ICCD. 50

Figure 68. Pictures showing the crystals/polyurethane composites on 1"x1" glass that are used for imaging: (a) Dy:YAG/polyurethane and (b) DYAD/polyurethane. 50

Figure 69. TCTI pulsed laser heating time scheme. 51

Figure 70. PL intensity in band 1 and band 2 during laser heating. As the temperature rises the intensity transfers from band 1 to band 2. 52

Figure 71. Change in intensity ratio images for different laser heating pulse lengths. 52

Figure 72. Temperature map at different times during pulsed laser heating. Note that the profile is elliptical, which corresponds to the underlying CO₂ laser beam profile. 54

Figure 73. Temperature map at different times during pulsed laser heating of Dy:Y(acac)₃(DPEPO) dispersed in HTPB. 55

Figure 74. Average temperature in 10 px circle centered at (x = 110, y = 160) for heating of both Dy:YAG and Dy:Y(acac)₃(DPEPO). 56

Figure 75. Schematic view of the experimental configuration (not to scale). 57

Figure 76. Smoothed streaks from shot 1 (a) and shot 2 (b). 58

Figure 77. Average intensity of the 480 nm emission peak as a function of time during the first (a) and second (b) shock experiments. For both shots, the emission is fully quenched by 150 ns after the shock enters the CCl₄. 59

Figure 78. Calculated pressure profiles for the front and the rear of a pure CCl₄ sample. 59

Figure 79. Time averaged (50 ns averaging) and normalized PL spectra for 355 nm excitation at different times during the first (a) and second (b) shock experiments. 60

Figure 80. Temporally averaged intensity (over 800 ns to 1000 ns) as a function of wavelength, with blackbody prediction at 800 K and BB fit with T found to be 3400 K. 60

Figure 81. Example multippeak fitting for shot 1 t = 0 data. 61

Figure 82. (a) SEM image of un-annealed Dy:Y ₂ O ₃ particles. (b) Photos showing particles suspension in CCl ₄ : observed under ambient light (left) and observed under a 254 nm UV lamp (right).	62
Figure 83. (a) SEM image of functionalized, annealed Dy:Y ₂ O ₃ particles (1273 K for 30 min). (b) Photos showing overnight-stable particles suspension in CCl ₄ : observed under ambient light (left) and observed under a 254 nm UV lamp (right).	63
Figure 84. Normalized PL spectra as a function of temperature for a laser heated Dy:YAG bead.	63
Figure 85. SEM micrographs of Dy:YAG nanoparticles prepared according to rgAFOSR159-53 and rgAFOSR162-65.	64
Figure 86. SEM micrographs of precursor Dy:YAG particles with different diameters: (a) in a few hundred nm range (rgAFOSR176-11) and (b) about 50 nm or less (rgAFOSR177-15).	64
Figure 87. SEM micrograph of the calcined Dy:YAG nanoparticles (1373 K for 30 min).	65
Figure 88. Dy:YAG target: (left) green body pressed using a 1273 K/1h calcined powder and (right) sintered at 1873 K for 6h. Scale bar is 1 cm.	65
Figure 89. (a) SEM and (b) EDS of Ce,Dy:Zn ₂ P ₂ O ₇ .	66
Figure 90. (a) Emission spectrum of our Dy,Ce:Zn ₂ P ₂ O ₇ and (b) excitation and emission spectra from Reference [35].	66
Figure 91. Ce,Dy:Zn ₂ P ₂ O ₇ target: (left) observed under ambient light. (right) observed under a 254 nm. The diameter is 2.64 mm. (b) A large batch of Ce,Dy:Zn ₂ P ₂ O ₇ powder.	67
Figure 92. (a, b) SEM micrographs of Dy:NaGdF ₄ . Blue arrows in (a) indicate <20 nm diameter particles. (c) EDS spectrum. (d) Picture showing fluorescence under a 254 nm UV lamp. Left is in the solid state on a glass slide and right is in a 3% v/v CHCl ₃ .	68
Figure 93. PL spectrum of Dy:NaGdF ₄ .	69
Figure 94. (a) Excitation and (b) Emission spectra of NaGdF ₄ . Reproduced from Reference [36].	69
Figure 95. PL intensity for (a) different inorganic hosts (10 ms gate) and (b) smoothed single shot spectra comparing DAT and Dy:YAG.	70
Figure 96. Pictures showing the samples used for the shock experiment: (a) Dy:YAG/polyurethane and (b) DYAD/polyurethane.	71
Figure 97. Diagram of shock experiment setup.	72
Figure 98. Spectral streak for shocked Dy:YAG dispersed in HTPB.	73
Figure 99. (a) PL spectra from Dy:YAG at different times during shock compression averaged over 50 ns. (b) Integrated intensity ratio and total intensity as a function of time during shock compression.	74
Figure 100. Spectral streak for shocked DYAD dispersed in HTPB.	75
Figure 101. (a) PL spectra from DYAD at different times during shock compression averaged over 50 ns. (b) Integrated intensity ratio and total intensity as a function of time during shock compression.	75
Figure 102	77
Figure 103. Top view view of DYAD/Polyurethane between a front buffer window (Cu) and a sapphire rear window.	77
Figure 104. Diagram of shock experiment setup.	78

Figure 105. Streak camera traces for DYAD shots with peak pressures of 3 GPa (a), 6 GPa (b), and 9 GPa (c).	79
Figure 106. Integrated intensity and ratio as a function of time during shock experiments for peak pressures of 3 GPa (a), 6 GPa (b), and 9 GPa (c). Edge wave arrival times are 1.68 μ s, 1.45 μ s, and 1.21 μ s for 3 GPa, 6GPa, and 9 GPa, respectively.	80
Figure 107. Normalized intensity (a) and ratio (b) as a function of time for different peak pressures. Edge wave arrival times are 1.68 μ s, 1.45 μ s, and 1.21 μ s for 3 GPa, 6GPa, and 9 GPa, respectively.	81
Figure 108. Streak camera trace for 6 GPa DAT shot.	82
Figure 109. (a) Spectra of DAT measured at different times after the shockwave enters the sample a (averaged over 150 ns) and (b) the integrated intensity and intensity ratio as a function of time during the shock experiment with each data point averaged over 64 ns.	82
Figure 110. Schematic view of the experimental configuration (not to scale). The impact velocity and the cell thickness were same as the Pangilinan and Gupta's 12 GPa experiment [24].	86
Figure 111. Time resolved CCl ₄ Raman spectra (50 ns spacing).	87

II. BACKGROUND

Explosives and propellants are heterogeneous materials consisting of energetic molecular crystals (e.g. RDX, HMX, etc.) embedded in polymeric binders (e.g. elastomers, fluoro-polymers, etc.). Additional components may include plasticizers, antioxidants, taggants/ markers, friction-generating grit, etc. These energetic materials can be initiated through a variety of stimuli, including thermal, mechanical, and electrical means, with the non-thermal stimuli believed to generate heat first which then causes thermally induced chemical decomposition. Optimizing the performance of energetic materials for specific applications has to be balanced against safety and reliability considerations. This process requires an improved fundamental understanding of chemical decomposition or initiation (for a particular stimulus).

Our research effort is designed to gain insight into the shock wave initiation of energetic materials (explosives and propellants). Plane shock wave studies on energetic materials have the benefit that the macroscopic loading state is well defined (uniaxial strain). Of course, the short time scales associated with shock wave loading and the destructive nature of these experiments pose significant experimental challenges.

Plane shock wave studies on energetic materials have been underway for several decades. However, due to the heterogeneous nature of these materials, a long-standing scientific issue involves relating the macroscopic state (average stress and strain) to the local stress, deformation, and temperature.

Figure 1 shows an SEM image of a typical plastic bonded explosive (PBX). Randomly oriented energetic crystals with sizes ranging from sub-micrometer to hundreds of micrometers are embedded in a polymeric binder. As a shock wave travels through such a heterogeneous material, a variety of phenomena such as pore collapse, plastic deformation, micro-fractures, shear banding, binder/crystal and crystal/ crystal interface friction, etc. can take place. Each of these mechanisms can lead to localized heating with the temperature rise dependent upon the local rate of inelastic deformation vs. the local heat dissipation. If sufficient heating occurs, these local hot-spots can lead to chemical energy release in the material.

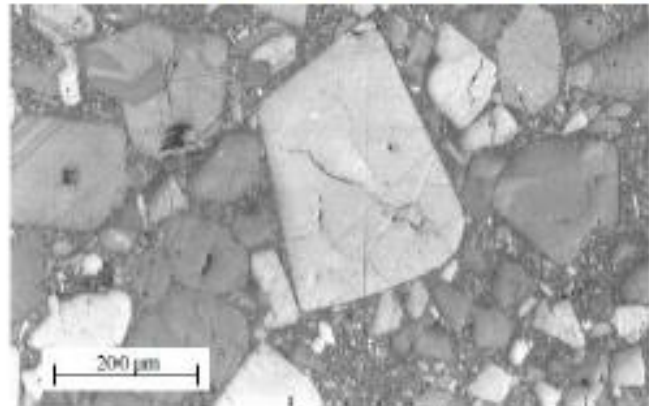


Figure 1. SEM image of PBX (reproduced from Ref. [1]).

Hot-spot formation and the resulting chemical decomposition during shock and impact have been investigated by many researchers. [2–11] While many different mechanisms have been identified and characterized, it is not known which of them is responsible for chemical energy release for a given material composition under specific loading

conditions. The complexity of this problem, was expressed by Field et al. as: “*The results show that no one mechanism is the dominant means of ignition and that only very slight changes in the conditions of an experiment can lead to ‘hot spots’ being formed by different processes.*” [12]

Advances in mesoscale modeling and simulations (starting with Mel Baer’s pioneering work at Sandia), and in computing capabilities can now provide estimates of the local variables of interest. However, without real-time measurements of local variables in shocked heterogeneous solids, it is difficult to ascertain the validity of the numerical simulations.

Progress has been made over the years in developing more advanced experimental capabilities to characterize hot-spot formation. For example, Dlott et al. reported on temperature imaging with a temporal resolution of 8.3 ms using mid-IR cameras for hot spots generated by ultrasonic or long-wavelength infrared exposure (pulses of about 450 ms), and on the use of dye-based pressure sensors in shock experiments generated by laser-driven flyer plates with shock durations of about 15 ns. [13–16] Progress toward in-situ microstructural evolution measurements under shock wave loading was recently reported by Jensen et al. [17–19] These authors were able to monitor microstructural changes in heterogeneous materials under impact loading using phase contrast imaging (PCI) and Laue XRD.

With the recent development of the NNSA supported Dynamic Compression Sector (DCS) at the Advanced Photon Source (Argonne National Laboratory), there exists a significant opportunity to obtain real time measurements of microstructural changes in shocked energetic materials.

The ability to measure in-situ microstructural evolution on ns- μ s timescales in shock experiments is an exciting prospect. However, such measurements are not enough. To fully utilize the microstructure measurements, experimental methods are needed to provide complementary measurements of local temperatures. These two types of measurements on identical samples and under identical loading conditions will represent a major advance in real-time, mesoscale measurements.

III. OBJECTIVES

Our objectives are to investigate potential temperature sensors for use in heterogeneous materials, to determine the feasibility of temperature measurements under dynamic compression and, if successful, to examine the microstructural evolution under dynamic compression of heterogeneous samples containing our temperature sensors.

IV. APPROACH

Two types of sensors are needed, one to measure the temperature within the binder, and one to measure the temperature within particulates embedded in the binder. The main challenge is to ensure that the signal-to-noise level of the 2CFT measurements using

these temperature sensors is sufficiently high under single laser pulse excitation and shock wave loading conditions. As such, the luminescence intensity of the temperature probes needs to be maximized and the noise level for the optical excitation and detection processes must be minimized.

Our temperature sensors consist of molecular complexes that contain lanthanide ions such as Dy³⁺ and Sm³⁺. Both ions have been successfully used for 2CFT. Using organic ligands to form lanthanide complexes serves several purposes:

1. The molar absorption of lanthanide ions is relatively small ($0.1 - 10 \text{ M}^{-1}\text{cm}^{-1}$). The ligands increase the molar absorption to $10^4 - 10^5 \text{ M}^{-1}\text{cm}^{-1}$ and the energy is then very quickly transferred to the lanthanide ion.
2. Selecting the appropriate ligand allows us to disperse the complex within the polymer binder and then probe the temperature at various locations.
3. Selecting the appropriate ligand allows us to grow molecular crystals with mechanical properties similar to those of HE crystals, and then probing the temperature within the crystals.

During actual temperature measurements, the heterogeneous samples containing our molecular and molecular crystal sensors will be excited by a UV laser pulse shortly before shock impact. This timing allows us to excite the lanthanide complex and transfer all the energy to the lanthanide ion before the shock disturbs the ligand configuration and affects the absorption properties. Depending on the ligand, the fluorescence lifetime of the lanthanide ranges between about 5 μs and 20 μs , giving us tens of microseconds to monitor the fluorescence properties and thus the temperature of the sample.

The fluorescence will be imaged by two cameras with different wavelength filters. Subsequent processing of the images will provide a temperature image of the sample during shock loading which can be compared with images of the microstructure to correlate specific microstructural changes with temperature.

V. ACCOMPLISHMENTS

A. Overview

During this project we developed non-contact optical temperature sensors suitable for use in polymeric binders and in molecular crystal components of heterogeneous materials, as well as on characterizing the optical properties of these temperature sensors.

We have synthesized and characterized eight different sensor materials, four of them for potential use as molecular crystals (MC), and four of them as potential dyes for dispersion in the polymer, see Table 1.

Table 1. Potential sensor materials

Sensor Type	Material
MC	Dy(acac) ₃ (phen)
MC	Dy(4-BBA) ₃ (TPPO) ₂
MC	Dy(PBI) ₃ (DPEPO)
MC	Dy(acac) ₃ (DPEPO)
Dye	Sm(2-ethyl hexanoate) ₃
Dye	Sm(acac) ₃ (TOPO) ₂
Dye	Sm(acac) ₃
Dye	Dy(acac) ₃
Dye	Dy(acac) ₃ (TOPO)

acac = acetylacetonate
phen = 1,10-phenanthroline
BBA = 4-benzoylbenzoic acid
TPPO = triphenylphosphine oxide
PBI = 3-phenyl-4-benzoyl-5-isoxazolone
DPEPO = bis(2-(diphenylphosphino)phenyl) ether oxide
TOPO = trioctylphosphine oxide

With regards to shock compression measurements, we performed several shots of both dye-doped and undoped CCl₄ using a 2.5" bore single-stage gas gun. CCl₄ was chosen as the host material as it has a known equation-of-state allowing for independent temperature verification. Based on the dye-doped shock tests we determine that our soluble dye (Dy(acac)₃(TOPO)) undergoes complete PL quenching during shock, with the most likely mechanism being deformation of the ligands. We are now evaluating several alternative phosphor materials, including inorganic hosts which should be less sensitive to effects due to conformational changes.

B. Binders

We have evaluated three different binders HTPB/IPDI/DOA, Clear Flex 50, and EPON 813 / EPIKURE 3223 as matrix materials for the thermosensors. HTPB/IPDI/DOA is a polyurethane (PU) and is commonly used in plastic-bonded explosives (PBX). Clear Flex 50 is also a PU, but is not as soft as HTPB/IPDI/DOA. EPON 813 / EPIKURE 3223 on the other hand is an epoxy.

All three binders can be easily processed into transparent samples, see Figure 1. The figure also shows images of Clear Flex 50 samples with different thicknesses that contain small amounts of molecular crystal temperature sensors, and a magnified image of molecular crystal temperature sensors embedded in the binder material.

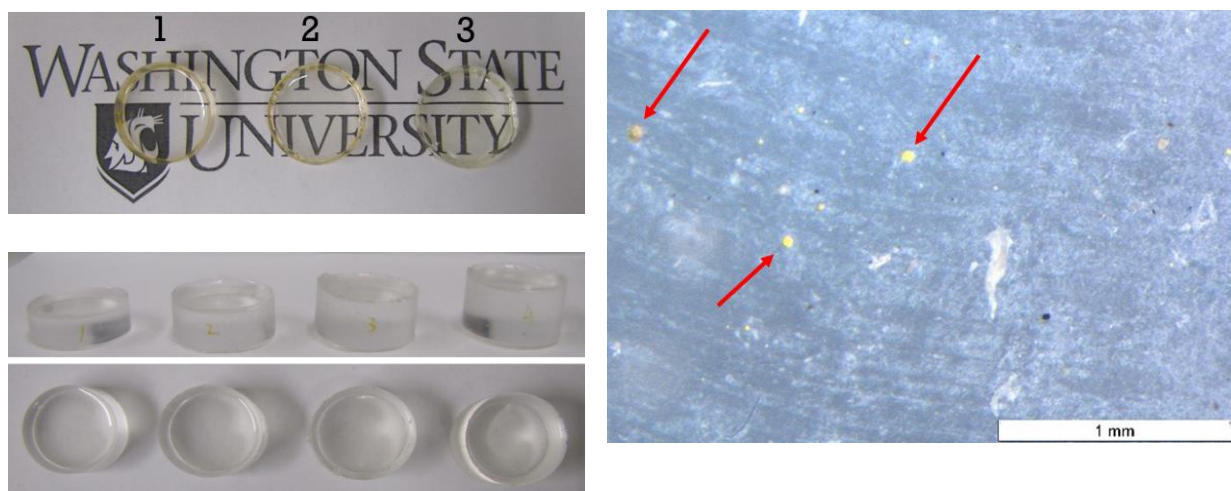


Figure 1. Transparent samples of all three binders (top left), Clear Flex 50 samples containing temperature sensors (bottom left), and magnified image of molecular crystal sensors embedded in binder (right).

Figure 2. shows the optical absorption spectra of the three binders. As can be seen, Clear Flex 50 starts absorbing at around 400 nm, while the other two materials are transparent to about 300 nm. Since the thermosensors require an excitation by 355 nm, Clear Flex 50 has been ruled out for further use. Figure 3. shows samples of HTPB/IPDI/DOA and EPON 813 / EPIKURE 3223 containing some Sm-based thermosensors. While the HTPB/IPDI/DOA samples show red emission, the epoxy samples don't. Most likely, the epoxy contains some chemical groups that quench the luminescence from the thermosensors. As a result, all future experiments will be conducted on HTPB/IPDI/DOA binder samples.

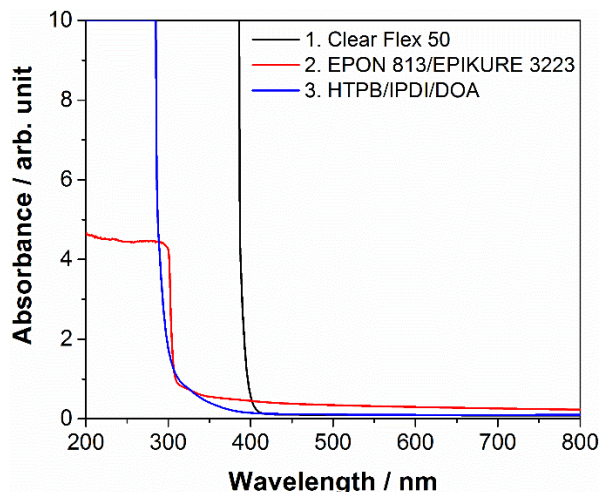


Figure 2. Optical absorption of potential binder materials.

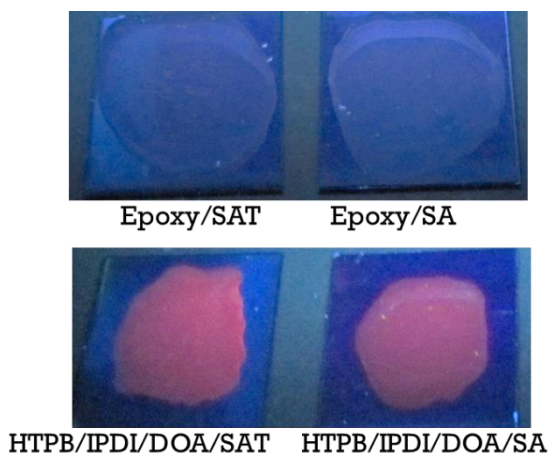


Figure 3. UV (254 nm) illuminated epoxy and HTPB/IPDI/DOA binder samples containing thermosensors.

C. Molecular Crystal Sensors

Dy(acac)₃(phen)

The molecular structure of $Dy(acac)_3(phen)$ is shown in Figure 4.. The complex consists of a Dy^{3+} ion surround by three acac and one phen ligand.

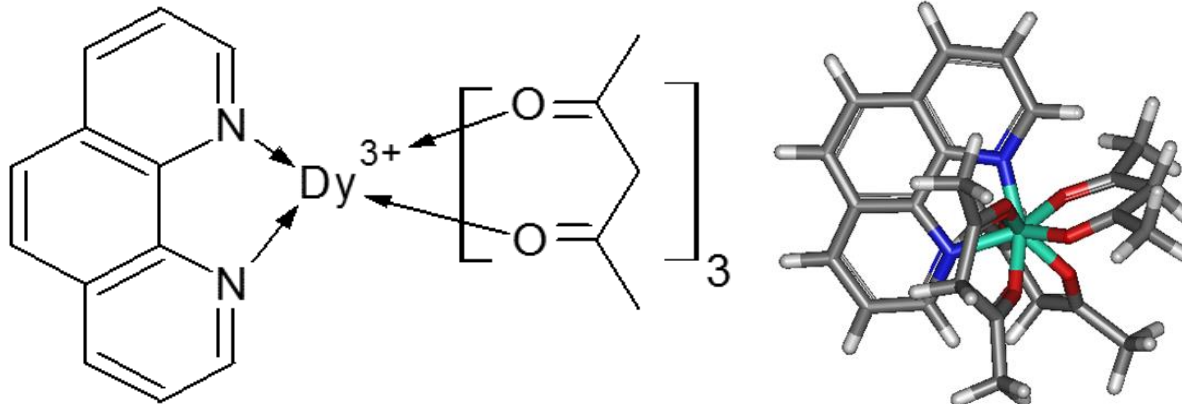


Figure 4. Molecular structure of $Dy(acac)_3(phen)$.

This material was grown into molecular crystals. Figure 5. shows an optical microscope image and an x-ray diffraction pattern of the crystals. The crystals show a wide range of sizes and shapes.

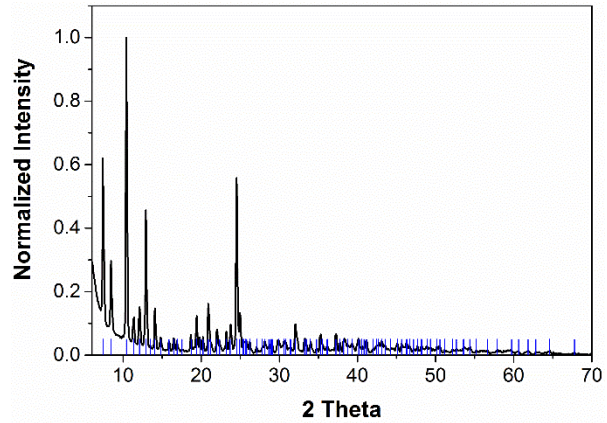
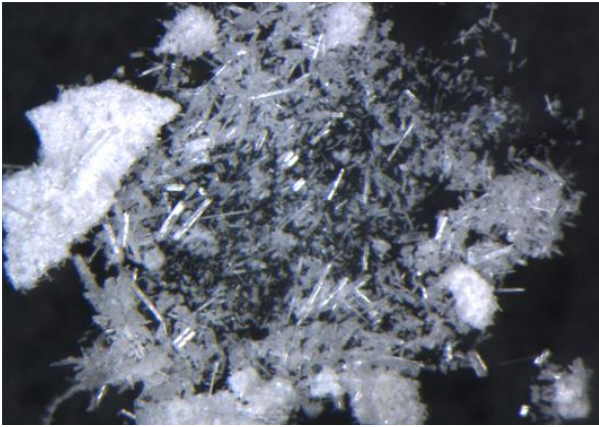


Figure 5. Optical image (left) and x-ray diffraction pattern of $\text{Dy}(\text{acac})_3(\text{phen})$.

The FTIR spectrum shown in Figure 6. shows that both types of ligands are present. Figure 7. shows the bright yellow-green emission of $\text{Dy}(\text{acac})_3(\text{phen})$ when excited with 254 nm light.

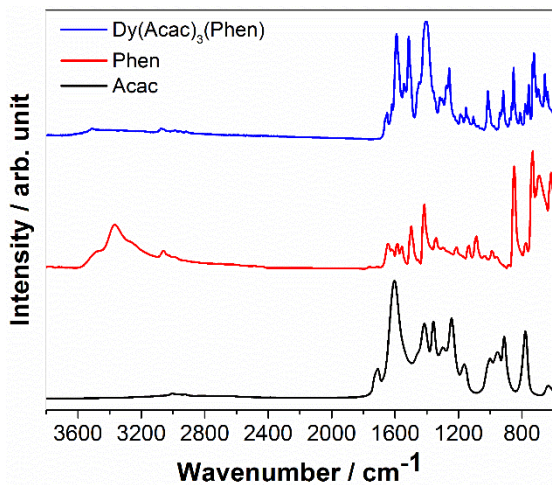


Figure 6. FTIR spectra of acac, phen, and $\text{Dy}(\text{acac})_3(\text{phen})$.



Figure 7. Optical image of $\text{Dy}(\text{acac})_3(\text{phen})$ illuminated by 254 nm light.

Figure 8. shows the absorbance of HTPB, $\text{Dy}(\text{acac})_3(\text{phen})$ in HTPB, and $\text{Dy}(\text{acac})_3(\text{phen})$. As can be seen, 355 nm, the third harmonic of a Nd:YAG laser, is a good match for the excitation of this material.

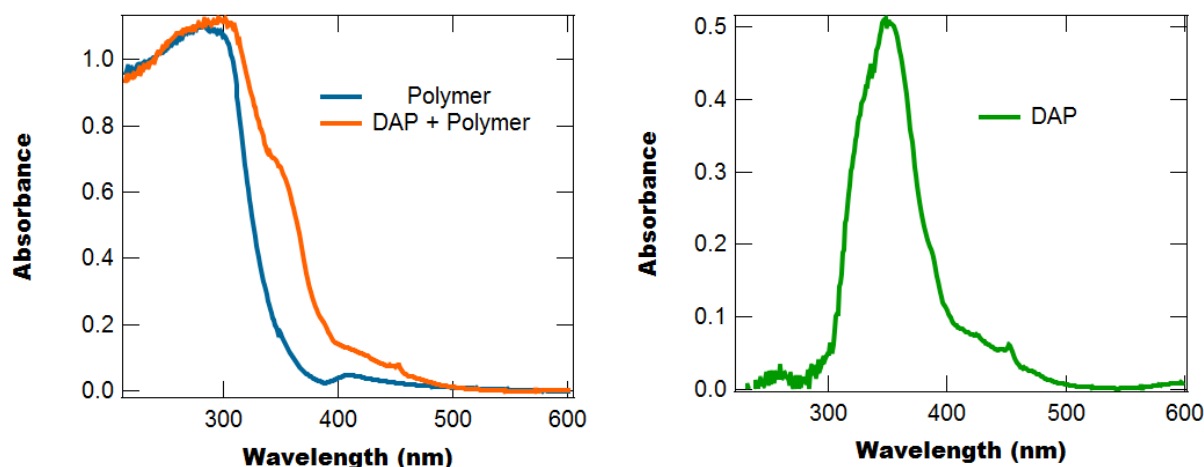


Figure 8. Absorbance of HTPB and $\text{Dy}(\text{acac})_3(\text{phen})$ in HTPB (left), and $\text{Dy}(\text{acac})_3(\text{phen})$ (right).

Figure 9 shows temperature-dependent emission spectra of $\text{Dy}(\text{acac})_3(\text{phen})$ and of $\text{Dy}(\text{acac})_3(\text{phen})$ in HTPB. The $\text{Dy}(\text{acac})_3(\text{phen})$ powder spectra show the emission lines of Dy^{3+} sitting on a large background which is due to ligand emission. The spectra of $\text{Dy}(\text{acac})_3(\text{phen})$ in HTPB show an even larger background due to polymer emission. Also shown is the normalized emission spectrum of $\text{Y}(\text{acac})_3(\text{phen})$ for 355 nm excitation. Y is optically inactive and all the emission is originating from the ligands.

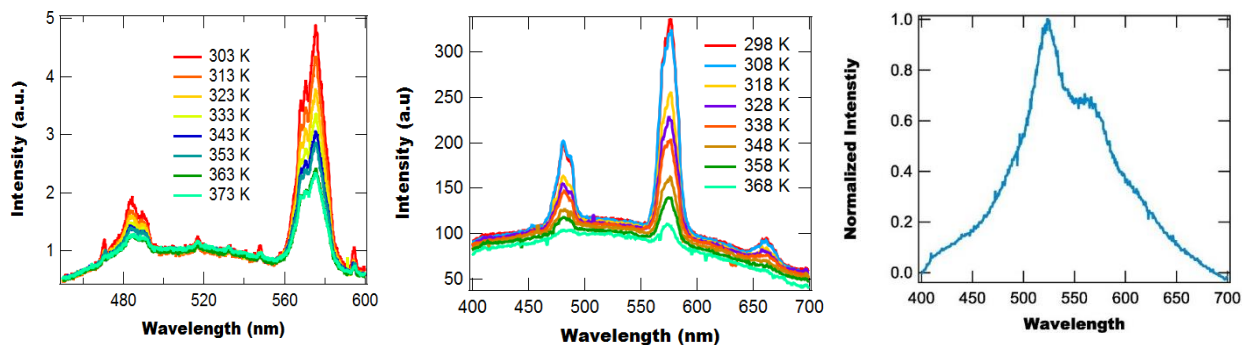


Figure 9. Temperature-dependent emission spectra of $\text{Dy}(\text{acac})_3(\text{phen})$ (left) and of $\text{Dy}(\text{acac})_3(\text{phen})$ in HTPB (center). Normalized emission spectrum of $\text{Y}(\text{acac})_3(\text{phen})$ showing the ligand background emission for 355 nm excitation.

Also, the investigation of this material, showed that concentration quenching is an issue. Figure 10. shows the lifetime of pure (100%) $\text{Dy}(\text{acac})_3(\text{phen})$ in HTPB at 481 nm as a function of temperature. The decay has a short and a long component with room-temperature values of about 55 ns and 340 ns. Furthermore, the material shows photodegradation as it is exposed to UV light, see Figure 11..

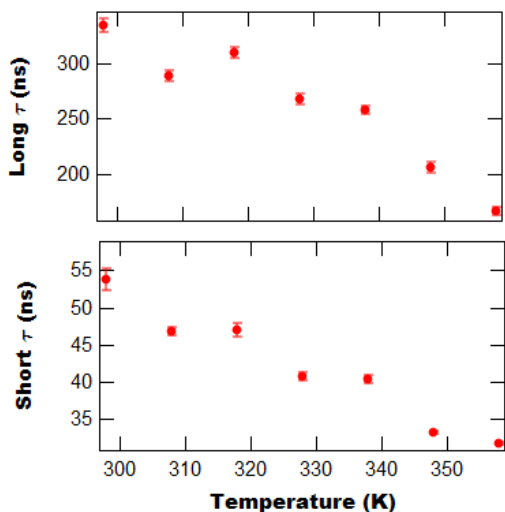


Figure 10. Temperature-dependent fluorescence lifetimes of pure Dy(acac)₃(phen) in HTPB at 481 nm.

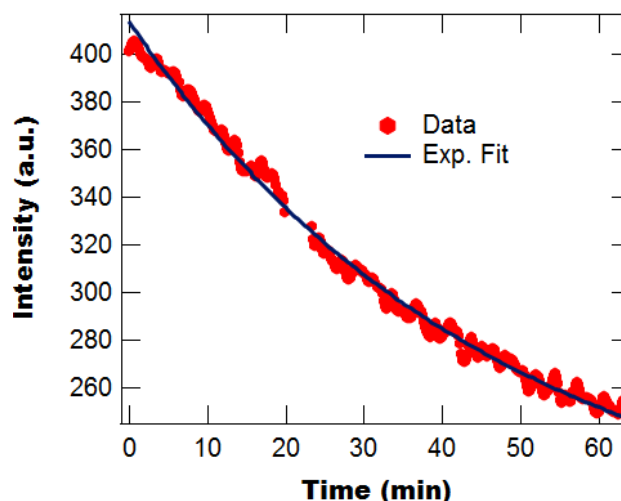


Figure 11. Emission intensity of Dy_{0.1}Y_{0.9}(acac)₃(phen) at 575 nm as a function of UV exposure time at room-temperature.

In order to address some of these short-comings, we adjusted the Dy concentration by diluting it with optically inactive Y, and also switched to a gated detection technique. Figure 12. shows emission spectra of Dy(acac)₃(phen) for different concentrations, as well as for gated detection. The sample with a 10% Dy and 90% Y concentration shows the highest emission intensity with a fluorescence lifetime of about 6 μs. In addition, switching to a gated detection technique improves the S/N by almost a factor of 10.

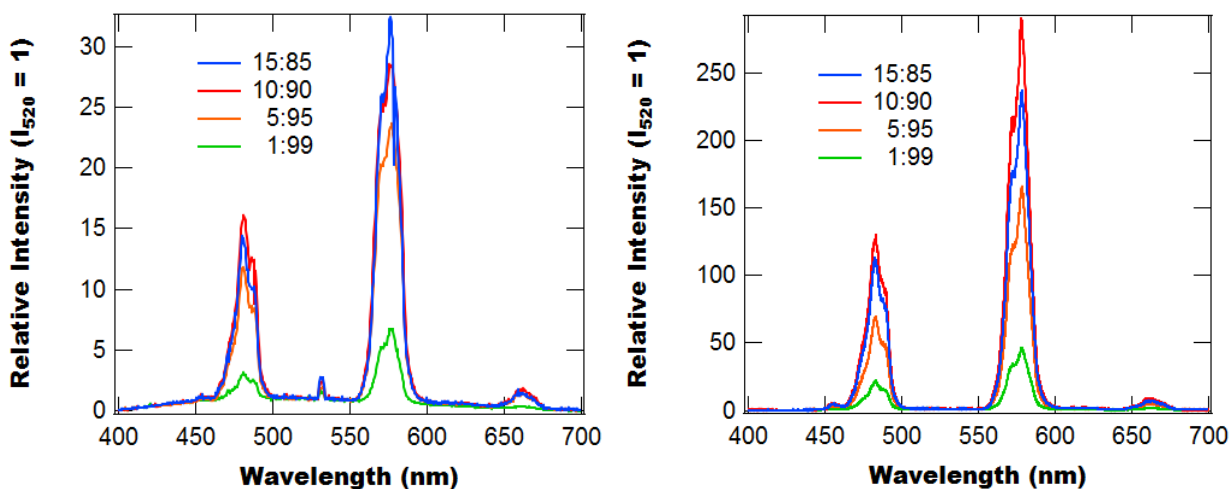


Figure 12. Emission spectra of Dy/Y(acac)₃(phen) for different concentrations, without (left) and with (right) gated detection.

Figure 13 shows the time-resolved emission of Dy/Y(acac)₃(phen) at 482 nm and 575 nm for different concentrations. Also shown are the relative intensities and lifetimes at 482 nm as a function of Dy concentration. The fluorescence lifetime drops by about a factor

of 2 between 1% and 15%, decreasing from about 16 μs to about 7 μs , while the absolute intensity peaks at about 10%.

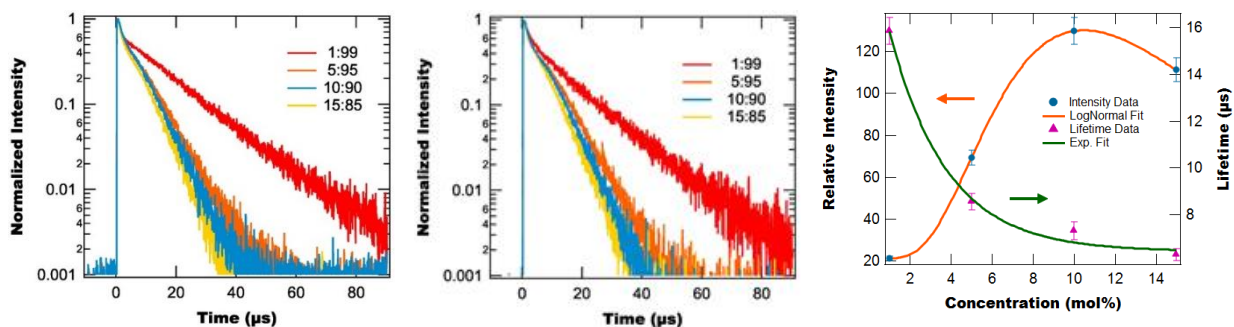


Figure 13. Time-resolved emission of Dy/Y(acac)₃(phen) at 482 nm (left) and 575 nm (center) for different concentrations. Also shown are the relative intensities and lifetimes at 482 nm as a function of Dy concentration (right).

Figure 14 provides more information about the Dy concentration on the optical properties. The normalized emission intensity as a function of temperature is relatively independent of concentration, however, as mentioned earlier, the 10% Dy/90% Y sample has the strongest emission intensity in absolute terms. The integrated ratio of the emission intensity for the two colors are also relatively similar, except for the lowest (1% Dy) sample. Also shown is the temperature-dependent fluorescence lifetime of 10:90 Dy/Y(acac)₃(phen) at 482 nm and 575 nm.

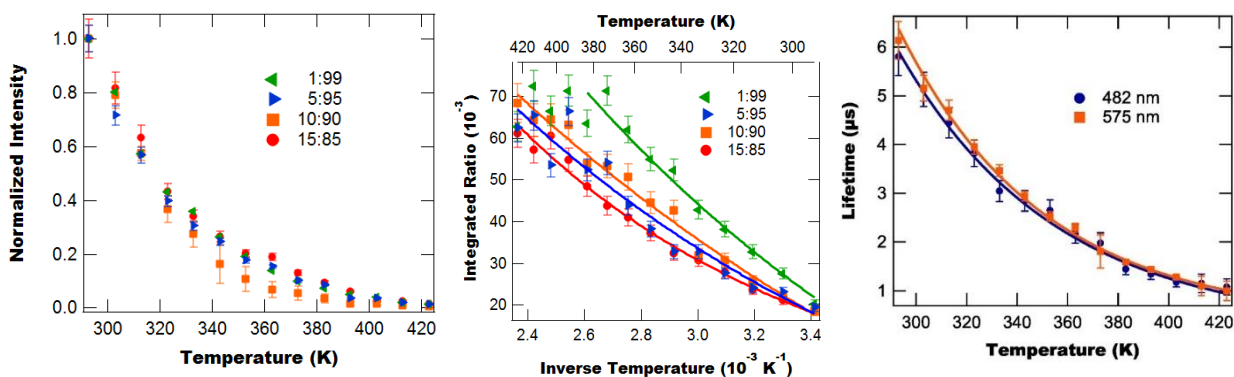


Figure 14. Temperature dependent emission intensity (left) at 484 nm, normalized to $T = 293 \text{ K}$ value, and ratio of integrated peak intensities (center) for peaks centered at 453 nm (450 nm - 460 nm) and 481 nm (462 nm – 504 nm). Fluorescence lifetimes of 10:90 Dy/Y(acac)₃(phen) at 482 nm and 575 nm.

Table 2 shows the exponential fit parameters for the temperature-dependent emission intensities ratios shown in Figure 14.

Table 2. Exponential fit parameters from data in Figure 3 for different Dy/Y ratios.

Dy/Y Ratio	A	$\square E (10^{-3} \text{ eV})$
1:99	2.30 ± 0.87	114 ± 14
5:95	1.06 ± 0.31	100.1 ± 9.4
10:90	1.08 ± 0.20	98.4 ± 6.2
15:85	0.98 ± 0.13	99.7 ± 4.3

The values for the energy gap correspond to about 800 cm^{-1} to 900 cm^{-1} and are close to the expected value.

Dy(acac)₃(DPEPO)

The molecular structure of $\text{Dy}(\text{acac})_3(\text{DPEPO})$ is shown in Figure 15.. The complex consists of a Dy^{3+} ion surround by three acac and one DPEPO ligand.

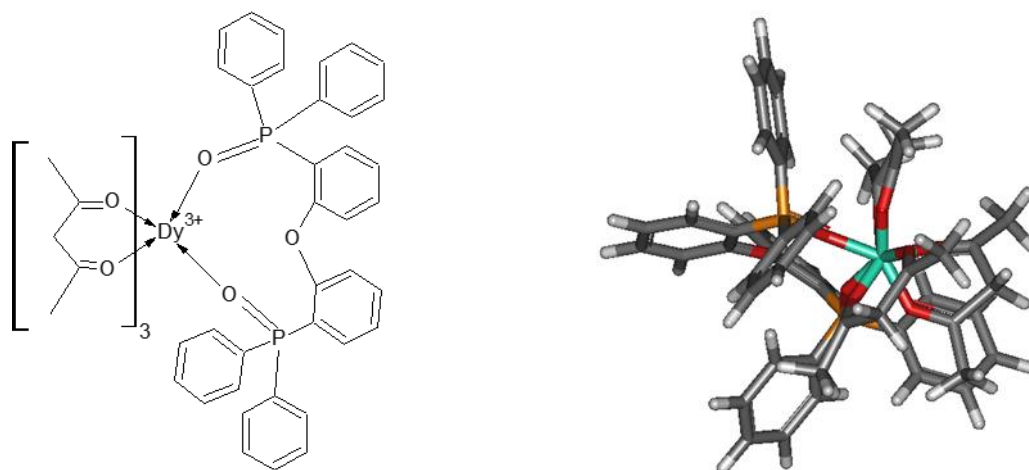


Figure 15. Molecular structure of $\text{Dy}(\text{acac})_3(\text{DPEPO})$.

This material was also grown into molecular crystals. Figure 16. shows an optical microscope image and an image of the material for excitation with 254 nm light. The material emits bright yellow-green light.

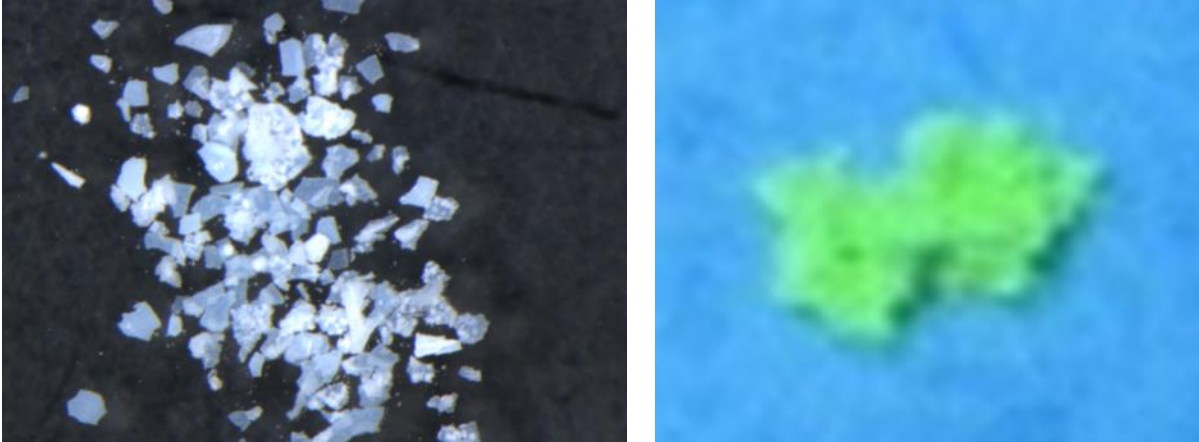


Figure 16. Microscope image (left) and optical image for illumination with 254 nm (right) of $\text{Dy}(\text{acac})_3(\text{DPEPO})$.

Figure 17. shows the emission spectra of $\text{Dy}(\text{acac})_3(\text{DPEPO})$ at temperatures as high as 433 K. The peaks at about 484 nm (${}^4\text{F}_{9/2} \rightarrow {}^6\text{H}_{15/2}$) and 455 nm (${}^4\text{I}_{15/2} \rightarrow {}^6\text{H}_{15/2}$) are used for determining temperature, while the peak at 575 nm corresponds to the ${}^4\text{F}_{9/2} \rightarrow {}^6\text{H}_{13/2}$ transition. Also shown are the temperature-dependent emission intensity at 484 nm and 575 nm and the integrated ratio (450 nm – 460 nm)/(462 nm – 504 nm) of $\text{Dy}(\text{acac})_3(\text{DPEPO})$. The upper temperature is limited by decomposition of the organic ligands and thermal quenching. However, this limit is not to be confused with the limits expected during single-pulse temperature measurements.

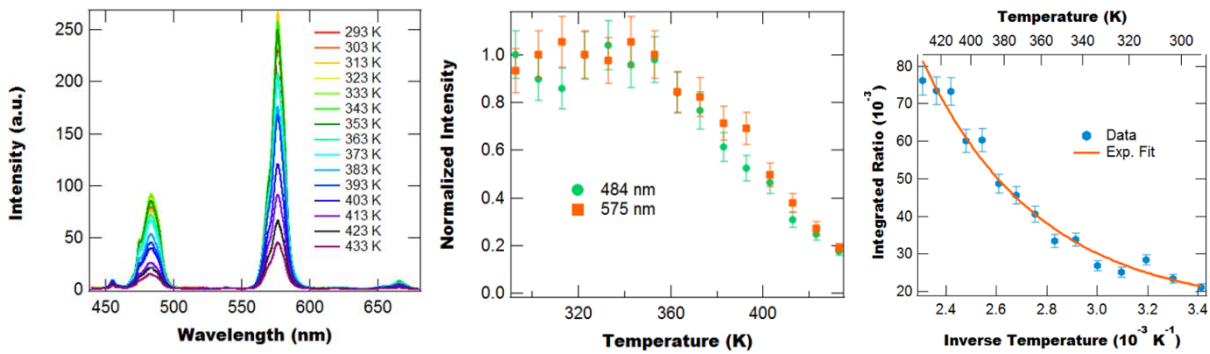
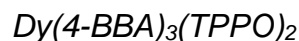


Figure 17. Temperature-dependent emission spectra (left), emission intensities (center), and integrated ratio (right) of $\text{Dy}(\text{acac})_3(\text{DPEPO})$.

The room temperature lifetimes and energy splitting of $\text{Dy}(\text{acac})_3(\text{DPEPO})$ are: $T_{455} = (17.13 \pm 0.32) \mu\text{s}$, $T_{482} = (21.34 \pm 0.22) \mu\text{s}$, $T_{575} = (22.25 \pm 0.26) \mu\text{s}$, and $\Delta E = (0.1071 \pm 0.0033) \text{ eV}$.



The molecular structure of $\text{Dy}(4\text{-BBA})_3(\text{TPPO})_2$ is shown in Figure 18.. The complex consists of a Dy^{3+} ion surround by three acac and one phen ligand.

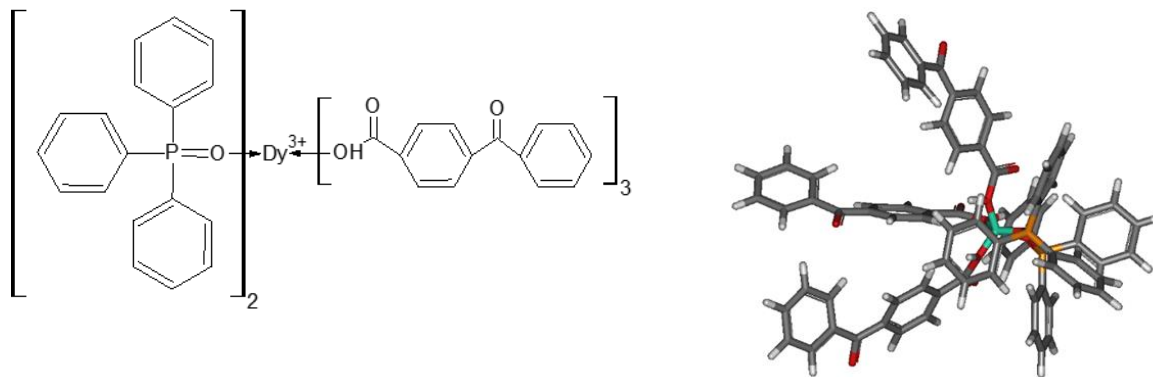


Figure 18. Molecular structure of $\text{Dy}(4\text{-BBA})_3(\text{TPPO})_2$.

This material was grown into molecular crystals. Figure 19. shows an optical microscope image and an x-ray diffraction pattern of the crystals. While the XRD pattern shows distinct diffraction peaks, there is also a broad background indicating an amorphous phase.

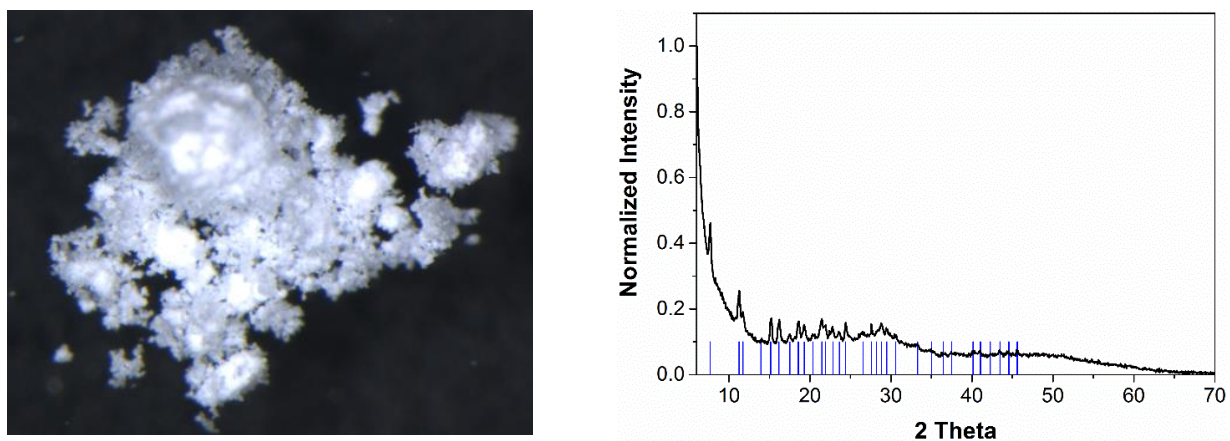


Figure 19. Optical image (left) and x-ray diffraction pattern of $\text{Dy}(\text{acac})_3(\text{phen})$.

The FTIR spectrum shown in Figure 20. shows that both types of ligands are present. Figure 21. shows the material for excitation with 254 nm light. The material emits green light.

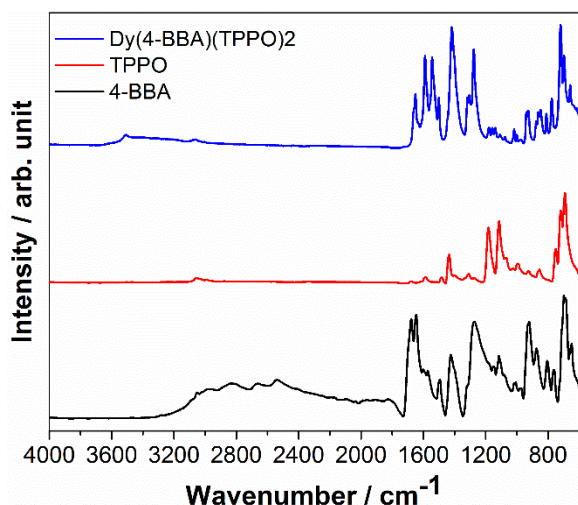


Figure 20. FTIR spectra of 4-BBA, TPPO, and Dy(4-BBA)₃(TPPO)₂.



Figure 21. Optical image of Dy(4-BBA)₃(TPPO)₂ illuminated by 254 nm light.

Figure 22. shows the emission spectra of Dy(4-BBA)₃(TPPO)₂ at temperatures as high as 423 K. The peaks at about 484 nm (⁴F_{9/2} → ⁶H_{15/2}) and 455 nm (⁴I_{15/2} → ⁶H_{15/2}) are used for determining temperature, while the peak at 575 nm corresponds to the ⁴F_{9/2} → ⁶H_{13/2} transition. The temperature-dependent emission intensity at 484 nm and 575 nm and the integrated ratio (450 nm – 460 nm)/(462 nm – 504 nm) of Dy(4-BBA)₃(TPPO)₂ are also shown in Figure 22.

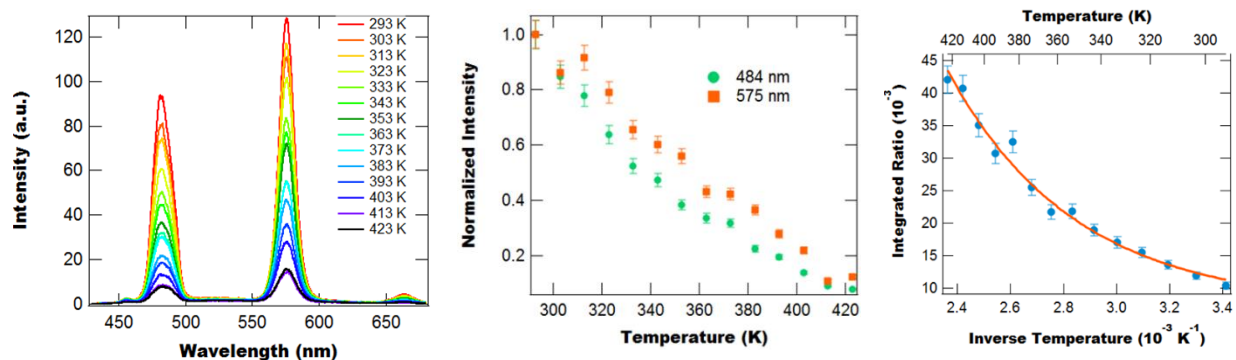


Figure 22. Temperature-dependent emission spectra (left), emission intensities (center), and integrated ratio of Dy(4-BBA)₃(TPPO)₂.

The upper temperature is limited by decomposition of the organic ligands and thermal quenching. However, this limit is not to be confused with the limit expected during single-pulse temperature measurements. The room temperature lifetimes and energy splitting of Dy(acac)₃(DPEPO) are: $\tau_{455} = (6.19 \pm 0.57) \mu\text{s}$, $\tau_{482} = (7.30 \pm 0.30) \mu\text{s}$, $\tau_{575} = (7.29 \pm 0.39) \mu\text{s}$, and $\Delta E = (0.1161 \pm 0.0039) \text{ eV}$.

$Dy(PBI)_3(DPEPO)$

This material was found to be not suitable for our purposes as it absorbs in the blue wavelength region.

$Dy:Y(hfa)_3(DPEPO)$

From a review of the literature on Ln-doped complexes we find that in many cases replacing the hydrogen atoms in a complex with fluorine atoms produces improved performance [20]. This improvement is due to H-F substitution resulting in high energy phonon modes being suppressed, which results in a decrease in the number of nonradiative energy loss channels. It is therefore desirable to perform this H-F substitution on some of our complexes to improve their performance.

The ligand that is most easily fluorinated is acac, with the fluorinated version being hfa. We therefore prepare (with 10 mol% Dy-doping) a partially fluorinated version of $Dy:Y(acac)_3(DPEPO)$, which is $Dy:Y(hfa)_3(DPEPO)$. See Figure 23 for a schematic of the molecule. Once prepared, we measure the emission properties (using 355 nm excitation) as a function of temperature. Figure 24 shows the emission spectra at different temperatures with the spectra looking similar to the other Dy-doped complexes.

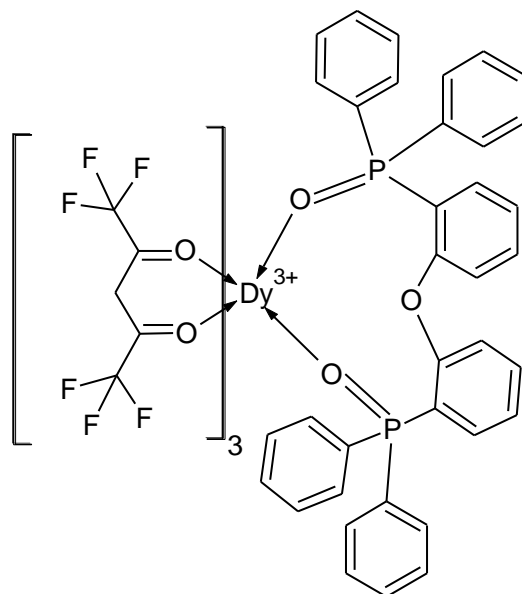


Figure 23. Schematic of $Dy:Y(hfa)_3(DPEPO)$'s chemical structure.

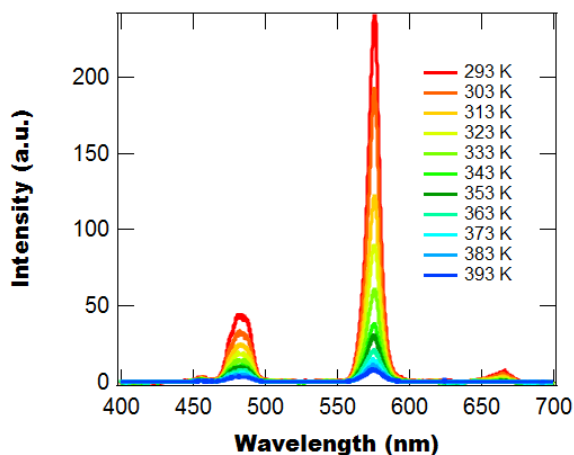


Figure 24. Emission spectra of Dy:Y(hfa)₃(DPEPO) at different temperatures.

From Figure 24 we find that the maximum peak intensity of the $^4F_{9/2} \rightarrow ^6H_{15/2}$ transition is at 482.91 nm and the maximum peak intensity of the $^4I_{15/2} \rightarrow ^6H_{15/2}$ transition is at 455.98 nm. Using these wavelengths, we also measure the lifetime of the two excited states and find that the $^4F_{9/2}$ energy level has a lifetime of $(3.39 \pm 0.65) \mu\text{s}$ and the $^4I_{15/2}$ energy level has a lifetime of $(2.76 \pm 0.71) \mu\text{s}$. These are the shortest lifetimes we have measured for our Dy-doped yttrium complexes.

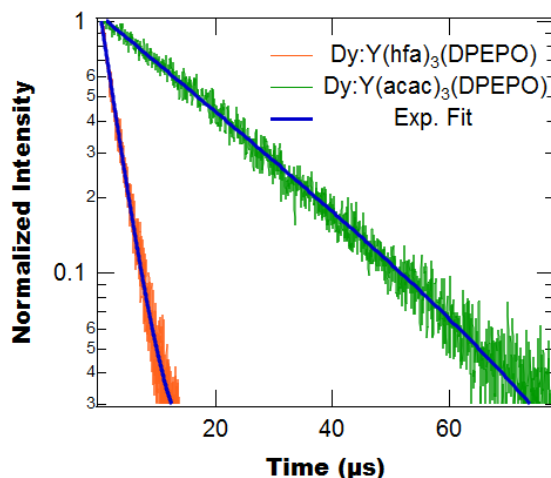


Figure 25. Normalized intensity at 482 nm as a function of time for Dy:Y(hfa)₃(DPEPO) and Dy:Y(acac)₃(DPEPO).

To compare the $^4F_{9/2}$ lifetime of both the fluorinated and non-fluorinated versions of the MC, we plot the normalized PL decay curves of both materials in Figure 25. From Figure 25 we find that the fluorinated version has a significantly shorter lifetime than the non-fluorinated version. This is unexpected given the stabilization effect seen previously in H-F substitution. However, we can understand this result by considering the energy difference between hfa's lowest triplet state and Dy's $^4F_{9/2}$, which is 0.18 eV. This energy difference is smaller than the empirically determined minimum difference for efficient

energy transfer [21]. This means that there is a larger degree of back energy transfer from ion to ligand than for the case of acac.

Additionally, from Figure 24 we find that the emission is quenched as the temperature is increased. To characterize the thermal quenching of Dy:Y(hfa)₃(DPEPO) we plot the peak intensity of the 482 nm peak as a function of temperature in Figure 26, where we have normalized the intensity such that the room temperature intensity is unity. From Figure 26 we find that the intensity follows a sigmoid function with temperature, with its half-temperature being 317 K.

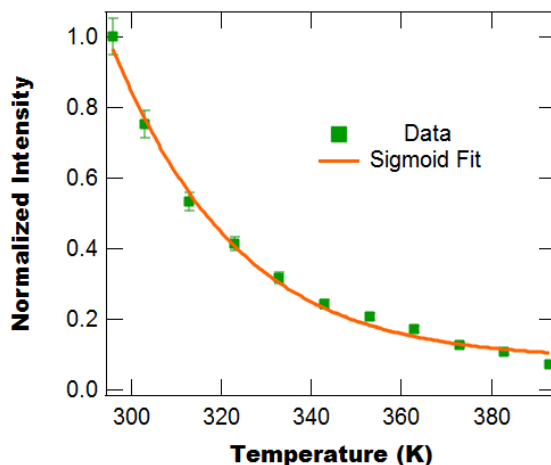


Figure 26. Intensity at 482 nm as a function of temperature for Dy:Y(hfa)₃(DPEPO) with the intensity normalized such that the room temperature intensity is unity.

We also perform ratio calibration measurements in which we compute the integrated intensity of the 455 nm (integration range 450-465) and 480 nm (integration range 465-504) peaks. Figure 27 displays the integrated ratio as a function of inverse temperature with a fit to an exponential function. The exponential fit yields an energy difference of $\Delta E = 76 (\pm 12) \times 10^{-3}$ eV and a proportionality constant of 0.65 ± 0.27 .

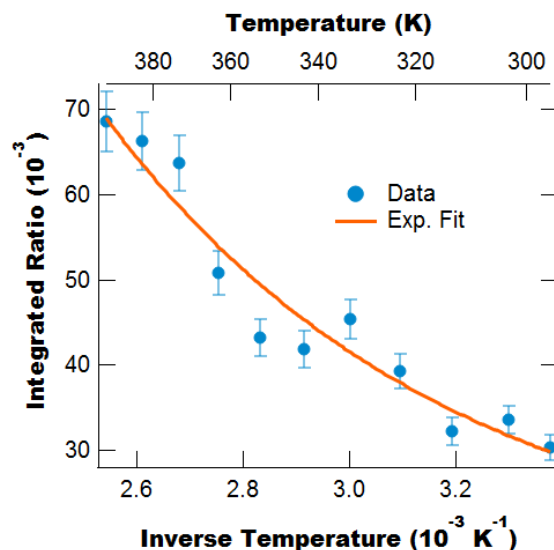


Figure 27. Integrated intensity ratio (455 nm/482 nm) as a function of inverse temperature with an exponential fit.

D. Molecular Dye Sensors

Sm(acac)₃(TOPO)₂

Sm(acac)₃(TOPO)₂ was synthesized as a potential dye for incorporation into the polymer matrix. The TOPO ligands, see Figure 28. , allow the material to be readily dissolved into the polymer matrix, while the acac ligands provide the optical functionality. Figure 29. shows a microscope image of *Sm(acac)₃(TOPO)₂*. The material has a gooey consistency.

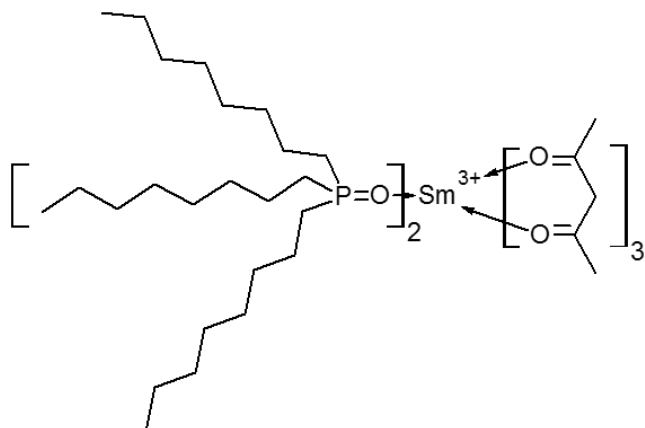


Figure 28. Molecular structure of **Figure 29.** Microscope image of *Sm(acac)₃(TOPO)₂*.

Figure 30. shows the FTIR spectra of *Sm(acac)₃(TOPO)₂*, acac, and TOPO, indicating that the sample contains both ligands. When irradiated by 254 nm light, the sample emits red light, see Figure 31. .

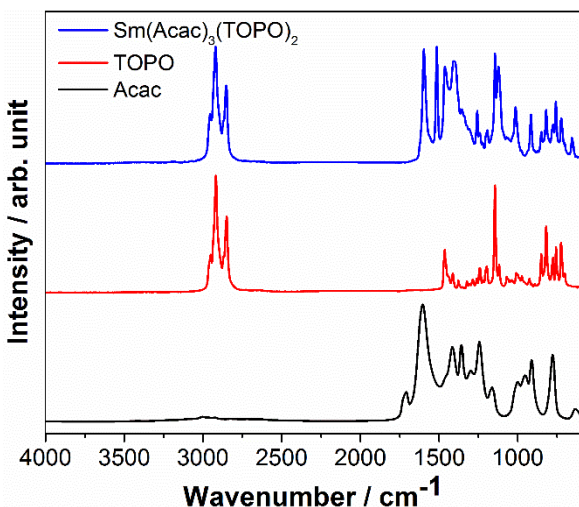


Figure 30. FTIR of $\text{Sm}(\text{acac})_3(\text{TOPO})_2$.



Figure 31. $\text{Sm}(\text{acac})_3(\text{TOPO})_2$ illuminated by 254 nm radiation.

Figure 32. shows the temperature dependent emission spectra, intensities at three wavelengths, and integrated ratio for $\text{Sm}(\text{acac})_3(\text{TOPO})_2$ for temperatures up to 433 K. The emission intensity at 566 nm stays about constant for temperatures up to about 363 K.

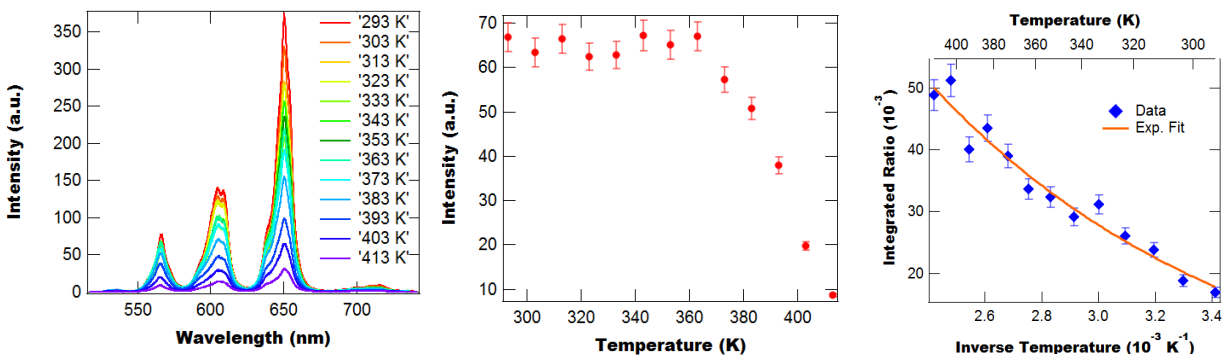


Figure 32. Temperature dependent emission spectra (left), emission intensities at 566 nm (center), and integrated 535 nm/566 nm ratio (right) of pure $\text{Sm}(\text{acac})_3(\text{TOPO})_2$.

Table 3 shows the observed peak centers and lists the transition assignments.

Table 3. Sm³⁺ transition assignments for observed SAT emission peaks with free ion wave-lengths shown for reference. Note that the 566 nm, 605nm, and 650 nm each contain two closely spaced transitions.

Peak Center / nm	Transition(s)	Free Ion Wavelength(s) / nm
535	$^4F_{3/2} \rightarrow ^6H_{5/2}$	529
566	$^4G_{5/2} \rightarrow ^6H_{5/2}$	559
	$^4F_{3/2} \rightarrow ^6H_{7/2}$	561
605	$^4G_{5/2} \rightarrow ^6H_{7/2}$	595
	$^4F_{3/2} \rightarrow ^6H_{9/2}$	602
650	$^4G_{5/2} \rightarrow ^6H_{9/2}$	640
	$^4F_{3/2} \rightarrow ^6H_{11/2}$	654
720	$^4G_{5/2} \rightarrow ^6H_{11/2}$	700

Figure 33. shows the corresponding data for Sm(acac)₃(TOPO)₂ dissolved in HTPB. The integrated ratios appear to be slightly higher when the material is dissolved in HTPB compared to when it is pure. Also, dispersion into the polymer appears to change the temperature dependence of the emission.

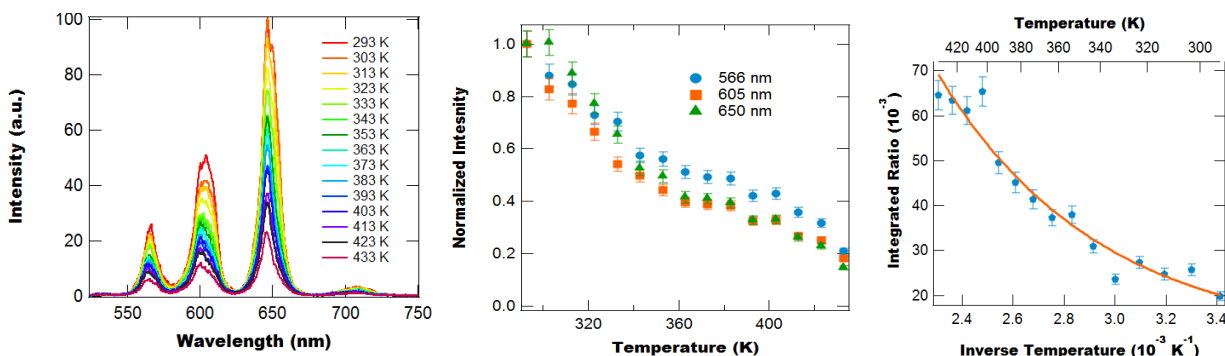


Figure 33. Temperature dependent emission spectra (left), emission intensities (center), and integrated ratio (right) of Sm(acac)₃(TOPO)₂ dissolved in HTPB.

The room temperature lifetimes and energy splitting of Sm(acac)₃(TOPO)₂/HTPB are: $\tau_{566} = (16.56 \pm 0.22) \mu\text{s}$, $\tau_{604} = (19.33 \pm 0.42) \mu\text{s}$, $\tau_{647} = (20.53 \pm 0.52) \mu\text{s}$, and $\Delta E = (0.1367 \pm 0.0086) \text{ eV}$.

Sm(acac)₃

Figure 34. shows the molecular structure and Figure 35. shows a microscope image of Sm(acac)₃. The complex consists of a Sm³⁺ ion surrounded by three acac ligands. While this material, without the TOPO ligands, appears to dissolve into HTPB, a later analysis appears to indicate that the material forms finely dispersed clumps in the binder and doesn't completely dissolve.

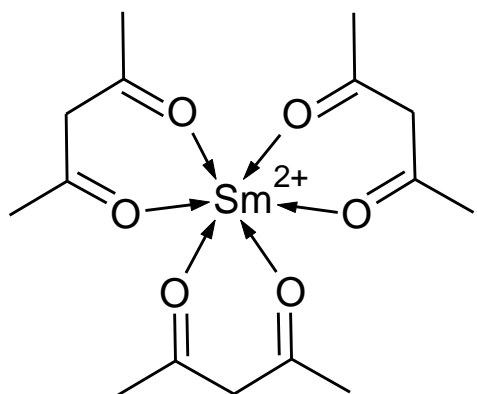


Figure 34. Molecular structure of **Figure 35.** Microscope image of $\text{Sm}(\text{acac})_3$.

The FTIR spectra shown in Figure 36. show that the acac ligand is present in the material, and Figure 37. shows the red emission for irradiation with 254 nm light.

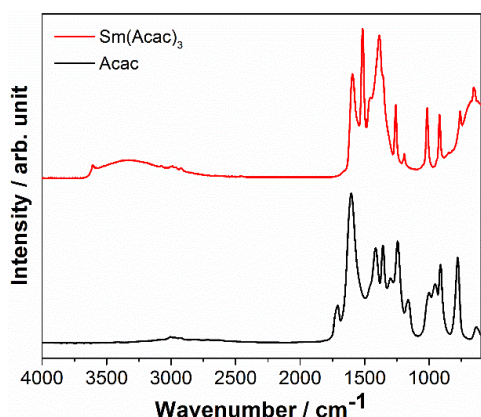


Figure 36. FTIR of $\text{Sm}(\text{acac})_3$.



Figure 37. Image of $\text{Sm}(\text{acac})_3$ irradiated by 254 nm light.

Figure 38. shows the temperature-dependent emission spectra, the emission intensities, and the integrated ratio of $\text{Sm}(\text{acac})_3$ in HTPB.

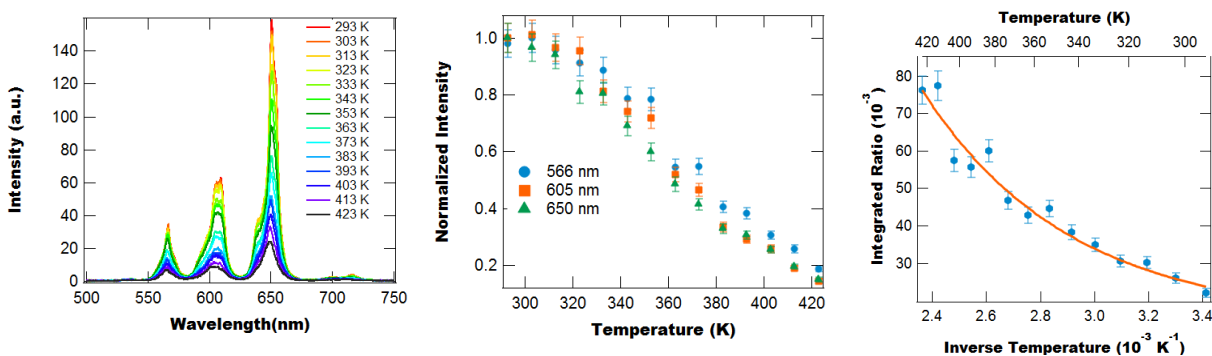


Figure 38. Temperature-dependent emission spectra (left), emission intensities (center), and integrated 535 nm/566 nm ratio (right) of $\text{Sm}(\text{acac})_3$ in HTPB.

The room temperature lifetimes and energy splitting of $\text{Sm}(\text{acac})_3/\text{HTPB}$ are: $\tau_{566} = (18.95 \pm 0.32) \mu\text{s}$, $\tau_{604} = (17.26 \pm 0.20) \mu\text{s}$, $\tau_{647} = (17.77 \pm 0.28) \mu\text{s}$, and $\Delta E = (0.0976 \pm 0.0035) \text{ eV}$.

$\text{Dy}(\text{acac})_3$

Figure 39. shows the molecular structure and Figure 40. shows a microscope image of $\text{Dy}(\text{acac})_3$. The complex consists of a Dy ion surrounded by three acac ligands. While this material, without the TOPO ligands, appears to dissolve into HTPB, a later analysis appears to indicate that the material forms finely dispersed clumps in the binder and doesn't completely dissolve.

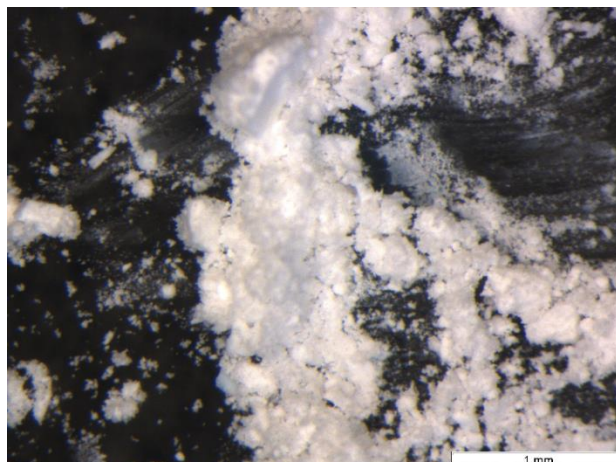
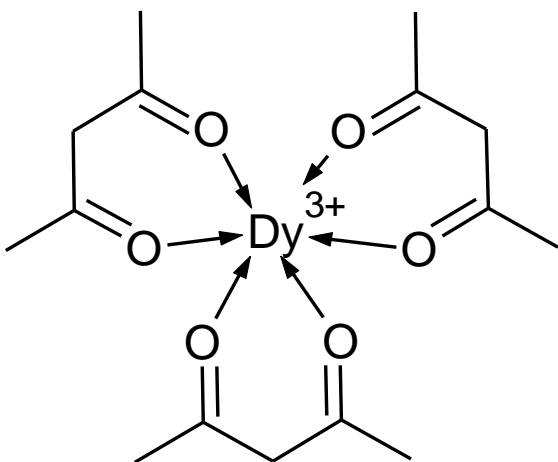


Figure 39. Molecular structure of $\text{Dy}(\text{acac})_3$. **Figure 40.** Microscope image of $\text{Dy}(\text{acac})_3$.

The FTIR spectra shown in Figure 41. show that the acac ligand is present in the material, and Figure 42. shows the emission for irradiation with 254 nm light.

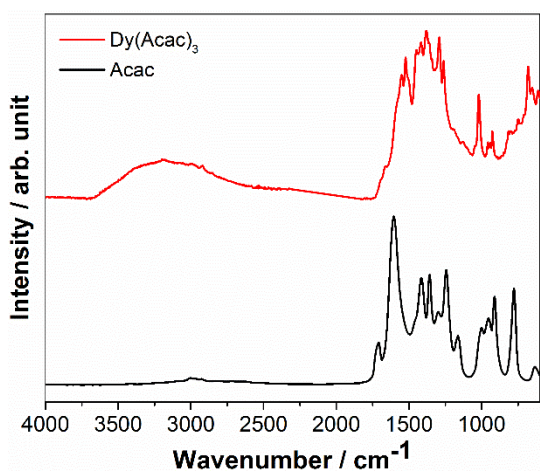


Figure 41. FTIR of $\text{Dy}(\text{acac})_3$.

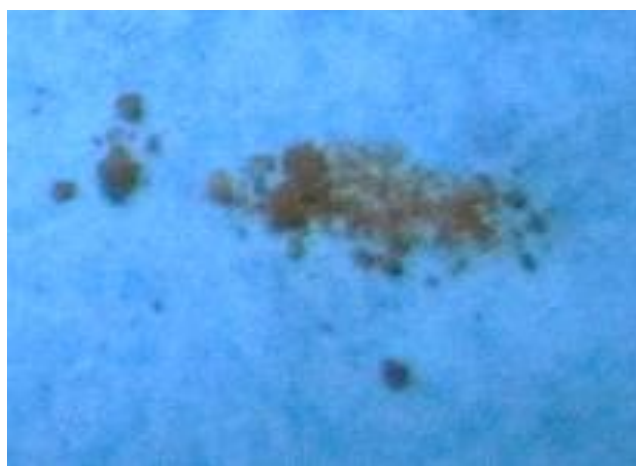


Figure 42. Image of $\text{Dy}(\text{acac})_3$ irradiated by 254 nm light.

Figure 43. shows the temperature-dependent emission spectra, the emission intensities, and the integrated ratio of Dy(acac)₃ in HTPB.

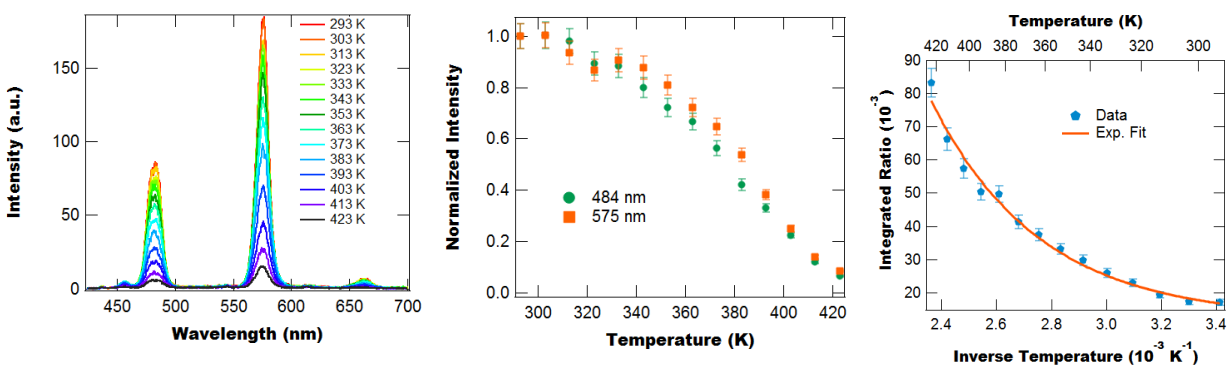


Figure 43. Temperature-dependent emission spectra (left), emission intensities (center), and integrated ratio (right) of Dy(acac)₃ in HTPB.

Sm(2-ethyl hexanoate)₃

This material was found to be not suitable for our purposes as it has a low quantum efficiency.

Sm(hfa)₃(TOPO)

Having tested the fluorinated version of the best MC from the previous year we next turn to testing the fluorinated version of the best dye, which was determined to be Sm(acac)₃(TOPO). The chemical structure of the fluorinated version – Sm(hfa)₃(TOPO) (SHT) – is shown in Figure 44. We first compare SHT's lifetime to that of SAT by considering their PL decays for the PL intensity at 650 nm, which are shown in Figure 45. From Figure 45 we find that SHT has a significantly longer lifetime than SAT. Table 4 tabulates the lifetimes for both the Dy and Sm complexes which have undergone fluorination.

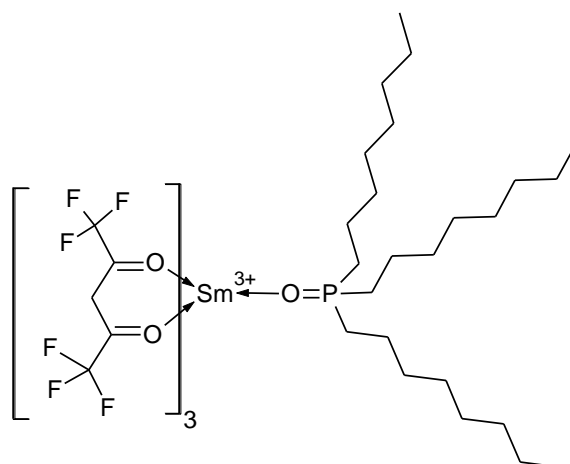


Figure 44. Schematic of Sm(acac)₃(TOPO).

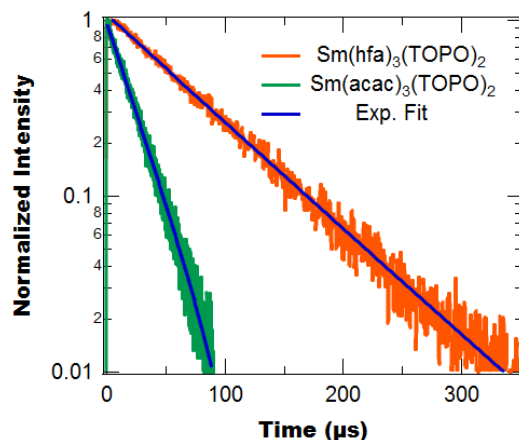


Figure 45. Normalized intensity at 648 nm as a function of time for $\text{Sm}(\text{hfa})_3(\text{TOPO})_2$ and $\text{Sm}(\text{acac})_3(\text{TOPO})_2$.

Table 4. Lifetimes of different Dy and Sm complexes

Complex	Lifetime (μs)
Dy:Y(acac) ₃ (DPEPO)	21.34 \pm 0.22
Dy:Y(hfa) ₃ (DPEPO)	3.39 \pm 0.65
Sm(acac) ₃ (TOPO) ₂	21.35 \pm 0.12
Sm(hfa) ₃ (TOPO) ₂	71.44 \pm 0.24

From Table 4 we find that the H-F substitution results in the Sm complex's lifetime increasing by 335%, while the Dy complex's lifetime is reduced to 16% of its original lifetime. To understand the different behavior between the two systems we note that the T_1 energy of hfa is 2.77 eV, the energy of Dy's $^4F_{9/2}$ level is 2.59 eV, and the energy of Sm's $^4G_{5/2}$ level is 2.21 eV. This means that the energy difference between Dy's $^4F_{9/2}$ level and hfa's T_1 level is 0.18 eV, while for Sm the energy difference is 0.56 eV.

Efficient energy transfer occurs when the energy difference between the ligand's T_1 energy level and the main emissive state of the lanthanide is greater than 0.23 eV [21]. Since the Dy complex's energy difference violates this requirement, energy back transfer (from lanthanide to ligand) is most likely occurring, leading to a decrease in the lifetime. Since the Sm complex has a larger energy difference it is found to benefit from the stabilizing effect of the H-F substitution.

Having considered the influence of fluorination on the PL lifetime of SAT, we prepare a 5 wt% SHT/HTPB sample to determine its thermal performance. This is performed by measuring its emission spectra at different temperatures using 355 nm excitation. Figure 46 shows the emission spectra at different temperatures, with the spectra found to quench surprisingly quick. To quantify the decrease in intensity as a function of temperature we plot the peak intensity at 650 nm as a function of temperature in Figure 47a, where the intensity is normalized such that the room temperature is unity.

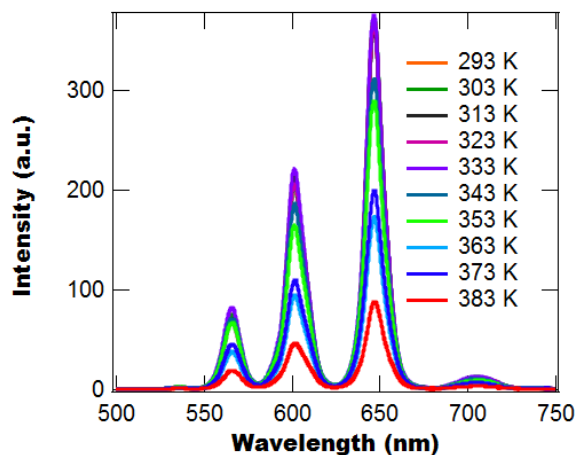


Figure 46. Emission spectra of SHT/HTPB for different temperatures.

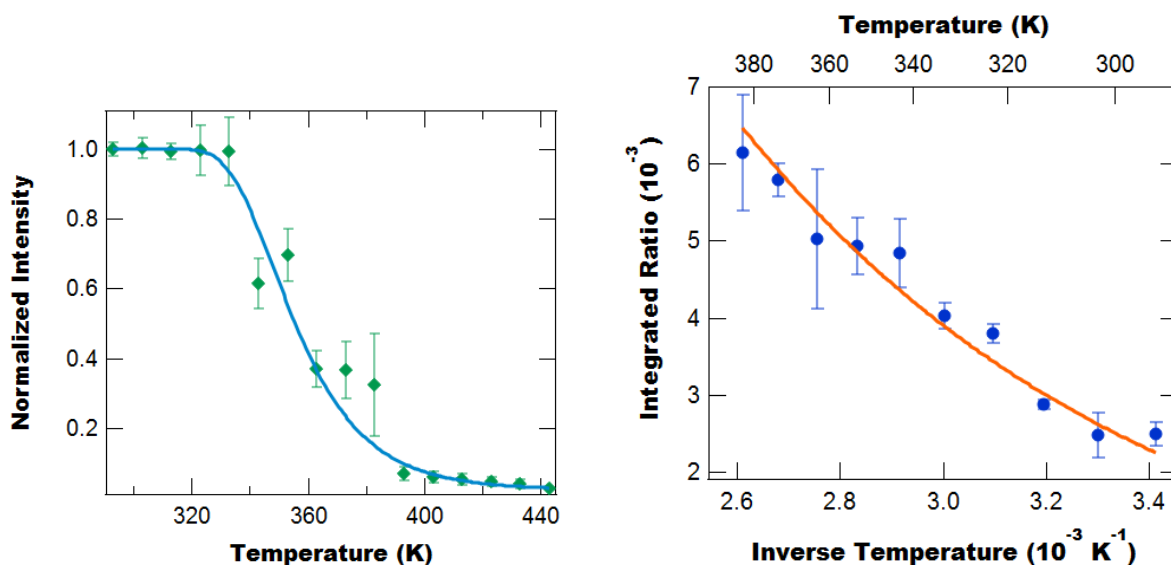


Figure 47. (a) Normalized intensity as a function of temperature and (b) the integrated intensity ratio (545/650) as a function of inverse temperature.

From Figure 47a we find that the peak intensity begins decreasing at a temperature of approximately 330 K, with the decay's half-temperature being 360 K. This is significantly lower than for SAT/HTPB, which had a half-temperature around 420 K. One possible explanation for this difference is that the SHT may be thermally degrading at a lower temperature than SAT. From our measurements thus far we have observed that after heating SHT/HTPB up to the 400 K range that the decrease in intensity is not fully reversible, which suggests thermal degradation of the SHT. To better understand this, we are planning to perform TGA/DSC on SHT and SAT.

With the behavior of the 650 nm peak intensity as a function of temperature quantified, we next turn to considering the integrated intensity ratio of the 545 nm and 650 nm peaks as a function of inverse temperature, which is shown in Figure 47b. From Figure 47b we

find that the integrated intensity ratio behaves as an exponential as a function of inverse temperature with the energy splitting found to be $\Delta E = (112.9 \pm 5.9) \times 10^{-3}$ eV and the amplitude parameter is found to be $A = 0.198 \pm 0.041$. These values are similar to those obtained for SAT, which is expected.

These results, in combination with the long lifetime of SHT, paint a mixed picture of the usefulness of SHT. On the one hand the material has a long lifetime and appears to be more efficient than SAT, but on the other hand it appears to thermally degrade at a lower temperature than SAT. For long duration measurements these results suggest that the SHT is not a good material. However, for short duration heating, such as during shock, the SHT may not have time to thermally degrade, meaning that the thermal degradation issue may be irrelevant

Dy(acac)₃(TOPO)₂ and Dy(hfa)₃(TOPO)₂

For initial shock experiments it was determined that the host material for the TCT phosphors should be an organic solvent which has a known equation of state (i.e., benzene, CCl₄, or nitromethane). We therefore tested the solubility of SAT in each of these solvents and settled on CCl₄ as an appropriate solvent. While SAT dissolves in CCl₄ optical measurements showed that the emission is relatively weak and insufficient for shock measurements. This failing was determined to be due to the Sm³⁺ ions having weaker emission than Dy³⁺ ions. Therefore, we next prepared Dy³⁺-based versions of the two dyes: Dy(acac)₃(TOPO)₂ (DAT) and Dy(hfa)₃(TOPO)₂ (DHT), with Figure 48 showing the chemical structure of both dyes.

During initial development of DAT it was discovered that the reaction result in two compounds, one which is soluble and the other insoluble. Using filtration it is possible to separate the two compounds out, which we subsequently use FTIR to identify (see Figure 49). The insoluble component is identified as Dy(acac)₃ and the soluble part is Dy(acac)_x(TOPO)_y.

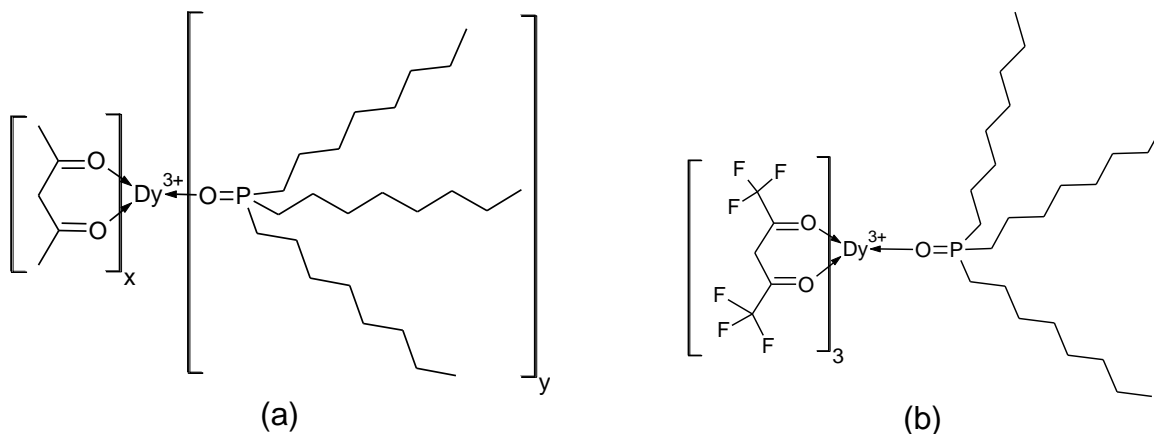


Figure 48. Schematic of the chemical structure of DAT (a) and DHT (b).

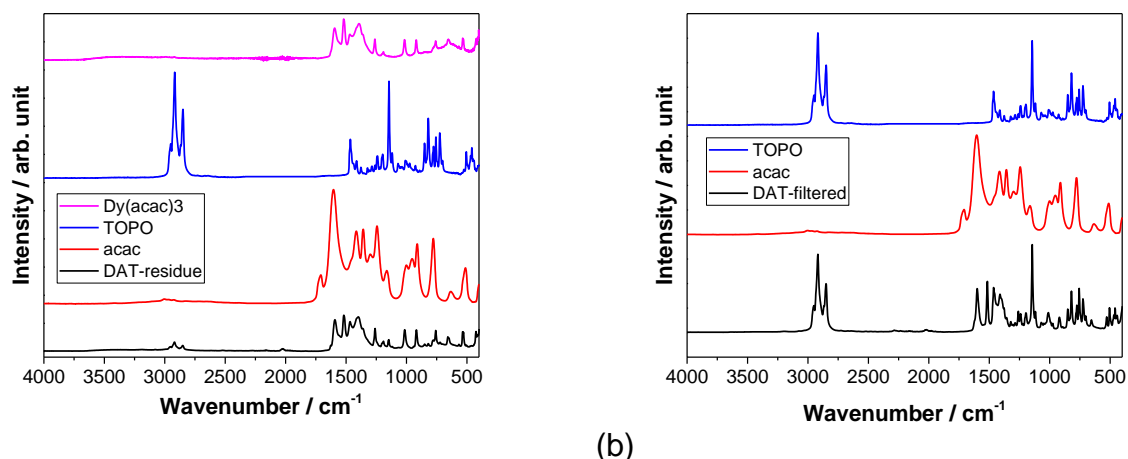


Figure 49. FTIR spectra of: (a) insoluble part and (b) soluble part of $\text{Dy}(\text{Acac})_x(\text{TOPO})_y$.

Next, we prepare DHT for testing. Unlike its Sm counterpart (SHT), which is a solid, DHT is a viscous compound (see image in Figure 50a). Based on FTIR spectra (Figure 50b) we find that both compounds have similar chemical compositions.

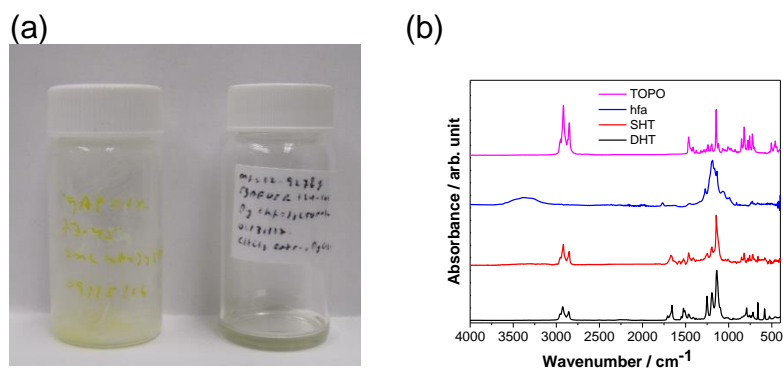


Figure 50. (a) SHT, rgAFOSR77-45 (left), and DHT, rgAFOSR124-101 (right) samples. (b) The corresponding FTIR spectra.

After synthesizing DAT and DHT we disperse them in CCl_4 at a 5 wt% concentration and perform spectroscopic characterization of the samples. Note that we prepare two separate DAT samples: one in which the insoluble DA is filtered out and one in which both components remain. Figure 51 shows the PL spectra of three different samples (filtered and unfiltered DAT/ CCL_4 and DHT/ CCL_4). From Figure 51 we find that the DHT has very poor emission while the unfiltered DAT/ CCl_4 has decent emission strength, but the filtered DAT/ CCl_4 far out performs either material.

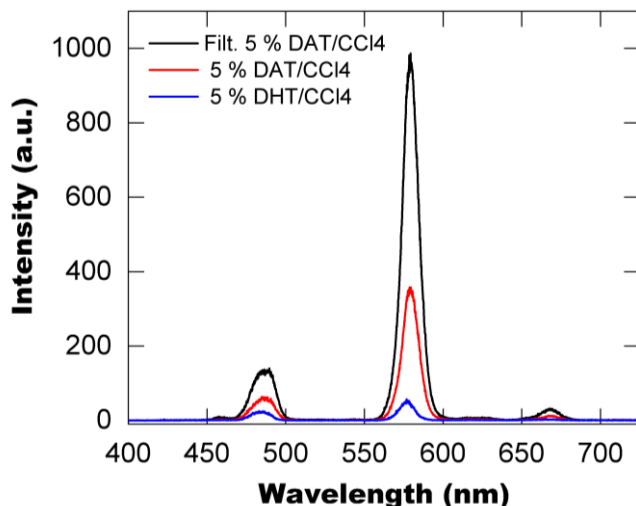


Figure 51. PL spectra (excited using 355 nm) of different Dy dyes doped into CCl₄ with a concentration of 5 wt%.

In addition to measuring the PL spectra of the different samples we also measure their PL lifetimes as determined from the time resolved decay of the 480 nm peak. Table 5 shows these lifetimes, with both the filtered and unfiltered DAT/CCl₄ having similar lifetimes of approx. 24 μ s, while the DHT is found to have a relatively short lifetime of approximately 550 ns. This short lifetime can be attributed to the relative spacing of the energy levels of Dy and hfa, which is found to violate Latva's empirical rule, resulting in back energy transfer from the Dy ion to the ligands.

Table 5. Luminescence lifetimes (measured at 575 nm) of Dy dyes in CCl₄.

Material	Lifetime
Filt. DAT/CCl ₄	24.05 \pm 0.25 μ s
DAT/CCl ₄	23.74 \pm 0.35 μ s
DHT/CCl ₄	545.6 \pm 4.8 ns

Having demonstrated that DAT/CCl₄ is a suitable material for PL measurements, we now characterize the influence of DAT concentration on DAT/CCl₄'s PL. We prepare a series of DAT/CCl₄ samples (rgAFOSR147-117-X) with four different DAT concentrations, whose PL spectra are shown in Figure 52. From Figure 52 we find that the emission intensity increases as a function of intensity (at least through 10 wt%). While the intensity is found to increase with concentration, it is found to behave sublinearly due to concentration quenching.

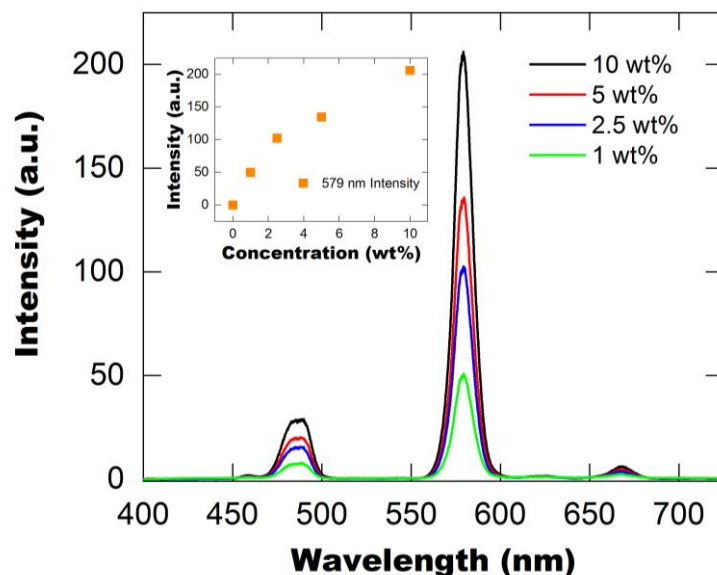


Figure 52. PL spectra (using 355 nm excitation) for different concentrations of DAT in CCl_4 . Inset: Intensity at 579 nm as a function of concentration.

With the influence of DAT concentration on the PL spectrum determined, we next determine the effect of temperature on DAT's emission. As CCl_4 has a boiling point of approximately 350 K and is hazardous, it is not a good host for temperature-dependent measurements. Therefore, we instead dope DAT into HTPB/IPDI polyurethane and perform temperature-dependent measurements on this system.

Figure 53 shows the PL spectrum of DAT/HTPB for different temperatures, with the emission found to decrease with increasing temperature due to thermal quenching. Using the spectra in Figure 53 we calculate the integrated intensity as a function of temperature, from which we determine calibration parameters of $E = 0.104 \pm 0.012$ eV and $A = 1.054 \pm 0.020$. We also determine a half-intensity temperature of 370 K. Note that this is for temperatures sustained over extended periods of time and it may be different for shock conditions.

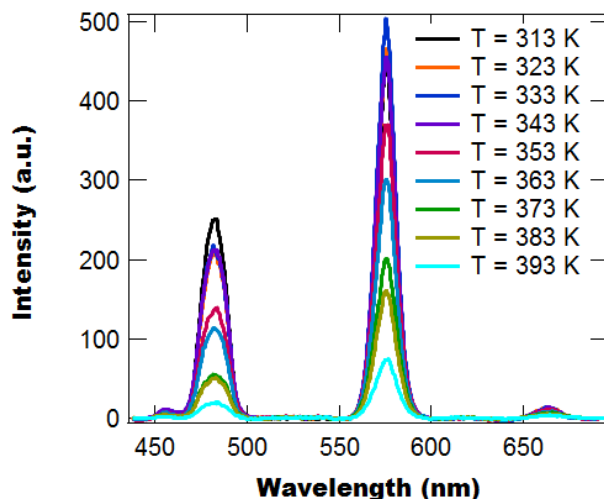


Figure 53. Temperature dependent PL Spectra of DAT/HTPB.

The above results for the evaluation of the different materials are summarized in Table 6.

Table 6. Summary of materials tested to date and comments on their viability as 2CT phosphors. Highlighted materials are probably the best candidates for dye and MCs.

Material Type	Material	Current Formulation Viable?	Notes
MC	Dy(acac) ₃ (Phen)	Y	Broad ligand emission, 10:90 is best concentration
MC	Dy(4-BBA) ₃ (TPPO) ₂	Y	Strong thermal quenching, but works with lower concentration
MC	Dy(PBI) ₃ (DPEPO)	N	Absorbs in blue
MC	Dy(Acac)₃(DPEPO)	Y	Excellent thermal response and longest lifetime. Most likely the best candidate.
Dye	Sm(2-ethyl hexanoate) ₃	N	Low QE
Dye	Sm(TOPO)₂(Acac)₃	Y	Strong emission. Outside of polymer it starts browning ~ 130 C.
Dye	Sm(Acac) ₃	Y	Peak structure differs from other Sm systems
Dye	Dy(Acac) ₃	Y	Excellent thermal response

E. Initial Temperature Measurements

Using $\text{Dy}(4\text{-BBA})_3(\text{TPPO})_2$, we performed heating measurements using a 120 W strip heater. The emission spectra were measured as a function of time, see Figure 54. Subsequently, the 2-color fluorescence temperature was calculated using the previously established calibration, see Figure 55. The calculated temperatures are in excellent agreement with the thermocouple temperature. The reduced absolute intensity at higher temperatures leads to more noisy data.

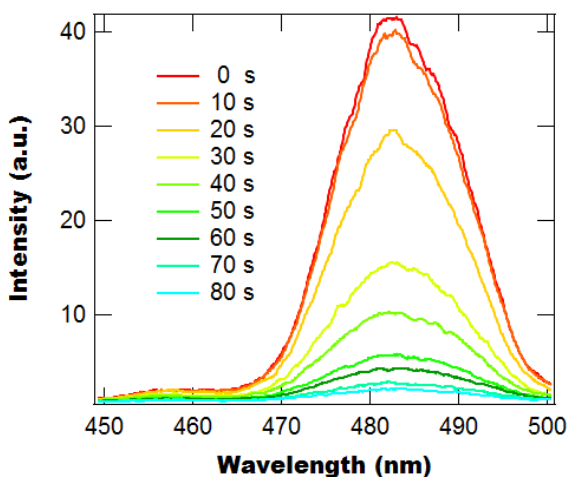


Figure 54. Emission spectra of $\text{Dy}(4\text{-BBA})_3(\text{TPPO})_2$ as the sample is heated up over time.

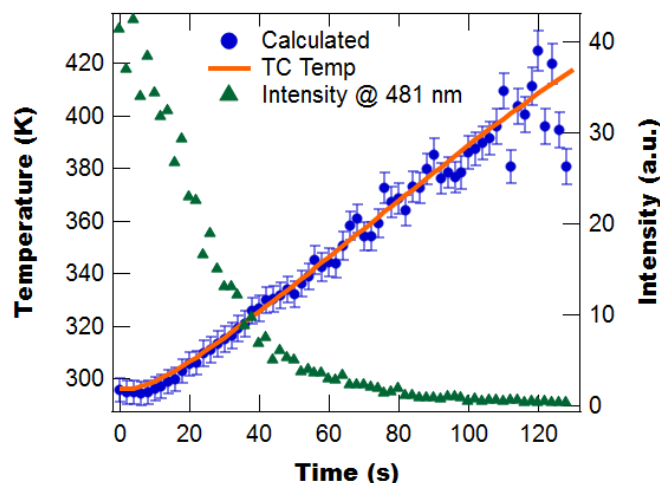


Figure 55. Calculated and measured temperature of $\text{Dy}(4\text{-BBA})_3(\text{TPPO})_2$. Also shown is the emission intensity.

F. Initial Imaging

Figure 56 shows false-color microscope images of $\text{Dy}(\text{acac})_3$ in HTPB at room temperature under different conditions: ceiling light illumination, 355 nm irradiation, 355 nm irradiation and 460 nm filter, and 355 nm irradiation and 485 nm filter. The structure in the upper right part of the sample is an air bubble. The image in the bottom right shows some bright spots indicating areas of increased emission intensity. At room temperature, these areas are only apparent when using the 485 nm filter. Very little emission is expected in the 460 nm filter image. The bright spots indicate that $\text{Dy}(\text{acac})_3$ does not completely dissolve in HTPB.

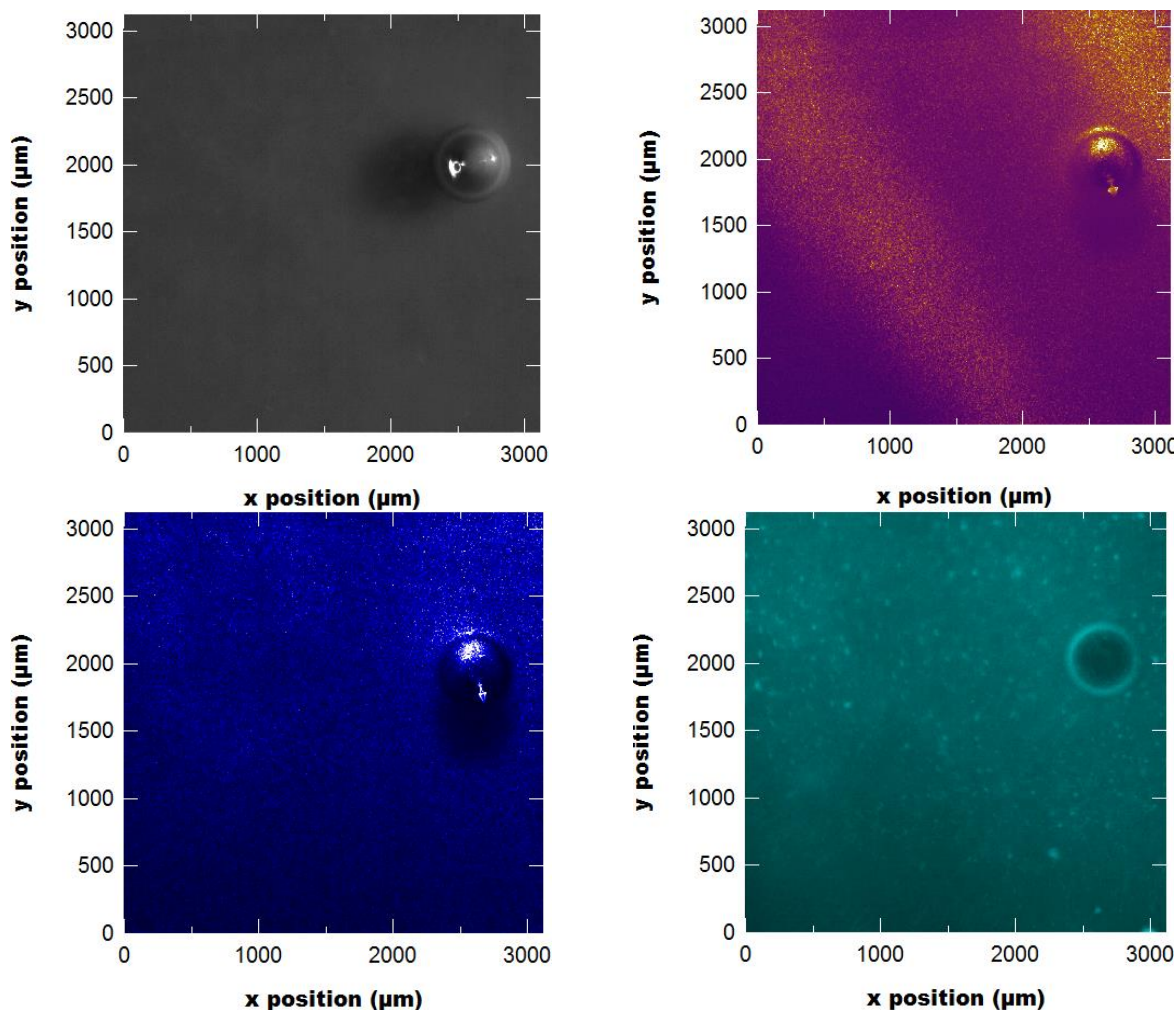


Figure 56. Microscope images of $\text{Dy}(\text{acac})_3$ in HTPB under different conditions: Daylight illumination (top left), 355 nm irradiation (top right), 355 nm irradiation and 460 nm filter (bottom left), and 355 nm irradiation and 485 nm filter (bottom right). The structure in the upper right part of the sample is an air bubble.

G. Two-Color Thermometry Imaging

System Setup

The initial TCT imaging (TCTI) system consists of a frequency tripled Nd:YAG laser (Continuum Powerlite II, 355 nm, 10 Hz, 8 ns), a Synrad Firestar f100 CO_2 laser, delay generators, various optics, and a two-color imaging system (two Pt Grey Grasshopper 3 cameras, a beam splitter and narrow bandpass filters). Figure 57 shows a schematic of the system. Note that the CO_2 laser beam spot diameter is approximately 1 mm, while the UV pump spot size has a diameter of approximately 13 mm.

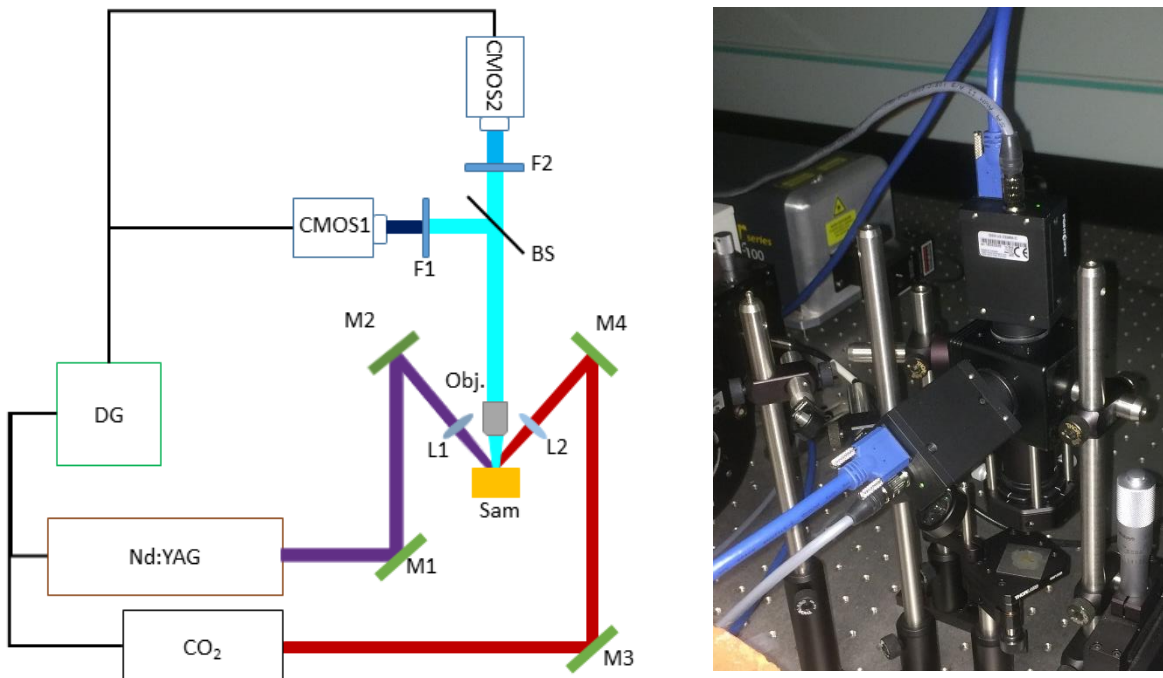


Figure 57. Laser heating and TCT imaging setup schematic.

While setting up and aligning the optics for the TCTI system is the first step for imaging the temperature profile during laser heating, the second – more difficult – step is synchronizing the various components in time. Initially we tried to use the trigger signal from the Continuum laser (which is synced to the output pulse) to trigger the cameras, but discovered that the Grasshopper cameras have a trigger latency of $46.7 \mu\text{s}$ and a timing jitter of $3.8 \mu\text{s}$, such that by the time the cameras triggered the samples luminescence had already decayed below the cameras detection limit. Given this latency it is therefore necessary to trigger the cameras before the excitation laser pulse using a delay generator. Additionally, since the timing jitter is longer than our typical gate delay of $1 \mu\text{s}$ we cannot effectively perform gated measurements using the Grasshopper cameras.

Having determined the issues related to the camera timing we next turn to triggering the Nd:YAG laser to be synchronized with the CO₂ laser pulse. This involves externally triggering the Nd:YAG laser to fire at the end of the CO₂ laser pulse. While this should be a simple procedure, we discover that due to a quirk with the Continuum laser the triggering scheme is more complicated. To correctly trigger the Nd:YAG laser pulses requires two delay generators. The first runs in rep mode at 10 Hz to trigger the laser lamp, with the second one setup for single pulse mode, which triggers the Q-switch, CO₂ laser, and Cameras. Note that the optimal Q-switch delay is determined to be $295 \mu\text{s}$ for our laser. Figure 58 shows a schematic of the time scheme.

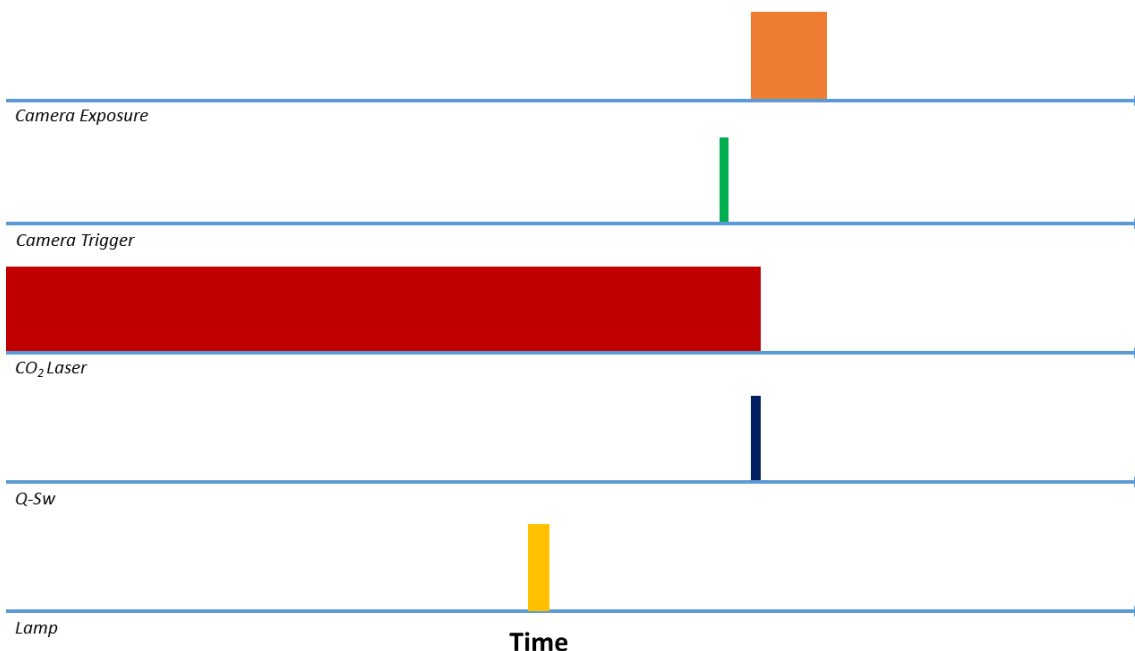


Figure 58. Schematic of TCTI trigger timing.

Room Temperature Imaging

To begin our imaging trials, we first perform two-color imaging at room temperature to determine the geometric considerations of the TCTI system. Figure 59 shows the single-excitation pulse emission images for each color with a Dy(acac)₃/HTPB sample. Comparing the two images in Figure 59 we find that the raw images are not perfectly matched in orientation, with the 480 nm image being flipped vertically and rotated with respect to the 460 nm image. This difference in orientation is due to the influence of the beam splitter and the fact that the cameras do not align perfectly in the filter cube.

In addition to determining the orientation of the images in Figure 59 we also find that there is a wide variation in emission intensity across the sample, which is due to the 355 nm pump being noisy. To improve uniformity, we plan to use a beam homogenizer. Also note that the small bright spots in the images are most likely due to clumping of the Dy(acac)₃.

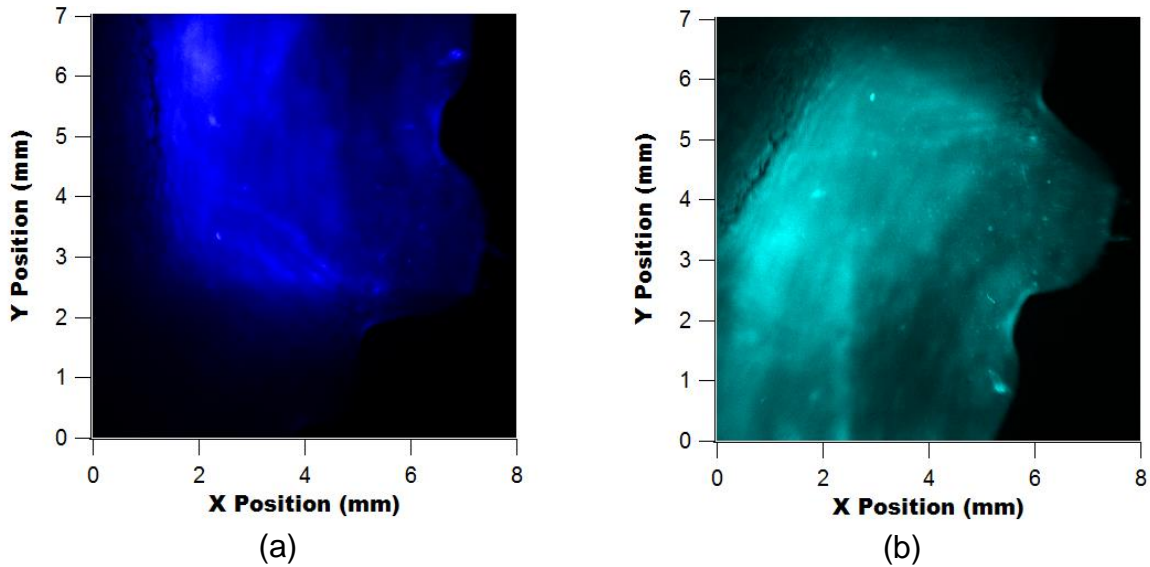


Figure 59. Raw images for 460 nm filter (a) and 480 nm filter (b).

Since we desire to take the ratio of the two images it is necessary to spatially transform one of them to match with the other. For this purpose we choose to transform the 480 nm image. This transformation consists of flipping the image about the horizontal axis and rotating the image about the out-of-page axis. Figure 60 shows the spatially transformed 480 nm image and the 460 nm image demonstrating that they are now spatially aligned. Note from Figure 60 that the dark line in the upper left corners now correspond as well as the bright spot in the upper right corners.

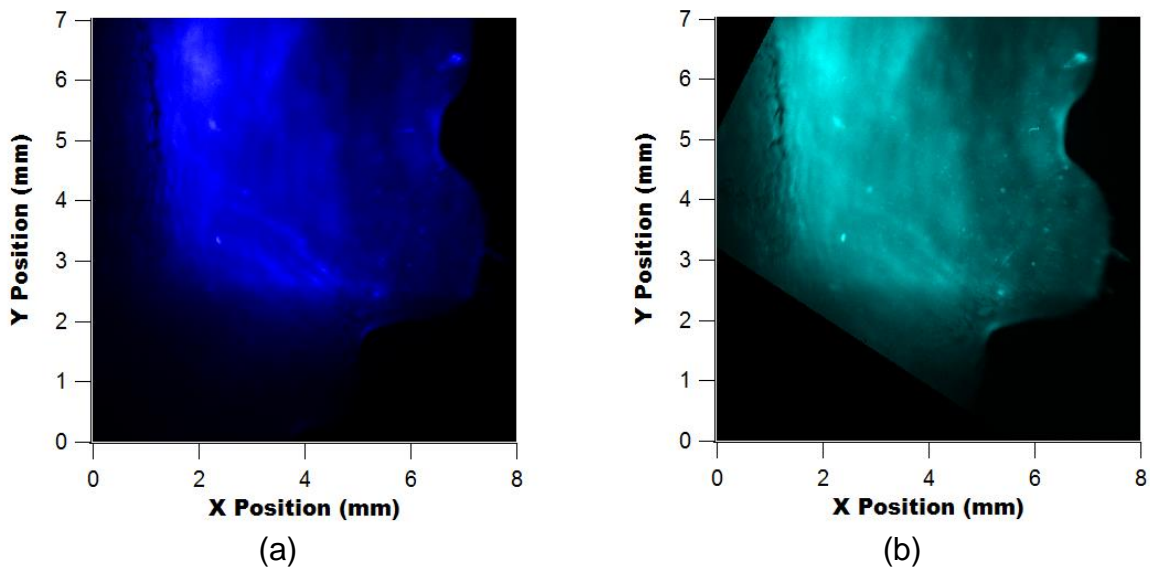


Figure 60. Room temperature image for 460 nm (a) and spatially transformed 480 nm filter image (b).

Laser Heating Tests

With the fundamental operation of the TCTI system determined, we next perform laser heating with the TCTI system taking a single-shot image during heating. For this purpose the CO₂ laser is turned on to full power for 1.795 ms with the sample being imaged immediately after the heating laser is turned off. Figure 61 shows the two-color images of the heated area, which appears as a dark spot on the sample due to thermal quenching of the emission.

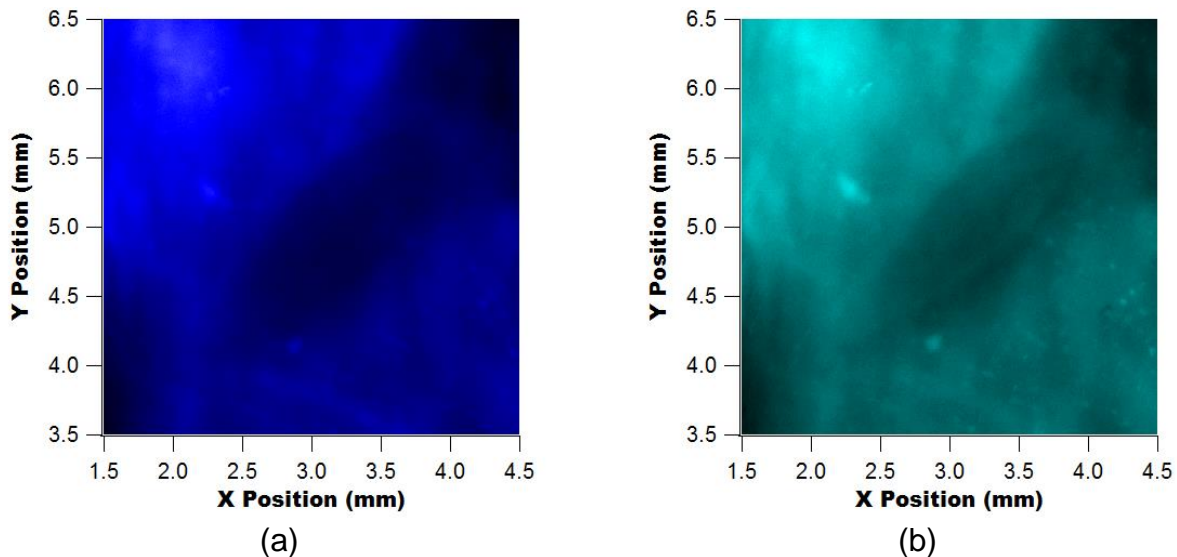


Figure 61. Images of laser heated sample for the 460 nm filter (a) and 480 nm filter (b).

Initially, to find the ratio between the two images we took the pixel-by-pixel ratio and found that the resulting ratio image was very noisy. This was due to noise fluctuations of individual pixels. Therefore, to improve the ratio image (and its SNR) we next binned the pixels. For binning we average over all the pixels in a 10 x 10 area to form “super-pixels”. Once binned we then take the ratio of the two wavelengths with the resulting ratios (for both room temperature and laser heating) shown in Figure 62. From Figure 62 we can clearly see the area heated by the CO₂ beam as compared to the room temperature ratio, with the heated area being roughly elliptical which is consistent with the CO₂ laser beam shape. We also note from Figure 62 that there appears to be hot-spots in the heating profile, which is consistent from what we know of the CO₂ laser’s beam shape.

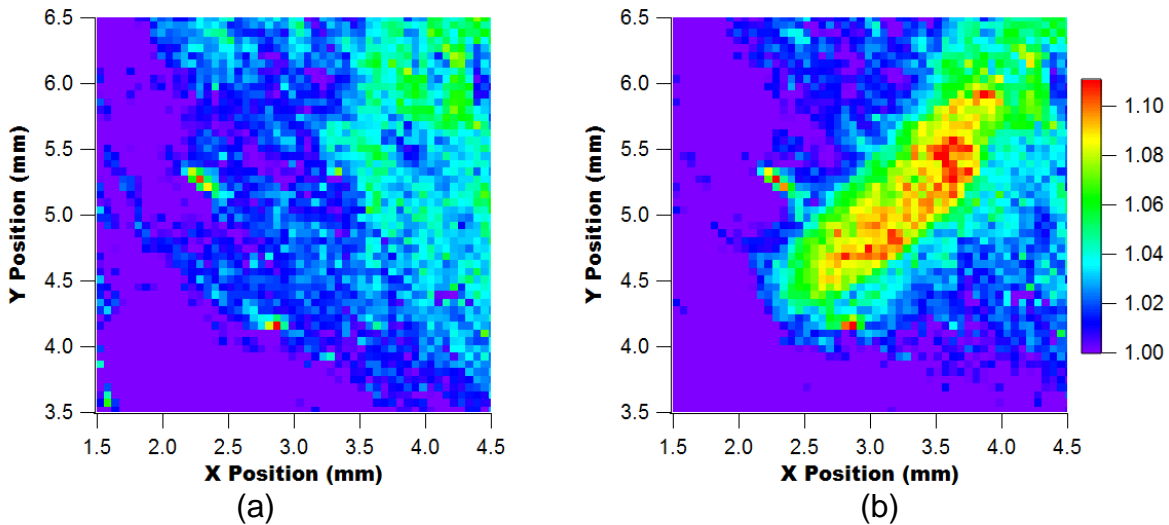


Figure 62. 460 nm/480 nm image ratio for sample at room temperature (a) and for 1.795 ms laser heating (b).

While we can roughly see the heating laser’s profile in Figure 62, it is not ideal as the background ratio variations overlap with the heating profile. We therefore take the difference between the heated ratio and the room temperature ratio to produce a cleaner image of the heated area, as shown in Figure 63. From Figure 63 we can more clearly see the heating beam profile, with the elliptic Gaussian shape now obvious.

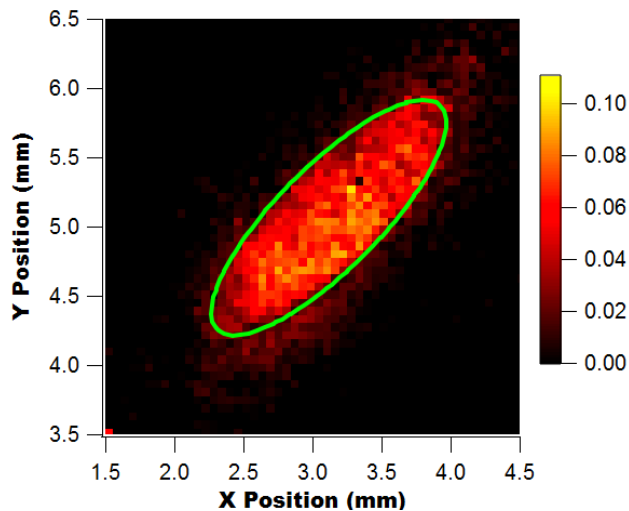


Figure 63. Difference between heated ratio and room temperature ratio for laser heating with a duration of 1.795 ms.

After testing the TCTI system with laser heating for 1.795 ms, we next test the system for the shorter duration of 1 ms. Currently, due to the lack of gating we find that it is difficult to resolve heating for durations less than about 1 ms, as the background intensity is very strong. Figure 64 shows the difference between the heated and room temperature ratios for the 1 ms heating, with the distribution found to be less smooth than for the longer heating. This is most likely due to the hot spots in the beam providing the majority of the

heating with the heat being transferred to the surrounding medium. Since the heating duration is shorter there is less time for thermal transport and therefore the heat is more localized. Also note that the very bright spot in the upper right of the beam ellipse corresponds to a defect in the sample and therefore the large ratio is most likely due to sample inhomogeneity.

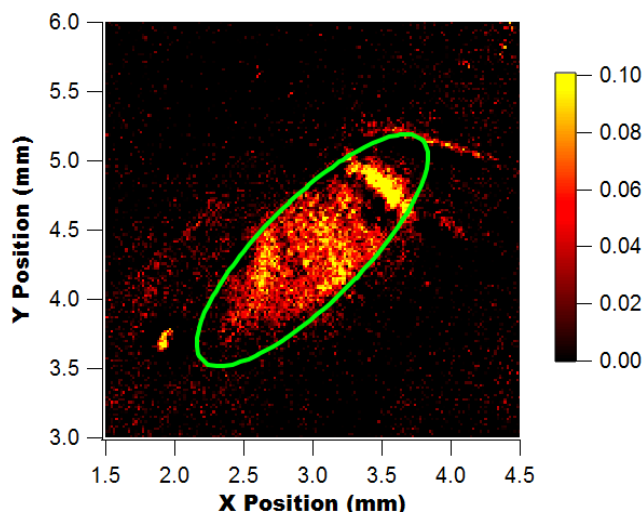


Figure 64. Difference between heated and room temperature ratios for laser heating with a duration of 1 ms.

Thus far we have considered laser heating of uniform samples with the TCT phosphor dissolved into the polymer host. Next, we consider laser heating of TCT molecular crystals dispersed in polymer, namely we use Dy:Y(acac)₃(DPEPO) dispersed in HTPB. Figure 65 shows a fluorescence image of the sample through the 460 nm filter with the brighter MCs highlighted using a particle analysis algorithm. Note that there is a wide range of particle sizes and the algorithm has only highlighted the largest and brightest particles.

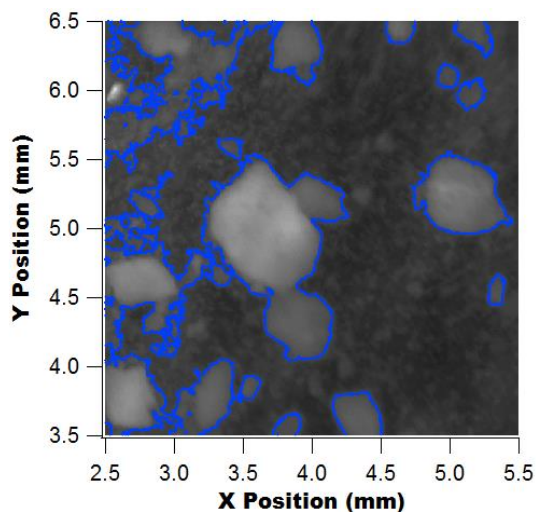


Figure 65. Fluorescence image (through 460 nm filter) for Dy:Y(acac)₃(DPEPO) in HTPB with a loading concentration of 5 wt%.

In addition to getting a sense of the particle size distribution and density in the polymer we also find that the particles result in light scattering and that the polymer has a broad emission under 355 nm illumination. These two effects lead to difficulties in the analysis of the spectral ratios as 1) the polymer emission currently cannot be removed from the particle emission due to the lack of gating and 2) the scattered light causes the entire sample to appear fluorescent and not just the particles themselves.

Despite these difficulties we still perform laser heating tests on the sample to determine how detrimental these effects are. From attempting heating for several different times, we find that to see a change in fluorescence with the MC +polymer system the heating laser needed to be on for approximately 2 ms or longer. While we can't be certain based on optical measurements alone, this result is most likely due to a layer of polymer lying over the MCs.

This layer of polymer means that the polymer will absorb most of the heating laser's energy resulting in the polymer heating up faster than the underlying MCs, which will result in lower MC temperatures than those observed for the dye in polymer. Because of this effect we find that the change in ratio between heated and unheated is small and very noisy. Figure 66 shows the difference between the heated and room temperature ratios along with guidelines for the beam and particles. From Figure 66 we find that the majority of changes in ratio occur within the beam profile and the particle outlines, which is expected if the MCs are heating up. The splotchy nature of the heat profile is most likely due once again to the hot-spots in the CO₂ laser as well as the 3D nature of the crystals (i.e. some parts are closer to the surface than others).

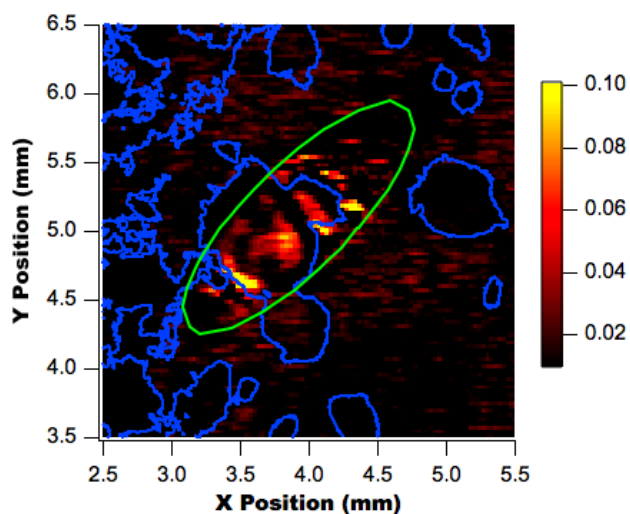


Figure 66. Difference between heated and room temperature ratios, with particle outlines and beam outline.

Upon closer inspection of Figure 66 we observe that the areas with the largest differences in ratios occurs near the boundaries of the particles in the heating beam. At this point, given the preliminary nature of these measurements, it is uncertain the source of this effect but there are several possibilities: 1) there really are hot spots at the boundaries

due to crystal geometry and the heating beam, 2) there is some scattering effect at the boundary (due to polymer heating) leading to the spectra being changed giving a different ratio, 3) some small misalignment during imaging and spatial transformation leads to an anomalous ratio difference, or 4) some combination of the above.

To determine which of these effects is most likely we will need to perform further measurements. At this point we are inclined to believe that it is either mechanism 1 or 2, as the third mechanism (misalignment) would result in ratio fluctuations to appear at every particle, but currently we only see it in the heated region.

H. Upgraded TCTI system

In the previous year, we built a demonstration TCTI apparatus using two CMOS cameras. Using this system, we demonstrated the TCTI approach but ran into timing issues due to the design of the CMOS camera. Additionally, this system involved complicated image transformations as the system was not optimized for one-to-one mapping of the images between cameras. However, this system at least allowed us to demonstrate the technique and get a better grasp on the issues involved in a TCTI system.

During this last year, using AFOSR DURIP funds, we built an upgraded TCTI system, consisting of a Cairn Splitcam system (with a variety of optical filters), two Princeton Instruments PI-Max 4 1024i CCD cameras, and an Oportek Radiant 355 HE OPO system for tunable excitation of our temperature sensors to optimize the PL signal.

The Cairn Splitcam system consists of two Cairn Optosplit devices connected to a Cairn Twincam device. The Twincam device evenly splits the incident image into two paths which pass through the Optosplits. The Optosplits then split the image into two spectrally filtered images which are passed to a single detector. By using two Optosplits with the PI-Max 4 1024i CCDs we are able to take four temporally resolved PL images due to the PI-Max 4's double image feature. This will eventually allow us to perform time-resolved TCTI during shock compression at four separate time points.

Pulsed Laser TCTI Demonstration

We demonstrate the TCTI technique using pulsed laser heating of a heterogeneous sample. For these experiments we only used one leg of the Splitcam system (i.e., a single Optosplit) and a single camera. Excitation was achieved using a frequency-tripled Nd:YAG laser with the heating laser pulse provided by a 100 W CO₂ laser. Figure 67a shows an image of the heating system, while Figure 67b shows a schematic diagram of the system.

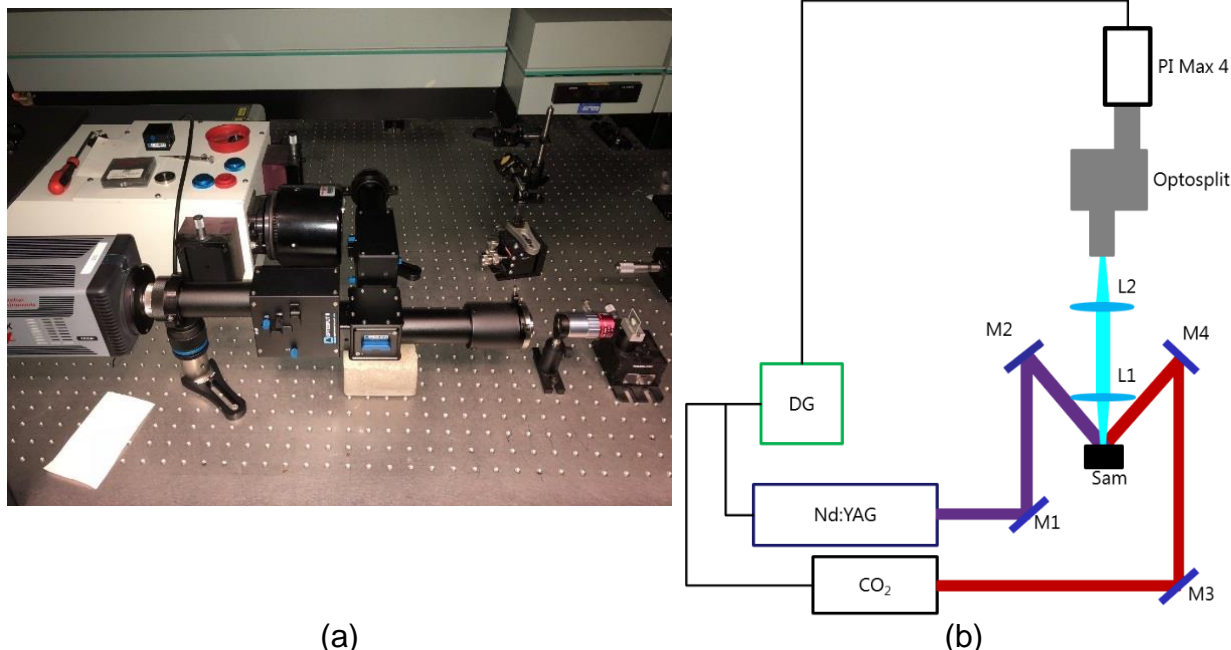


Figure 67. Image (a) and schematic (b) of TCTI setup using the Splitcam system and PI-Max 4 ICCD.

For our heterogeneous samples, we blend Dy:YAG and DYAD crystals with hydroxyl-terminated polybutadiene/isophoronediiisocyanate/Bis(2-ethylhexyl)adipate (HTPB/IPDI/DEHA) poly-urethane at a 75/25 and 50/50 crystals/polyurethane weight ratio, respectively, see Appendix A for more details on the sample preparation and composition. The crystal/polyurethane mixture is then poured onto a glass slide and cured overnight at ambient temperature. Figure 68 shows images of example samples.

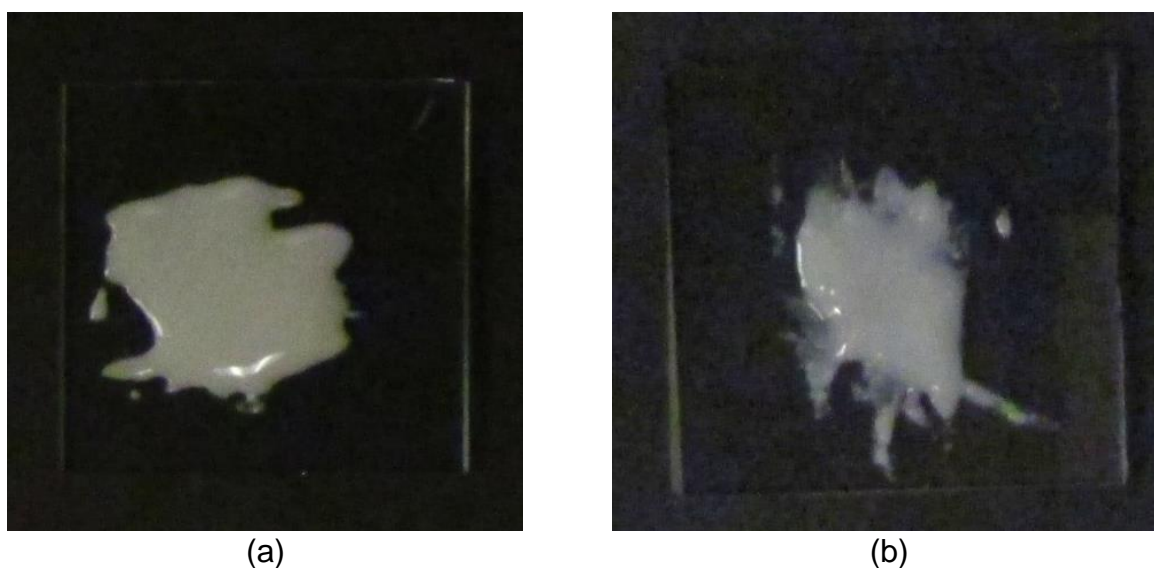


Figure 68. Pictures showing the crystals/polyurethane composites on 1"x1" glass that are used for imaging: (a) Dy:YAG/polyurethane and (b) DYAD/polyurethane.

After preparing the samples and setting up the TCTI system, the next step is to correctly determine the timing of the various components. To begin, we consider two key timing details: (1) that the ideal Q-switch delay is 295 μs meaning that once the lamp fires (at a rate of 10 Hz) the sample will be excited 295 μs later (as there is minimal delay between the Q-switch firing and the laser pulse exciting the sample), and (2) our temperature sensors have relatively short lifetimes ($\approx 20 \mu\text{s}$ for DYAD and $\approx 800 \mu\text{s}$ for Dy:YAG) compared to the heating pulse duration (10-100 ms). Given these two factors we setup our experimental timing such that the CO₂ laser fires at t_0 , followed by the flashlamp at $t_0+w-305 \mu\text{s}$, the Q-switch at $t_0+w-10 \mu\text{s}$, and the ICCD gate starting at t_0+w (with an ICCD gate width of 750 μs). Figure 69 shows a schematic of the timing with t_0 marking the start of the CO₂ laser pulse and w being the gate width of the laser pulse. Note that this timing scheme measures the PL immediately following the laser heating pulse.



Figure 69. TCTI pulsed laser heating time scheme.

TCTI of Dy:YAG in HTPB

First, we tested Dy:YAG particles dispersed in HTPB. For these samples we limited our pulse heating widths from 10 ms to 100 ms as longer durations can burn holes in the polymer. Figure 70 shows example two-color images for heating durations of 0 ms, 50 ms, and 100 ms. The PL emission dominates in band 1 (470 nm – 520 nm) for the ambient measurement, with the PL intensity transferring into band 2 (440 nm – 470 nm) as the sample is heated.

After measuring the two-color images for different gate widths, we computed the spatially resolved intensity ratio for each image. This ratio is found to have a baseline spatial profile, which must be removed to determine the influence of heating. We therefore subtracted the ambient ratio image from the computed heated ratio images, with Figure 71 showing the resulting change in ratio for different heating pulse widths.

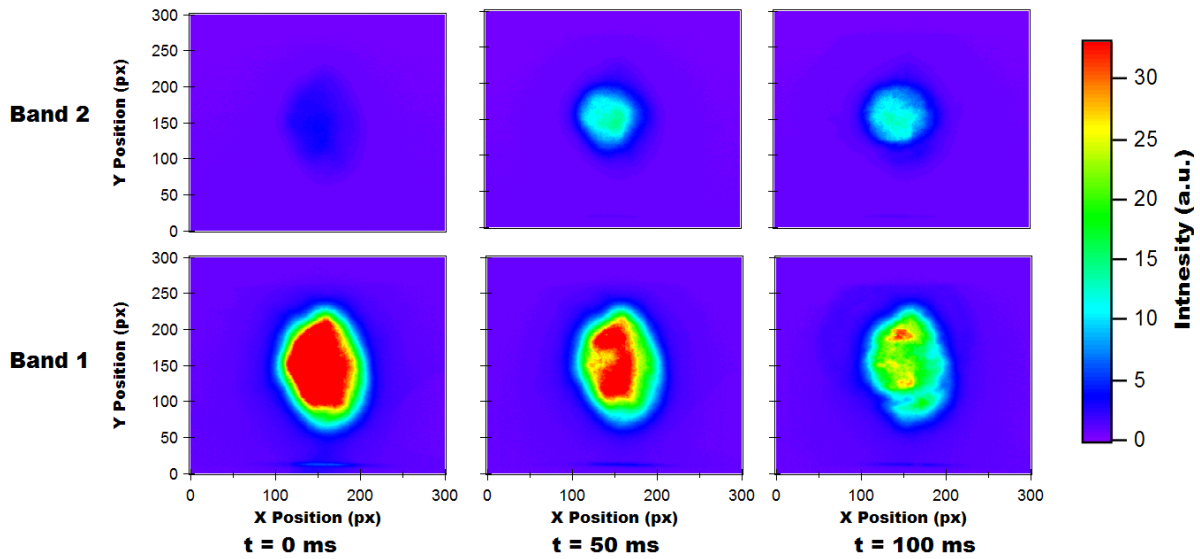


Figure 70. PL intensity in band 1 and band 2 during laser heating. As the temperature rises the intensity transfers from band 1 to band 2.

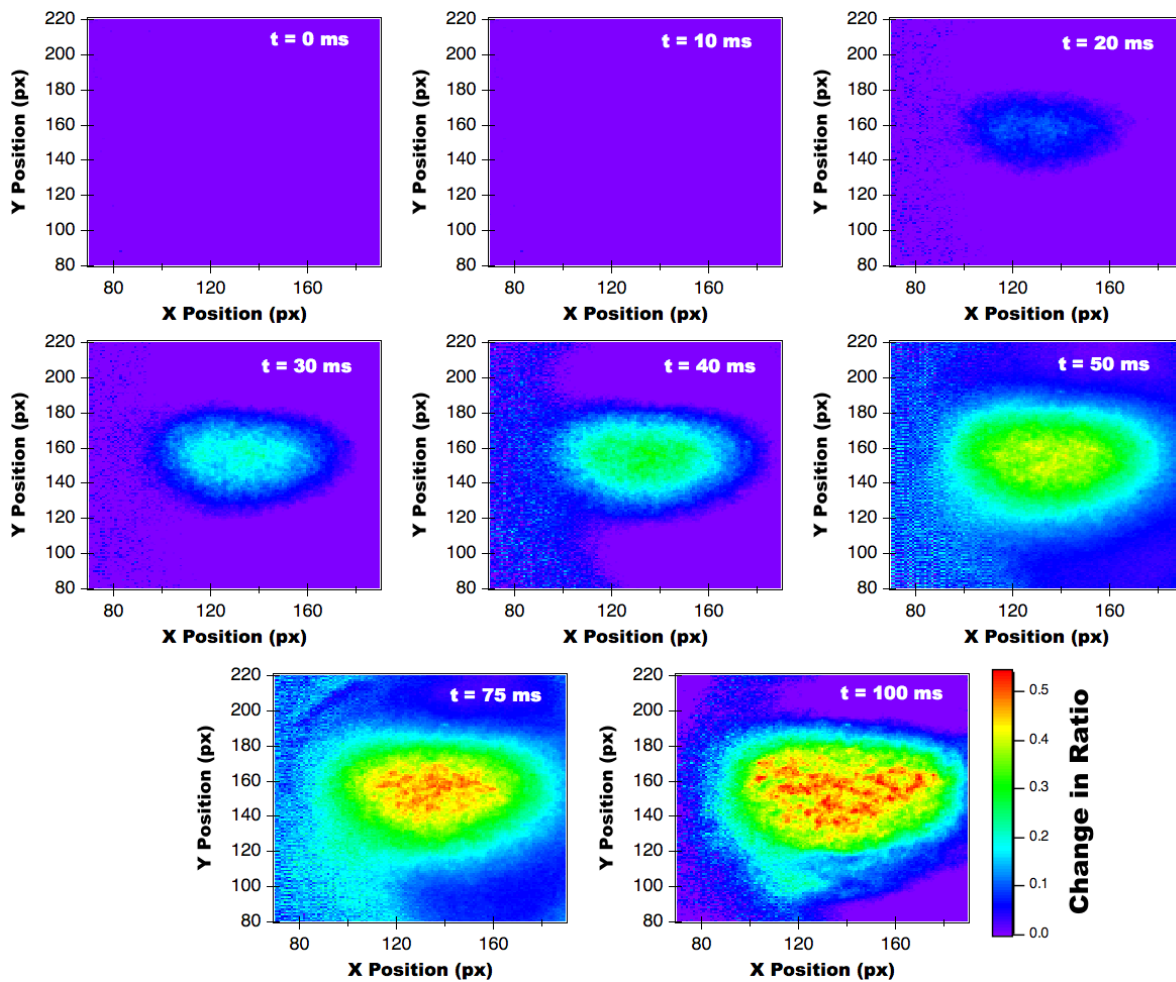


Figure 71. Change in intensity ratio images for different laser heating pulse lengths.

From Figure 71 we find several results: (1) the heating profile is elliptical, which corresponds to the CO₂ laser's known beam profile, (2) for durations < 20 ms there is very little change in the ratio, and (3) the hottest areas (largest ratios) are not uniformly distributed. This last observation is best observed by considering the ratio profile for the 100 ms heating pulse, which displays splotchy hot spots. These hot spots could either be due to poor CO₂ beam quality or nonuniformity in the sample. Unfortunately, it is impossible to determine which mechanism is responsible as the CO₂ laser used in these experiments is known to have a poor beam profile.

Having imaged the change in ratio for different heating pulse durations, we next convert these ratio profiles into temperature profiles. To do so we begin by writing the change in ratio Δr as a function of time,

$$\begin{aligned}\Delta r(t) &= r(t) - r(t_i), \\ &= r_0 + Ae^{-\frac{\Delta E}{kT}} - r_0 - Ae^{-\frac{\Delta E}{kT_i}}, \\ &= Ae^{-\frac{\Delta E}{kT}} - Ae^{-\frac{\Delta E}{kT_i}}, \\ &= Ae^{-\frac{\Delta E}{kT}} - D_i,\end{aligned}\tag{1}$$

Where T_i is the initial temperature at time t_i , A and ΔE are material parameters, r_0 is an offset parameter due to the optical setup, and D_i is a parameter related to the room temperature ratio that is given by

$$D_i = Ae^{-\frac{\Delta E}{kT_i}}.\tag{2}$$

For Dy:YAG, the material parameters are (on average) $A = 1.71$, and $\Delta E = 121.2$ meV, which results in $D_i = 0.0141$. With these parameters we rearrange Equation (1) to give the temperature as a function of time:

$$T = \frac{\Delta E}{k \ln \left[\frac{\Delta r(t) + D_0}{A} \right]}.\tag{3}$$

With Equation (3) and the change in ratios in Figure 71, we compute the temperature profiles at the different times, which are shown in Figure 72.

From Figure 72 we find that the heating profiles are elliptical, as expected, with the peak temperatures being near 1200 K. Interestingly, by comparing the different profiles at each time we find that the heated region increases as the time increases, which is consistent with heat diffusion from the laser spot into the surrounding materials. This heat transfer limits further heating, which leads to the temperature as a function of time being a nonlinear function (as discussed below).

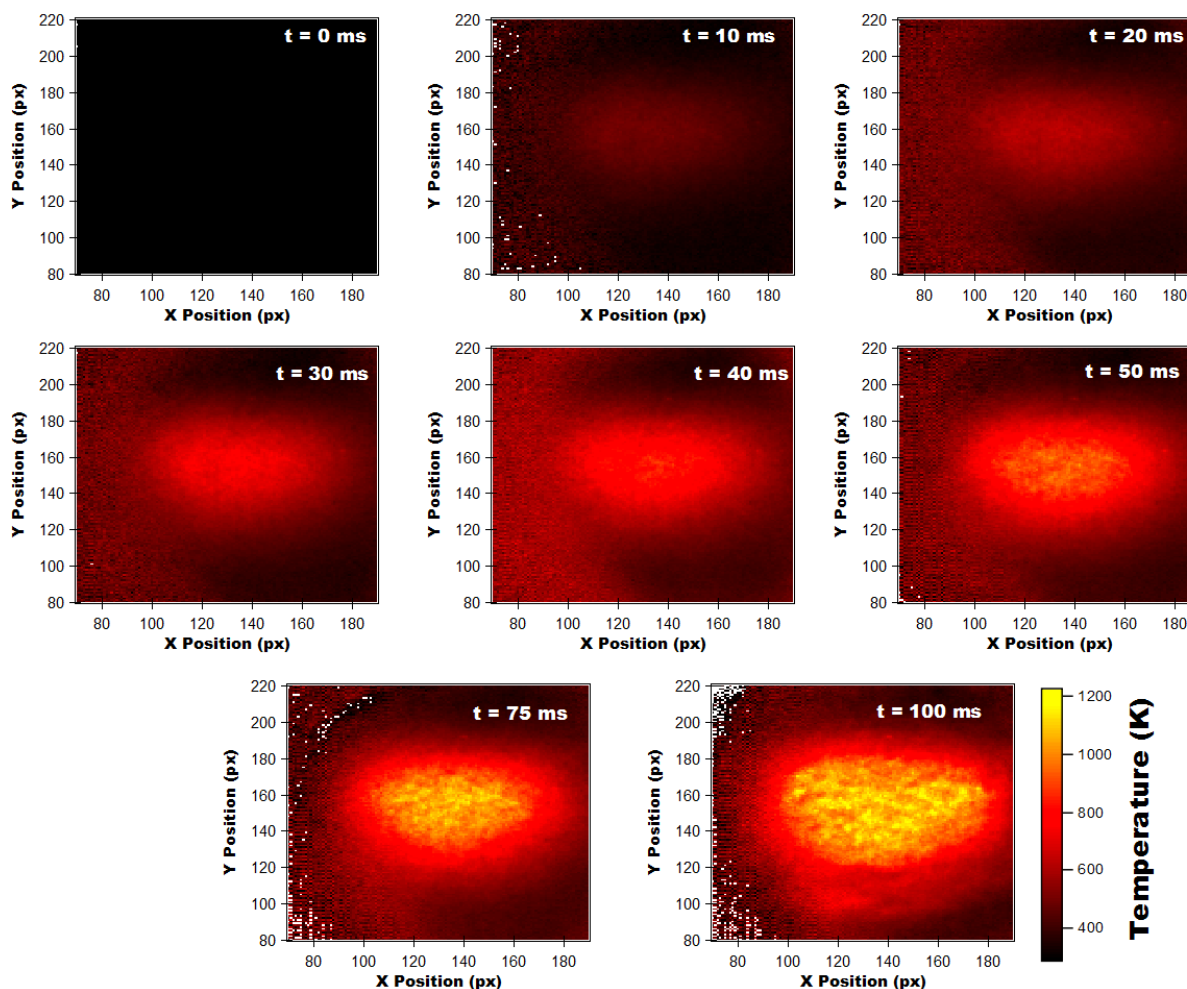


Figure 72. Temperature map at different times during pulsed laser heating. Note that the profile is elliptical, which corresponds to the underlying CO₂ laser beam profile.

TCTI of Dy:Y(acac)₃(DPEPO) in HTPB

Having demonstrated the TCTI technique with Dy:YAG, we next consider the performance of Dy:Y(acac)₃(DPEPO) as a TCT phosphor with the heating limited to pulse widths of 50 ms as further heating results in complete quenching of the phosphors PL. For brevity we suppress the PL and ratio images for Dy:Y(acac)₃(DPEPO) and instead turn directly to considering the measured temperature profiles, which are shown in Figure 73. Note that in Figure 73 we apply an elliptical mask to hide noise outside of the region of interest.

From Figure 73 we find that once again little to no heating is observed for durations < 20 ms. We also observe that the heated region for Dy:Y(acac)₃(DPEPO) has significantly more temperature variations than were observed for Dy:YAG. These variations are due to the Dy:Y(acac)₃(DPEPO) sample displaying more concentration inhomogeneity and a rougher surface than the Dy:YAG samples. Most likely this lower uniformity is due to the Dy:Y(acac)₃(DPEPO) particles being larger than the Dy:YAG particles.

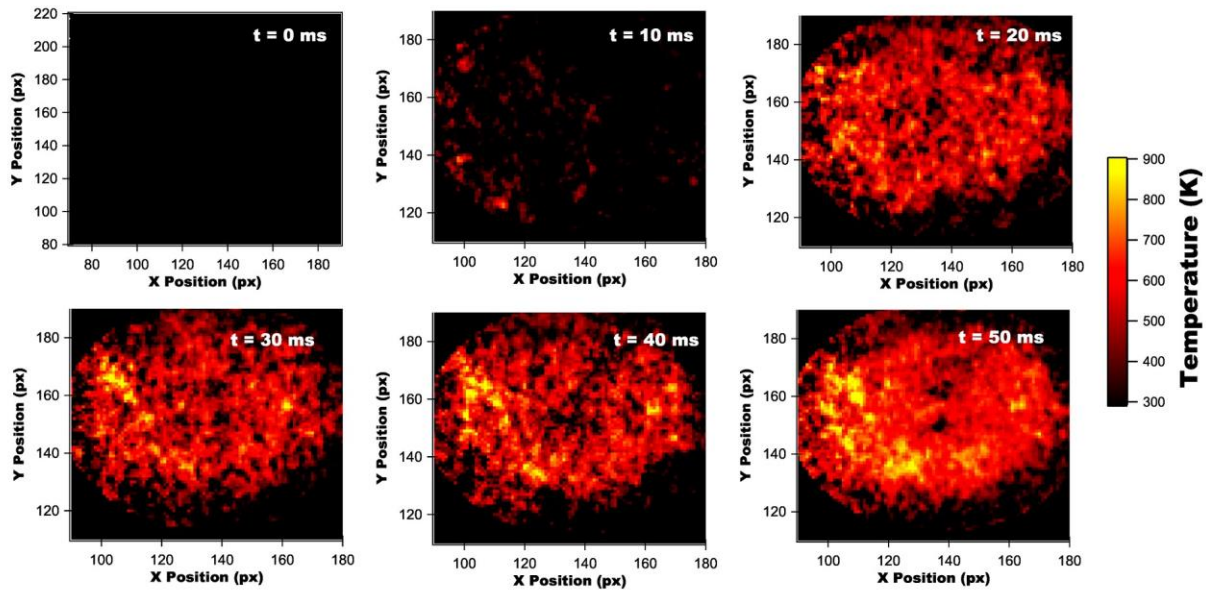


Figure 73. Temperature map at different times during pulsed laser heating of Dy:Y(acac)₃(DPEPO) dispersed in HTPB.

At this point we had planned on making a direct comparison of the full heating profiles of the two materials to demonstrate Dy:Y(acac)₃(DPEPO)'s performance as compared to Dy:YAG. Unfortunately, due to uniformity issues, this is not possible. While we cannot compare the full profiles, we can make some limited comparisons if we consider the regions in Figure 73 that correspond to the highest temperatures. The motivation for this comparison is as follows: (1) the same laser profile and power was used for both samples, which means for equally uniform samples the profiles should be identical. (2) the Dy:Y(acac)₃(DPEPO) crystals are larger and doped at a lower concentration, which means that the main impact of inhomogeneity will be voids and areas of lower concentration. Both of these will result in less heating and therefore lower temperatures. (3) The areas with the highest concentration of Dy:Y(acac)₃(DPEPO) crystals will therefore be heated the most similar to the Dy:YAG sample.

With these assumptions in mind we compare the average temperature in a 10 px circle centered at ($x = 110$, $y = 160$) for both materials, with the resulting temperatures shown in Figure 74. From Figure 74 we find good agreement between the two sensor materials, which demonstrates Dy:Y(acac)₃(DPEPO)'s suitability as a phosphor for TCTI. We also observe that both materials display an exponential heating curve, which is expected in the case of constant-power heating with heat diffusion. At early times the energy coming into the target area is far greater than the energy being transferred out, leading to the temperature increasing linearly. However, as the temperature rises the rate of heat loss to the surrounding material increases resulting in a net decrease in the heating rate. This continues until the rate of energy input is balanced by the heat transfer out of the region of interest, leading to a steady state temperature. Note that we do not reach the steady state temperature as we limit the pulse width to 50 ms.

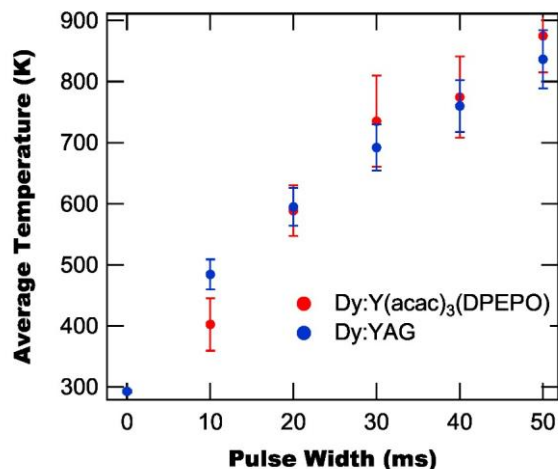


Figure 74. Average temperature in 10 px circle centered at $(x = 110, y = 160)$ for heating of both Dy:YAG and Dy:Y(acac)₃(DPEPO).

I. Shock Measurements

2017 Shots

The first plate-impact experiment was designed and conducted to examine time-resolved photoluminescence spectra of Dy(acac)₃(TOPO)₂ dye dissolved in CCl₄ under shock wave loading. Following the first experiment, the second experiment was conducted to evaluate the experimental reproducibility. The two photoluminescence bands, for the dye used in our experiments, are located at 455 nm and 485 nm wavelengths, respectively, and the emission life time is 24 μs [22]. This long lifetime allows the dye to be excited prior to impact. The intensity ratio of the two emissions bands $I_{455\text{nm}}/I_{485\text{nm}}$ is expected to increase with increasing temperature [22,23].

CCl₄ was chosen as a solvent because its temperature under shock compression has been well-characterized experimentally, and it does not luminesce near the dye emission wavelengths. The experiment was designed to multiply shock compress CCl₄/dye to ~12 GPa peak pressure. Previously, the temperature of pure CCl₄ at this configuration was measured to be 850 K through time-resolved Raman measurements [24].

Experimental Configuration

Figure 75 shows a schematic view of the experimental configuration. A CCl₄/dye mixture (10 weight % dye concentration) was sandwiched between two a-axis sapphire windows. The mixture was prepared 3 – 4 hours prior to the impact experiment. The sample volume was ~25.4 mm in diameter and ~250 μm thick. An a-axis sapphire flyer was mounted on a projectile and accelerated to about 530 m/s using the 2.5" bore gas gun. In our experiments, the a-axis sapphire remains elastic and transparent. Experimental parameters for the two experiments are provided in Table 7.

A 355 nm wavelength laser pulse (10 ns pulse duration, ~ 6 mJ energy) was used to excite the dye. The laser beam was delivered through an optical fiber and focused onto a sample (400 μm spot size). The photoluminescence signals were collected at 45 degrees angle and sent to a detection system through an optical fiber. The detection system consisted of a spectrometer (Acton SpectraPro 150 with 600 g/mm - 500 nm blaze), a streak camera (Imacon 500), an image intensifier (Photek MCP140) and a CCD camera (Princeton instrument 1300x1340). A long-pass filter was used to filter out the 355 nm wavelength excitation pulse. Additionally, scattered laser pulse was recorded using a fast PMT to provide a time fiducial. A series of electrical shorting pins were used to synchronize laser firing and a detector trigger with respect to impact. The excitation laser pulse was incident on a sample 0.5 μs before the impact. It should be noted that the laser energy for Expt. 1 was somewhat lower (4 mJ) than the energy for Expt. 2 (6 mJ).

The temporal resolution of our measurements was 50 ns, limited by the combination of the streak camera sweep rate (set to cover the experiment duration) and the fiber diameter (400 μm). The spectral resolution was 4.5 nm, limited by the spectrometer slit size which was maximized for the maximum throughput.

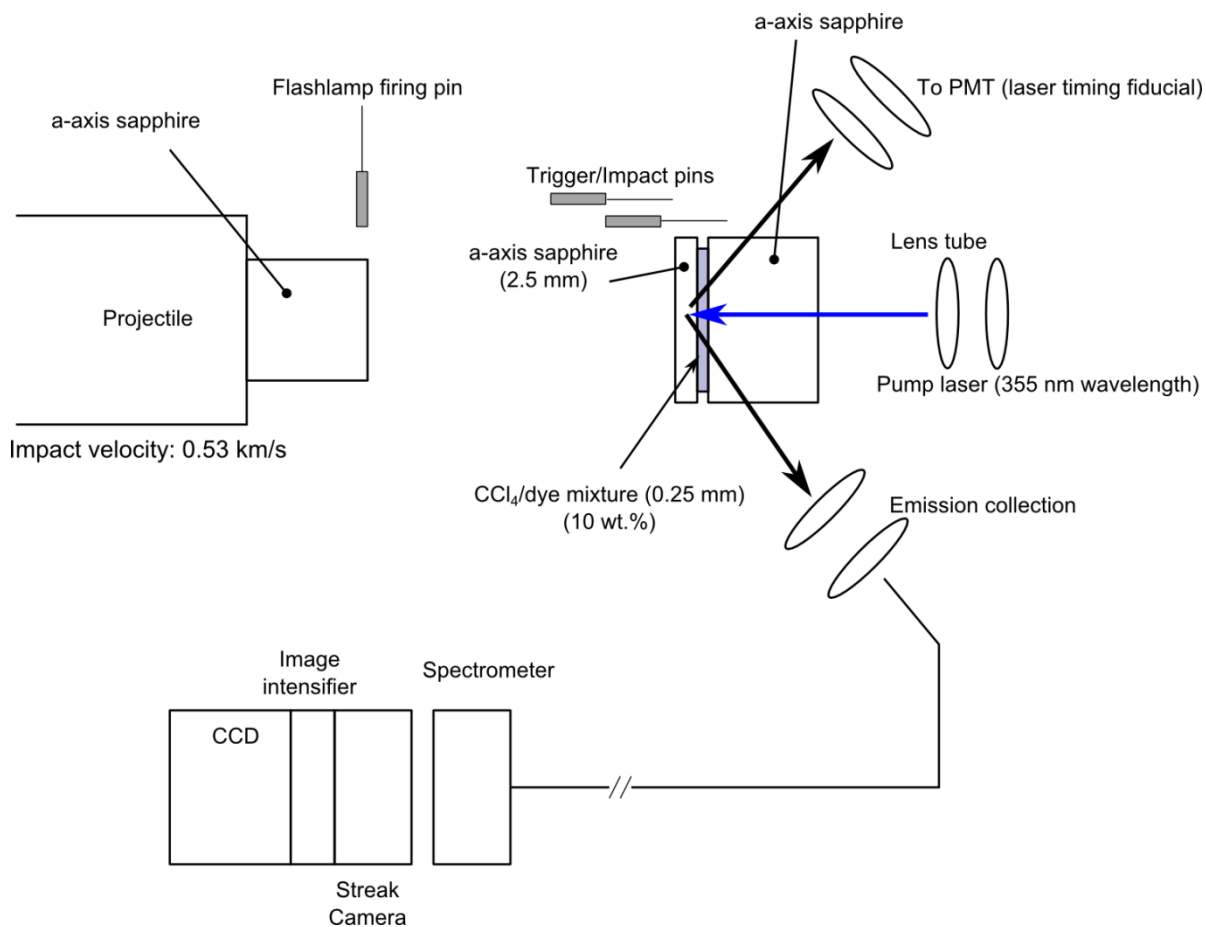


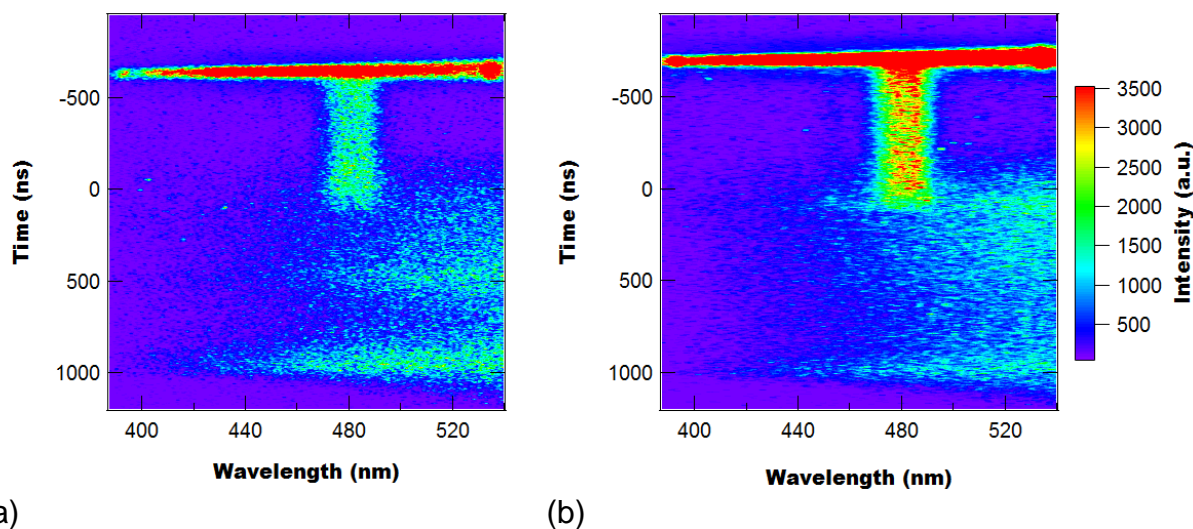
Figure 75. Schematic view of the experimental configuration (not to scale).

Table 7. Experimental parameters

Expt.	V_{impact} (km/s)	Dye concentration (weight %)	Sample thickness (mm)	Impactor thickness (mm)	Front window thickness (mm)	Rear window thickness (mm)
1 (17-512)	0.527	10	0.254	a-axis sapphire/12.7	a-axis sapphire/2.51	a-axis sapphire/12.7
2 (17-514)	0.528	10	0.266	a-axis sapphire/12.7	a-axis sapphire/2.48	a-axis sapphire/12.7

Shock Experiment Results

The primary data resulting from each shock experiment is a spectral streak recorded by the streak camera. Figure 76 shows the smoothed spectral streaks (smoothed in wavelength axis using 1.3 nm averaging) for both shot 1 and 2, with $t = 0$ being the time at which the shock enters the CCl_4 . Note that shot 2 is significantly brighter due to improved Q-switch timing. In both shots, the streaks show a bright broad emission when the laser pulse excites the sample, followed by a narrower area of bright emission corresponding to PL from the DAT, which remains relatively constant before the shock enters the CCl_4 followed by a quick decay in PL intensity. The introduction of the shock wave also results in a new broad background emission, whose source is currently unknown.

**Figure 76.** Smoothed streaks from shot 1 (a) and shot 2 (b).

In both shot measurements the emission from DAT is found to be completely quenched approximately 150 ns after the shock enters the CCl_4 . Figure 77 shows the average intensity of the 480 nm peak as a function of time during the shock experiment. From Figure 77 we find that the emission peaks due to the laser pulse, followed by a flat area as the long lifetime DAT emits PL, which quickly quenches once the shock enters the CCl_4 . This quenching may arise due to a number of factors including: temperature, pressure, and deformation of the ligands. Regardless of the underlying mechanism, the

shock results in the formation of additional nonradiative decay channels which causes the DAT to quickly quench.

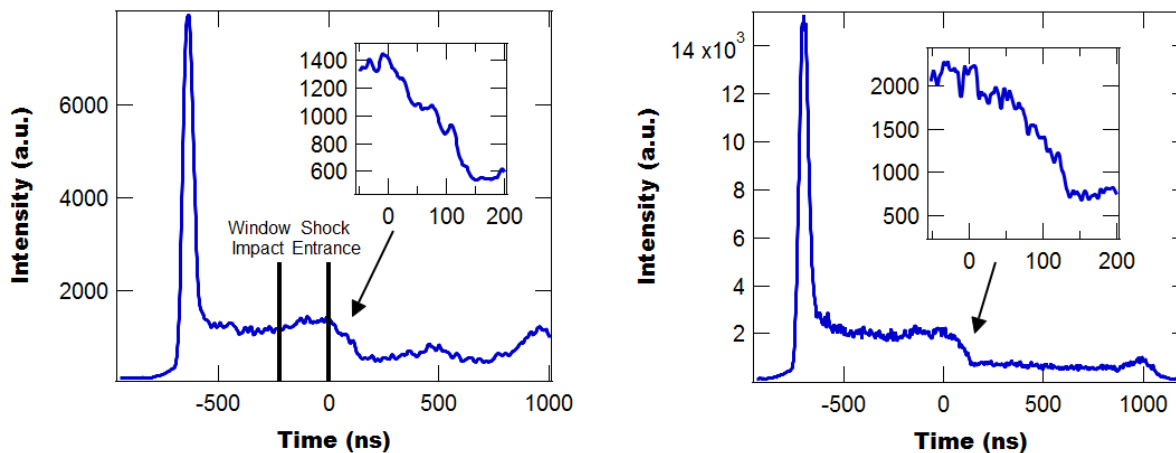


Figure 77. Average intensity of the 480 nm emission peak as a function of time during the first (a) and second (b) shock experiments. For both shots, the emission is fully quenched by 150 ns after the shock enters the CCl_4

To further examine a reason for the emission loss, a 1D wave profile simulation was carried out (by Dr. Mike Winey), using a material model for pure CCl_4 . Figure 78 shows calculated pressure histories at both the front and the rear of a sample. A comparison between the spectral data and the simulation result showed that emissions were lost when the first wave reached the rear of the sample.

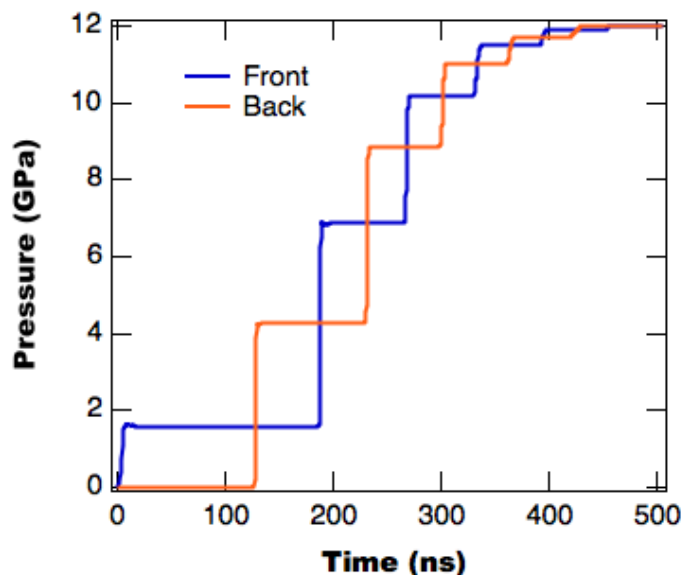


Figure 78. Calculated pressure profiles for the front and the rear of a pure CCl_4 sample.

While DAT's PL is quenched within 150 ns of being shocked, we still performed spectral analysis on the spectral streaks during the first 100 ns. In general, the streaks are rather noisy and therefore we need to perform time averaging to improve the SNR. Figure 79

shows the time averaged (over 50 ns) and normalized PL spectra at different times during each shot experiment.

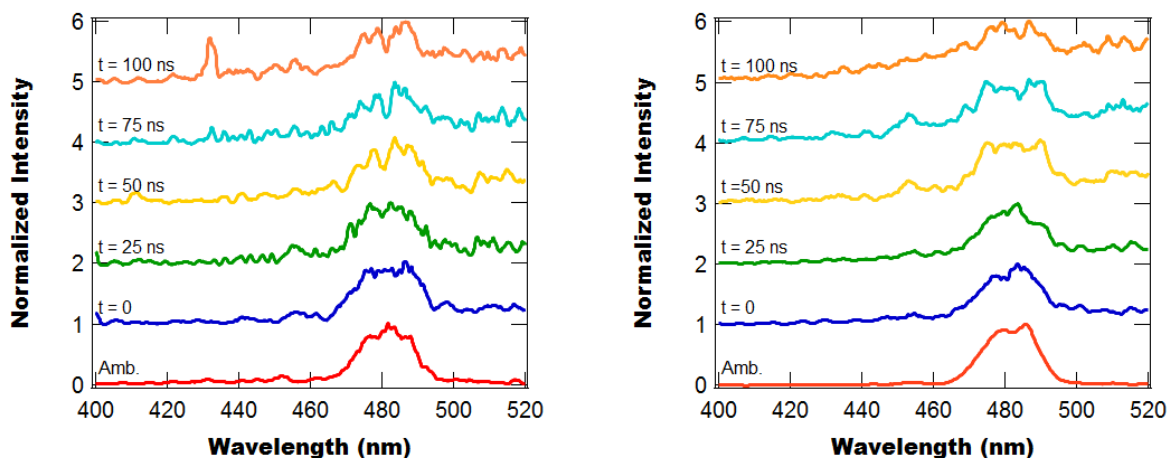


Figure 79. Time averaged (50 ns averaging) and normalized PL spectra for 355 nm excitation at different times during the first (a) and second (b) shock experiments.

From Figure 79 we find that the spectra are qualitatively consistent between shots, with the majority of differences arising due to differences in the pump energy. In both cases we see evidence of some peak splitting in the 480 nm peak after $t = 50$ ns. We also find that in both shots there is a broad background PL signal after the shock enters the CCl_4 . Initially this was hypothesized to be due to Blackbody radiation, but upon closer inspection we find that the functional form of the background does not match the blackbody curve (see Figure 80).

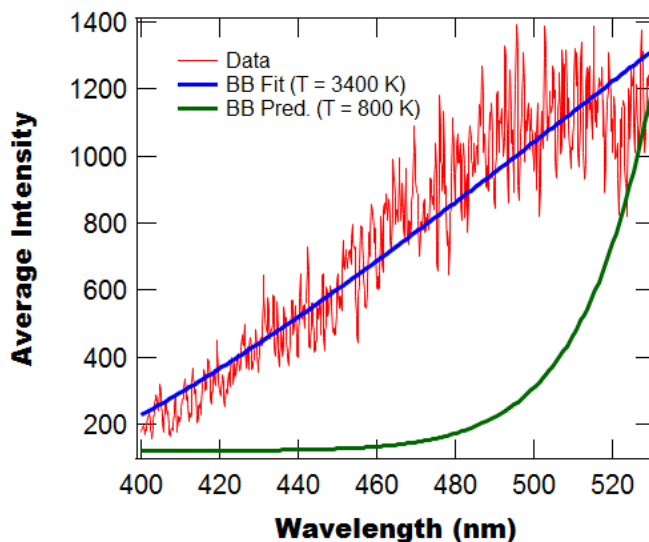


Figure 80. Temporally averaged intensity (over 800 ns to 1000 ns) as a function of wavelength, with blackbody prediction at 800 K and BB fit with T found to be 3400 K.

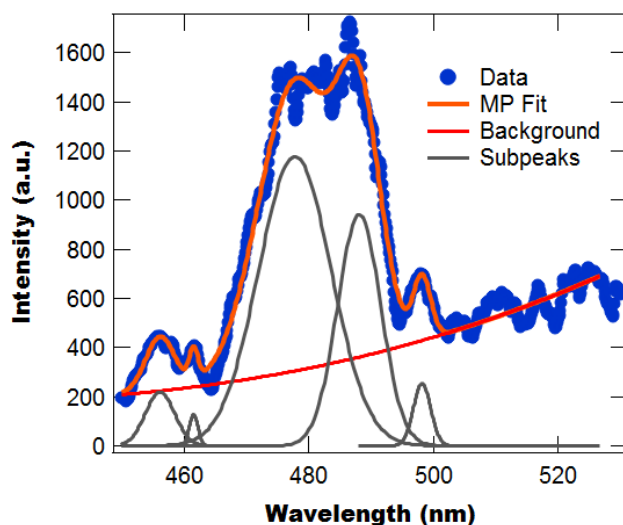


Figure 81. Example multipeak fitting for shot 1 $t = 0$ data.

While the background does not match the blackbody curve, it is found to be fit well by a cubic equation. Using this functional form and multipeak fitting we can extract DAT's emission from the spectra (see Figure 81 for example multipeak fitting). Based on the multipeak fits for the various spectra we can compute the integrated intensity of the 455 nm peak and the 480 nm peak. These integrated intensities are then used to compute the intensity ratios, which are tabulated in Table 8. However, with the PL quenching before the peak stress state is reached, and therefore not having any data to compare with independent Stokes/anti-Stokes temperature measurements (see appendix), we cannot calibrate and verify our data at this time.

Table 8. Spectral ratios calculated during first 100 ns of shock.

t (ns)	Shot 1	Shot 2
0	0.0487	0.0273
25		0.0459
50	0.0698	0.0971
75		0.1107
100	0.076243	0.1913

Developing Alternative Materials for Shock Experiments

While we intend to measure some of our current molecular dyes and molecular crystals embedded in a polymer matrix such as HTPB, based on the observation of DAT's PL quickly quenching during shock experiments we conclude that alternative materials may be required to perform thermometry under shock conditions. Most likely the cause of the quenching in DAT is the deformation of the ligands during compression leading to new non-radiative decay channels forming. The primary solution to this problem is to use more rigid structures with fewer non-radiative decay modes, which suggests the use of an

inorganic host for the Dy³⁺ ions. We therefore prepared four different inorganic materials, with two of them utilizing energy transfer to the Dy ions (Ce,Dy:Zn₂P₂O₇ and Dy:NaGdF₄) and two which use direct excitation of the Dy ions (Dy:Y₂O₃ and Dy:YAG).

Once the materials are prepared, we characterize their optical performance as well as their ability to be functionalized for suspension in CCl₄. While we could shock the materials directly, it is still desirable to use the CCl₄ host as an independent verification of temperature during shock compression. Based on our tests thus far we find that only Dy:Y₂O₃ and Dy:NaGdF₄ form stable suspensions in CCl₄.

Dy:Y₂O₃

The first inorganic material we prepared is Dy:Y₂O₃. This material is chosen as we have previous experience synthesizing it for use in an ex-situ thermal impulse sensor cocktail [25–27]. Figure 82a shows the morphology of the as-synthesized, un-annealed inorganic Dy:Y₂O₃ nanoparticles (rgAFOSR155-33). From this SEM image, the particle size can be estimated to be about < 30 nm. An accurate measurement of the size distribution will have to be done on TEM micrographs. The particles are annealed at 1273 K for 30 min and functionalized with n-octadecyltrimethoxysilane.

When dispersed in CCl₄ the annealed, functionalized particles form a stable suspension as shown in Figure 82b. The solution concentration is about 0.2% w/v. The suspension remains stable after being left to stand for 3-4 h and displays PL when excited with a UV lamp. Letting the suspension stand for longer than 4 h results in the larger size particles settling down to the bottom of the vial. The stable supernatant is decanted to give a suspension concentration that is less than 0.2% w/v. Figure 83a shows the morphology of the particles in the stable suspension. The stable suspension shows fluorescence under a 254 nm UV lamp as shown in Figure 83b. The method used to prepare this stable suspension is easily scalable.



Figure 82. (a) SEM image of un-annealed Dy:Y₂O₃ particles. (b) Photos showing particles suspension in CCl₄: observed under ambient light (left) and observed under a 254 nm UV lamp (right).

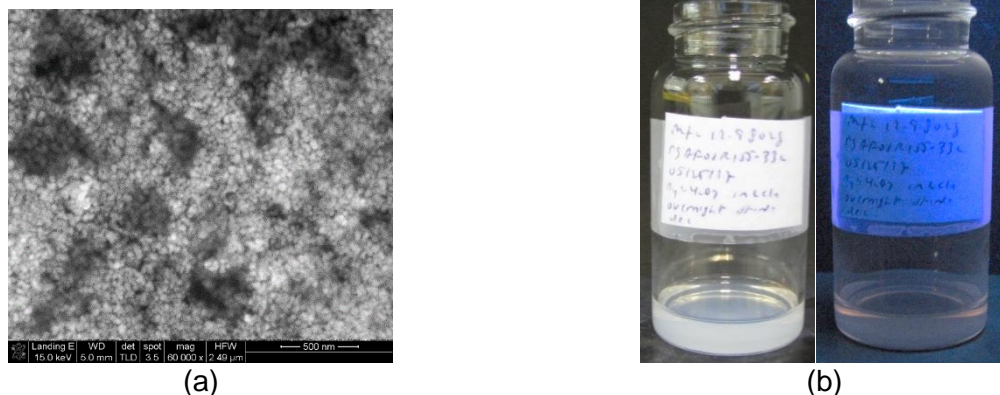


Figure 83. (a) SEM image of functionalized, annealed Dy:Y₂O₃ particles (1273 K for 30 min). (b) Photos showing overnight-stable particles suspension in CCl₄: observed under ambient light (left) and observed under a 254 nm UV lamp (right).

Dy:YAG

The next inorganic nanoparticle phosphor we considered is Dy:YAG, which is a well-known TCT phosphor [28,29]. Figure 84 demonstrates Dy:YAG's temperature dependent PL, with the maximum functional temperature reported in literature being ~ 1700 K [30], which is significantly higher than for our organic-ligand-based materials and is also found to be one of the highest maximum functional temperatures reported [29,31–33].

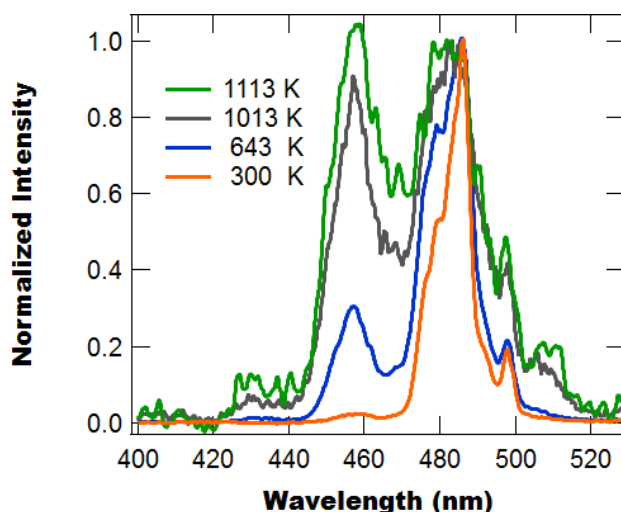


Figure 84. Normalized PL spectra as a function of temperature for a laser heated Dy:YAG bead.

Our initial Dy:YAG synthesis attempt was to use the same synthesis method as for precursor Dy:Y₂O₃, but with the Y(NO₃)₃.xH₂O substituted with either a mixture of Al(NO₃)₃.xH₂O and Al₂(SO₄)₃.xH₂O (SEM shown in Figure 85a) or just Al(NO₃)₃.xH₂O (SEM shown in Figure 85b). Both methods produce clumpy nanoparticles with sizes on the order of microns. These particles are found to be too large to form stable suspensions in CCl₄.

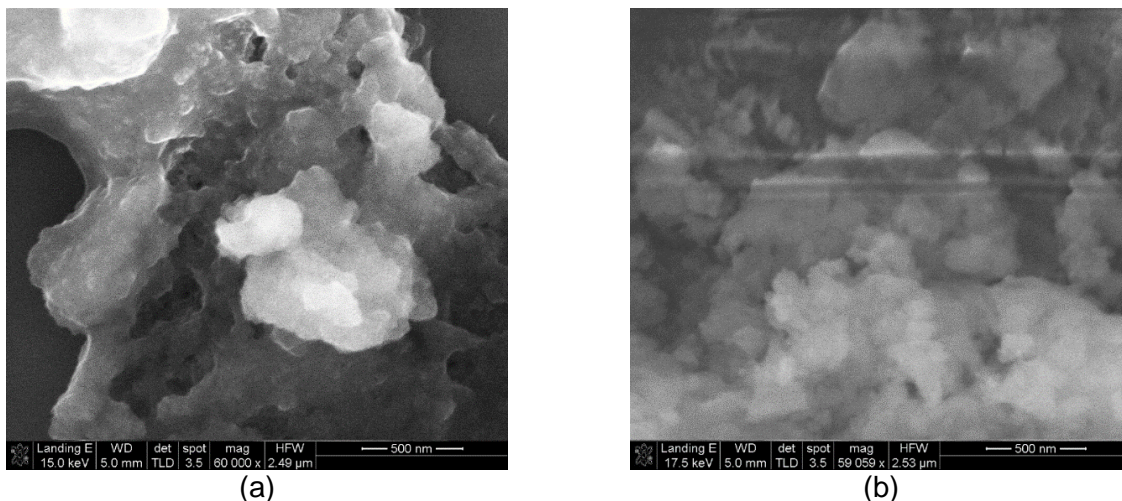


Figure 85. SEM micrographs of Dy:YAG nanoparticles prepared according to rgAFOSR159-53 and rgAFOSR162-65.

Our next attempt involved adjusting the mole ratios of $\text{Al}(\text{NO}_3)_3 \cdot x\text{H}_2\text{O}$, $\text{Al}_2(\text{SO}_4)_3 \cdot x\text{H}_2\text{O}$, and urea, which successfully resulted in spherical precursor Dy:YAG nanoparticles with diameters on the order of a few hundred nanometers (see Figure 86a). By increasing the concentration of urea, the size of these particles can be reduced to about 50 nm or less (see Figure 86b). These precursor particles form a relatively stable suspension in water.

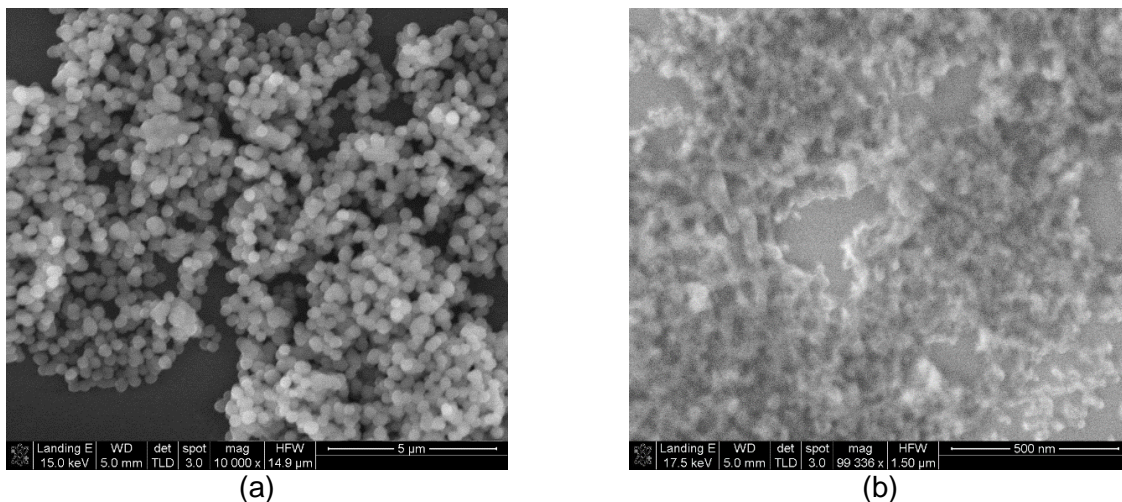


Figure 86. SEM micrographs of precursor Dy:YAG particles with different diameters: (a) in a few hundred nm range (rgAFOSR176-11) and (b) about 50 nm or less (rgAFOSR177-15).

Taking the small size p-Dy:YAG particles we next calcined them at 1373 K for 30 min. In the literature, 1373 K is found to be the minimum temperature that is required to convert the amorphous precursor to a fully YAG phase [34]. Figure 87 shows an SEM micrograph of the calcined NPs showing that the spherical particles undergo significant agglomeration during calcination. This agglomeration leads to larger particles which no longer form stable suspensions.

To address the agglomeration issue, we are going to perform calcination at a lower temperature (e.g., 1073-1273 K) and determine if the resulting particles can form a stable suspension in solvents. Note that the lower calcination temperature will result a mixture of phases (i.e., YAP, YAM, and YAG), which may or may not influence the optical properties. Additionally, we are exploring brief calcination using pyroprobe to avoid sintering that would otherwise yield micron size aggregates.

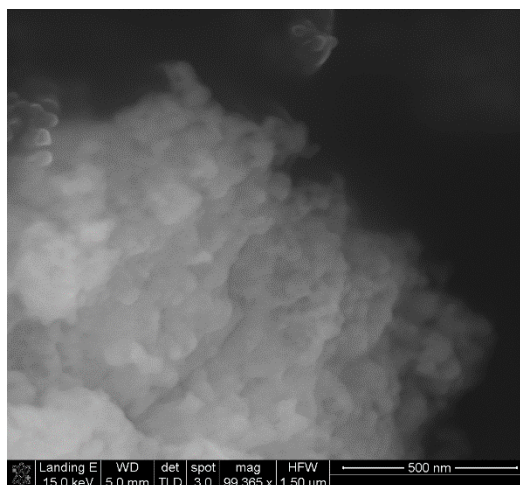


Figure 87. SEM micrograph of the calcined Dy:YAG nanoparticles (1373 K for 30 min).

While the development of suspend-able Dy:YAG nanoparticles is still ongoing, we have also developed macroscopic Dy:YAG ceramic targets for shock measurements. These targets consist of Dy:YAG powder which has been calcined at 1273 K for 1 hr, pressed into circular targets, which are subsequently sintered at 1873 K for 6 h. Figure 88 shows the Dy:YAG target samples before and after sintering. After sintering, the initially 25.4 mm (1") diameter green body laterally shrinks by about 31% to 17.5 mm (0.69") diameter.

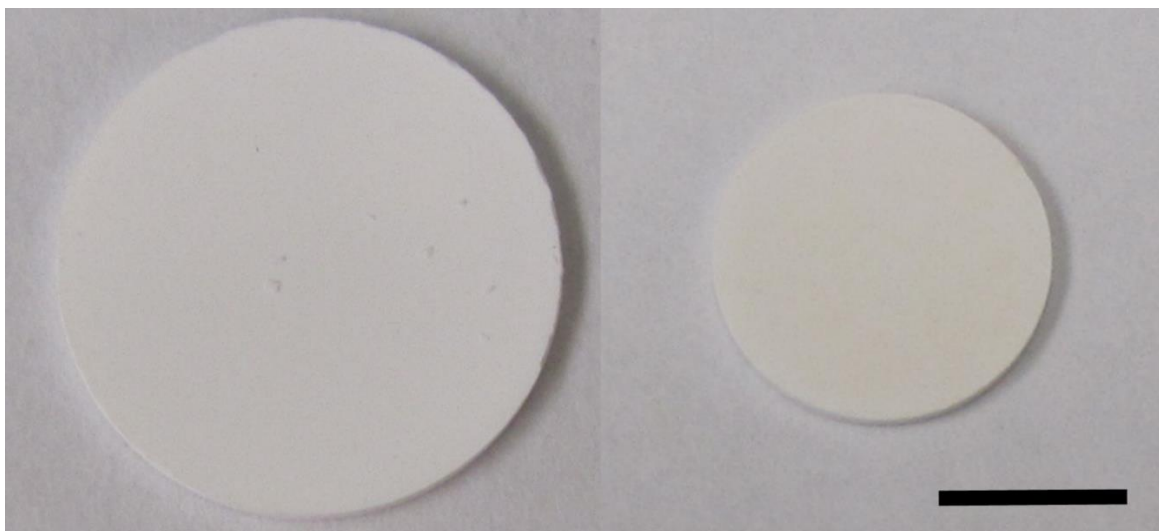


Figure 88. Dy:YAG target: (left) green body pressed using a 1273 K/1h calcined powder and (right) sintered at 1873 K for 6h. Scale bar is 1 cm.

Ce,Dy:Zn₂P₂O₇

The next material tested is Ce,Dy:Zn₂P₂O₇, which utilizes energy transfer from Ce to Dy to improve PL efficiency. This material is prepared using the method of Xu *et al.* [35], with Figure 89 showing an SEM micrograph and EDS analysis of the material. Once prepared we performed PL characterization using 355 nm excitation with Figure 90a showing our measured emission spectra and Figure 90b showing the emission/excitation spectra from the literature [35]. We also measured the material's PL decay and find it to follow a bi-exponential with a fast lifetime of $1.31 \pm 0.036 \mu\text{s}$ and a long lifetime of $10.59 \pm 0.56 \mu\text{s}$.

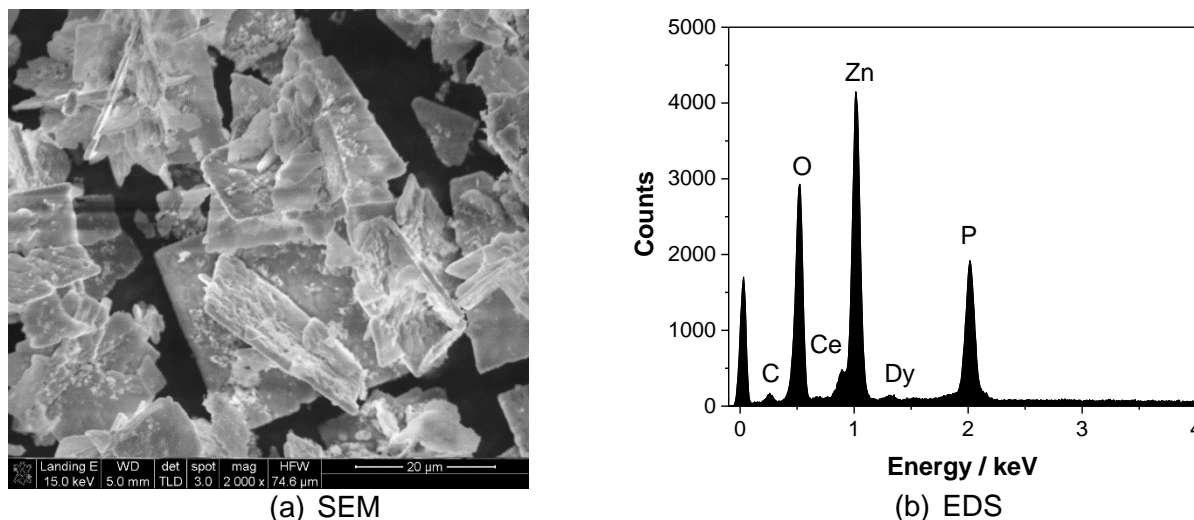


Figure 89. (a) SEM and (b) EDS of Ce,Dy:Zn₂P₂O₇.

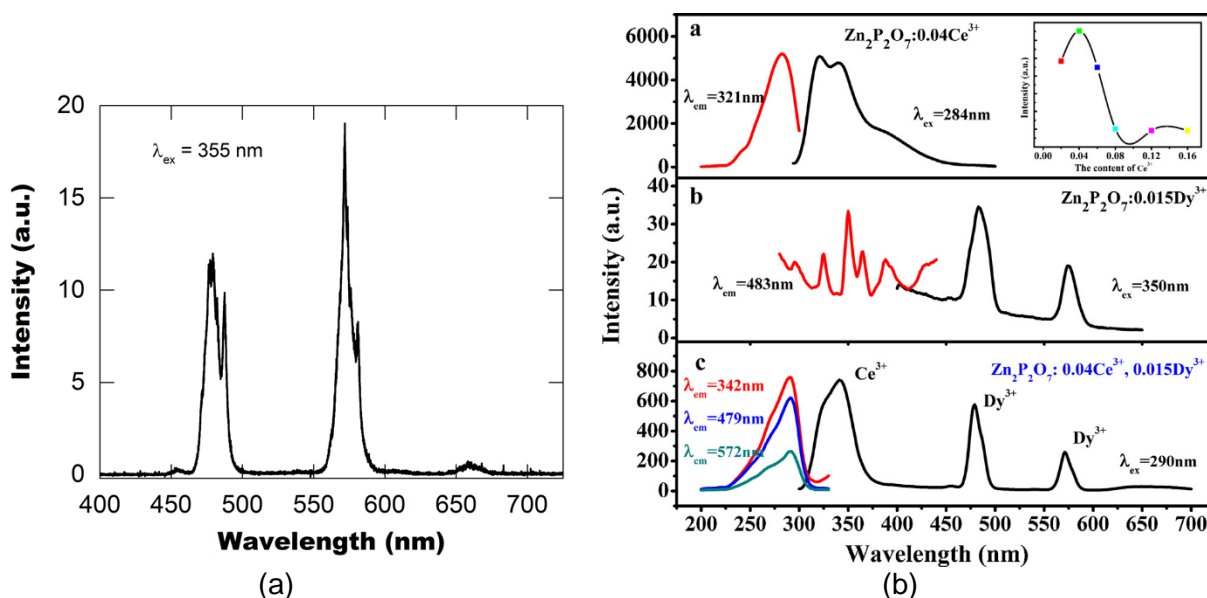


Figure 90. (a) Emission spectrum of our Dy,Ce:Zn₂P₂O₇ and (b) excitation and emission spectra from Reference [35].

From Figure 90 we observe that our spectrum is slightly different than that measured by Xu *et al.*, with our spectra displaying some Stark-splitting, but this may be simply due to differences in spectrometers and not the materials themselves. Additionally from Figure 90b we find that the ideal excitation wavelength is 290 nm, which is currently inaccessible to us. In the near future we hope to have a light source capable of exciting at this wavelength to provide more intense emission.

In addition to preparing Dy,Ce:Zn₂P₂O₇ nanoparticles, we also prepared macroscopic targets for shock experiments as shown in Figure 91. These targets were prepared by pressing the Ce,Dy:Zn₂P₂O₇ powder followed by sintering at 1223 K for 6 h. The pressed pellets are found to display green PL under 254 nm excitation.



Figure 91. Ce,Dy:Zn₂P₂O₇ target: (left) observed under ambient light. (right) observed under a 254 nm. The diameter is 2.64 mm. (b) A large batch of Ce,Dy:Zn₂P₂O₇ powder.

Dy:NaGdF₄

The final material we prepared is Dy:NaGdF₄, which utilizes energy transfer from Gd to improve PL efficiency. The material is synthesized using a solution-based method that should yield solution-stable particles that are ≤ 20 nm in diameter [36]. However, due to clumping we also observe particles > 20 nm in diameter.

Figure 92a shows the morphology of the Dy:NaGdF₄ nanocrystals prior to size separation and Figure 92b shows that prolong exposure (a few minutes) to electron beam during SEM imaging causes the particles to melt. This indicates that the particles are not very stable. From the literature, it seems that the sample should be thermally stable up to at least 553 K.

EDS measurement of the NPs confirms that the particles consist of 'Na', 'Gd', 'Dy', and 'F' elements (Figure 92c). The 'Si' peak is attributed to the substrate. The small size particles (<20 nm in diameter) that are solution-stable are obtained by centrifuging the particles dispersion in CHCl₃. It is not possible to obtain a focused image of the solution-stable particles because it is well coated with solubilizing organic ligands (oleic acid) that causes excessive charging during SEM imaging. To determine the diameter distribution and morphology of the solution stable particles, TEM imaging will be performed in the future. Figure 92d shows that the sample exhibits green PL under a 254 nm UV lamp in both the solid state and dispersed in a solution (3% v/v in CHCl₃).

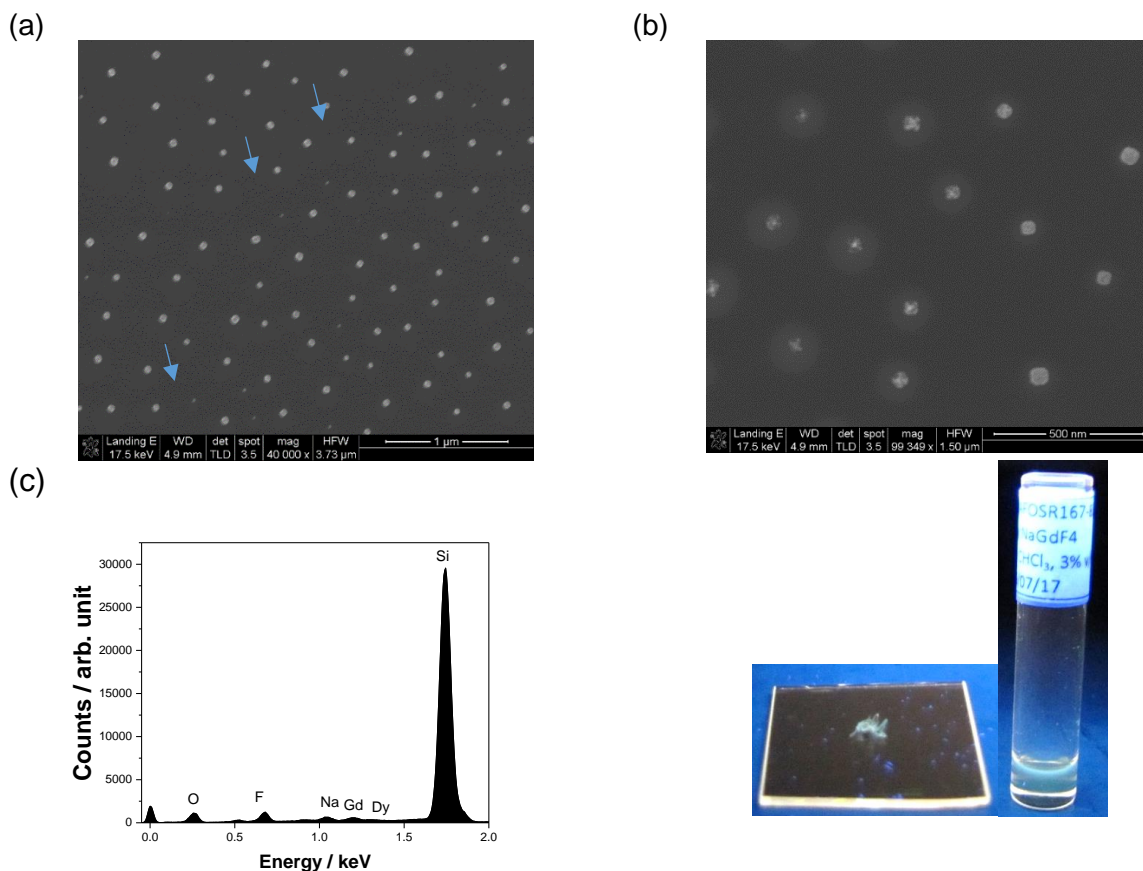


Figure 92. (a, b) SEM micrographs of Dy:NaGdF₄. Blue arrows in (a) indicate <20 nm diameter particles. (c) EDS spectrum. (d) Picture showing fluorescence under a 254 nm UV lamp. Left is in the solid state on a glass slide and right is in a 3% v/v CHCl₃.

After synthesis, we measured Dy:NaGdF₄'s PL spectrum using 355 nm excitation and find broad emission peaks from the Dy ions as shown in Figure 93. We also measured the time resolved emission and find that the PL decay follows a double exponential with lifetimes of $13.6 \pm 1.8 \mu\text{s}$ and $54.2 \pm 4.0 \mu\text{s}$. While we use 355 nm excitation, we find from literature that the peak excitation occurs using 274 nm light (see Figure 94 for excitation spectrum), which is absorbed by the Gd with subsequent energy transfer to the Dy³⁺ ions [36].

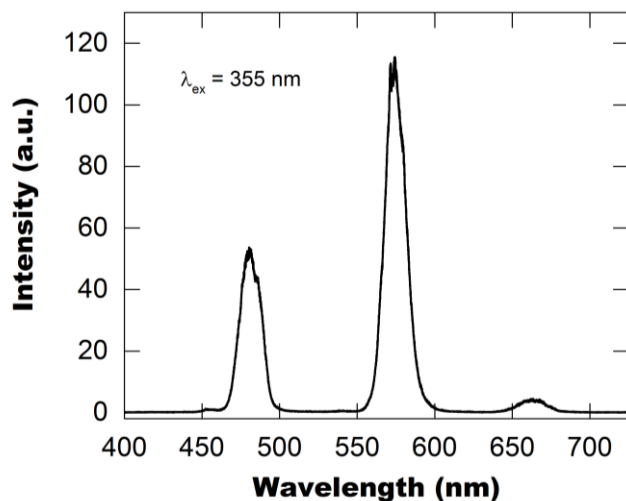


Figure 93. PL spectrum of Dy:NaGdF₄.

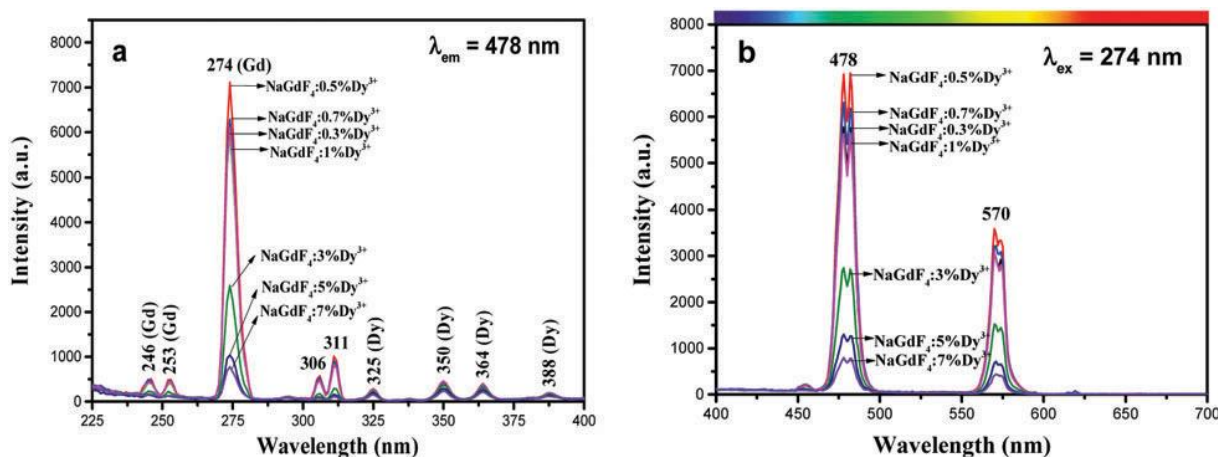


Figure 94. (a) Excitation and (b) Emission spectra of NaGdF₄. Reproduced from Reference [36].

Comparison of Materials

To compare the performance of the different inorganic materials to one another (and to DAT), we prepared identical quantities of each material and measure their PL spectra under 355 nm excitation using gated detection with a 1 μ s delay and 10 ms gate width. Figure 95a shows the resulting PL spectrum, from which we find that Dy:YAG is significantly brighter than any of the other materials for 355 nm excitation. Note that this is not an ideal comparison for Dy,Ce:Zn₂P₂O₇ and Dy:NaGdF₄ as their optimal excitation is at 290 nm and 274 nm, respectively. Future work will use OPO pumping to optimally excite these materials.

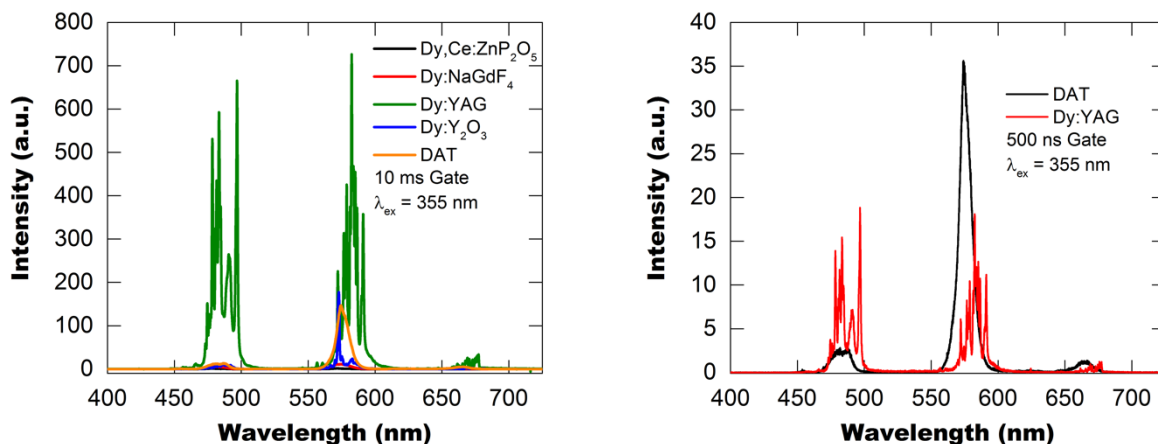


Figure 95. PL intensity for (a) different inorganic hosts (10 ms gate) and (b) smoothed single shot spectra comparing DAT and Dy:YAG.

While Dy:YAG has the brightest emission of the materials, it also has the longest lifetime, see Table 9. This long lifetime can be detrimental for single shot measurements, which have much shorter gate times. Therefore, to estimate this effect we measure both DAT and Dy:YAG using single shot measurements with a 500 ns Gate width, with the spectra shown in Figure 95b. From Figure 95b we find that the overall emission of Dy:YAG is actually dimmer than DAT, while emission in the blue is still slightly better than DAT. This implies that for single shot measurements Dy:YAG should be slightly brighter than DAT, but the improvement is nowhere near as significant as seen for the 10 ms gate width.

Table 9. Lifetimes of Dy-based inorganic materials measured using 355 nm excitation.

Material	Short LT (μ s)	Long LT (μ s)
Ce,Dy:Zn ₂ P ₂ O ₇	1.131 \pm 0.036	10.59 \pm 0.56
Dy:NaGdF ₄	13.6 \pm 1.8	54.2 \pm 4.0
Dy:YAG	n/a	1027.4 \pm 3.4
Dy:Y ₂ O ₃	101.5 \pm 3.4	338.1 \pm 8.6

These results suggest that the best material to test next in shock experiments is Dy:YAG. Therefore, we are preparing macroscopic targets for testing as well as refining the nanoparticle version such that it can form a stable suspension in CCl₄ as well as dispersing these particles in HTPB/IDPI polymer. Additionally, we are planning on further testing and development for Dy,Ce:Zn₂P₂O₇ and Dy:NaGdF₄ once an appropriate light source is obtained.

2018 Shock Experiments

In the previous year, we performed shock tests of Dy(acac)₃(TOPO)₂ (DAT) dispersed in CCl₄. We found that this sensor material only emitted PL for about 150 ns, which was significantly before the peak state was reached. We hypothesized that this failure was

due to the shock deforming the long TOPO ligands, resulting in quenching of PL. This observation motivated a turn towards more rigid structures, such as organic and inorganic crystals. Specifically, we prepared two different Dy-based temperature sensors for shock testing: Dy:YAG and DYAD and embedded them into an HTPB polyurethane host, which is a common binder for PBXs.

Shock Samples

The samples used for shock measurements are blends of either Dy:YAG or DYAD crystals dispersed in hydroxyl-terminated polybutadiene/isophorone diisocyanate/Bis(2-ethylhexyl) adipate (HTPB/IPDI/DEHA) polyurethane at a 75/25 and 50/50 crystals/polyurethane weight ratio, respectively. See Appendix A for details of the sample preparation. The HTPB/IPDI to DEHA ratio is 1/1 by weight. We use dibutyltin dilaurate DBTDL as the catalyst (1 wt%). We also add a 0.5-1.0 wt% Disparlon OX-70 defoamer (King Industries, Inc.) to minimize air bubbles. We then cure the blend between two soda-lime glass windows (3/4" diameter) overnight at ambient temperature in a 20 mm die (Figure 96). The film thicknesses range within 60-90 μm for Dy:YAG/polyurethane and 180-210 μm for the DYAD/polyurethane composites.

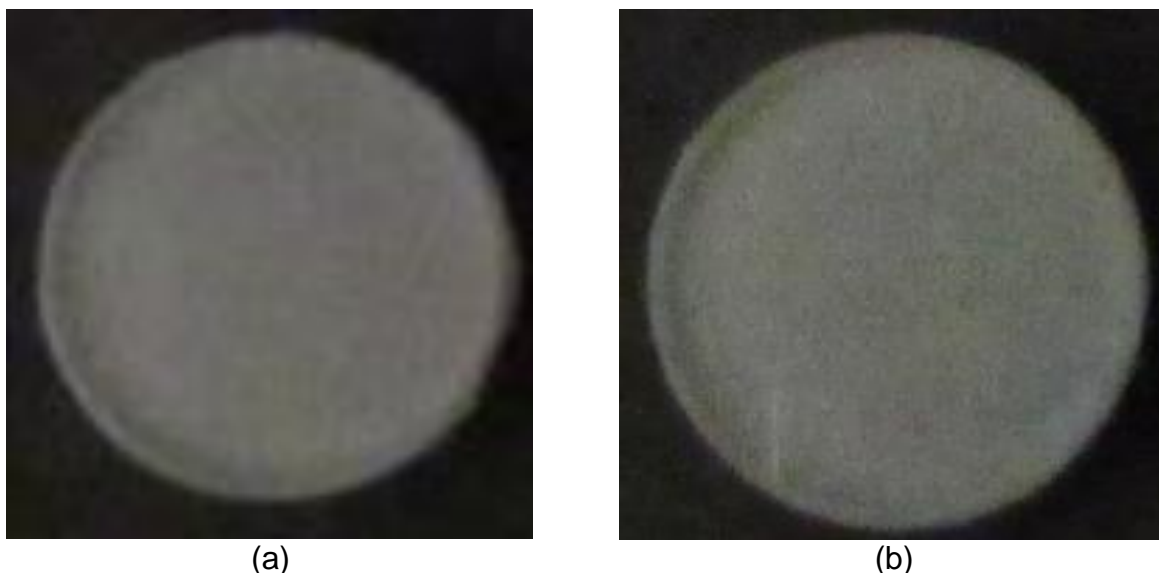


Figure 96. Pictures showing the samples used for the shock experiment: (a) Dy:YAG/polyurethane and (b) DYAD/polyurethane.

Next, we measure the densities of the sensors and composites to aid in shock experiments and modeling. The densities of the individual components, as well as the composites are tabulated in Table 10 and Table 11. We measure the densities of Dy:YAG and DYAD using a Helium Pycnometer (measured at Particle Technology Labs). For the HTPB polyurethane and the crystal/HTPB polyurethane composites, we use the Archimedes' principle (using the Ohaus AR1140 Adventurer analytical balance, along with the Density Determination kit) to determine the densities. For measurement of the densities of the composite samples, we use deionized water as the fluid medium. For the HTPB polyurethane, we use absolute ethanol because the density is less than 1.0 g/mL.

Table 10. Measured densities of the individual component.

Sample Name	Density (g/mL)
Dy:YAG	4.5513 ± 0.0027
DYAD	1.4492 ± 0.0004
HTPB/IPDI/DEHA polyurethane	0.9248 ± 0.0004

The measured densities of the composites are on par with the estimated rule of mixture densities that are based on the individual components, which uses the following equation:

$$\rho_{AB} = \rho_A V_A + \rho_B V_B \quad (4)$$

where, ρ is density, V is volume fraction, A and B are the respective components, and AB is the composite blend [20].

Table 11. Measured and calculated densities of the crystal/polyurethane composites.

Sample Name	Composition		Density(g/mL)	
	w/w	v/v	Measured	Calculated
Dy:YAG/polyurethane	75/25	38/62	2.2204 ± 0.0116	2.2982
DYAD/polyurethane	50/50	39/61	1.1097 ± 0.0032	1.1291

Shock Test

For shock measurements we use a 2.5" gas gun with an impactor velocity of 0.413 km/s, with Figure 97 displaying a schematic diagram of the shock test geometry. This geometry is designed to achieve a peak stress of 3 GPa.

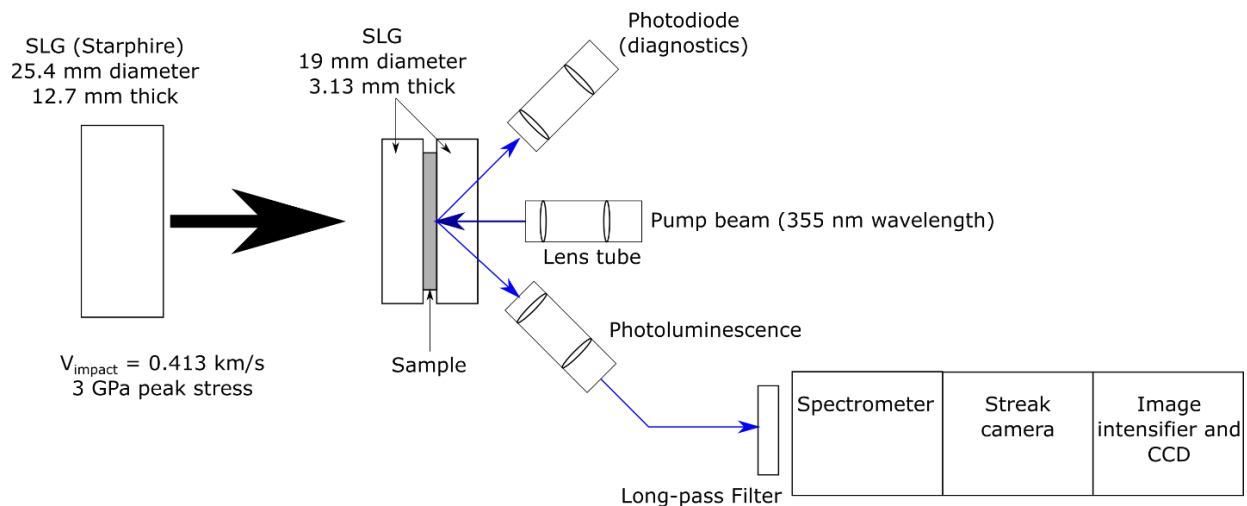


Figure 97. Diagram of shock experiment setup.

During our shock tests we excited the temperature sensors with 355 nm light from a fiber-coupled frequency-tripled Nd:YAG laser. This excitation pulse arrives at the sample shortly before impact such that the temperature sensors will be actively emitting PL as the shockwave enters the sample. The resulting PL is collected by a fiber-coupled lens tube which collects the PL emission into a spectral streak camera.

Dy:YAG Shock Results

The first sample we test under shock compression is Dy:YAG dispersed in HTPB. Based on our work with a variety of Dy-doped materials we determined that YAG is one of the best hosts for PL from Dy. We therefore anticipated that it should give us the best results possible.

Figure 98 shows the spectral streak of Dy:YAG's PL during shock. Impact occurs at $t = 0$, with the shock entering the sample 538 ns later. From Figure 98 we find that the Dy:YAG/HTPB sample continues to emit light until approximately 2 μs , which occurs after the expected arrival of the edge wave at $\approx 1.7 \mu\text{s}$. Additionally, we find that when the shock enters the sample there is a broad emission peak of unknown origin. However, it is short lived and has a minimal impact on our analysis.

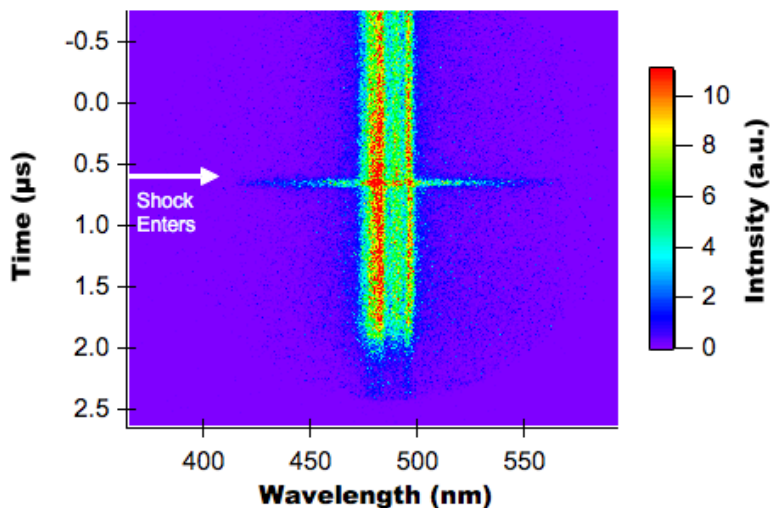


Figure 98. Spectral streak for shocked Dy:YAG dispersed in HTPB.

Using the spectral streak in Figure 98, we extract spectra at different times with 50 ns averaging to improve the signal-to-noise, with the resulting spectra (scaled to the peak at 496 nm) shown in Figure 99a. From Figure 99a we observe that there is very little change in spectra as time progresses.

In addition to considering the spectra at different times after impact, we also compute the total emission intensity and the integrated intensity ratio between band 1 (420 – 470 nm) and band 2 (470 – 520 nm), which are shown in Figure 99b. From Figure 99b we find that the integrated intensity remains relatively flat (minus the anomalous peak after the shock enters the sample) until after the edge wave is expected to arrive. This means that

there is little to no quenching of Dy:YAG's PL due to shock compression in this experiment. Additionally, we find from Figure 99b that the ratio between band 1 and 2 only increases slightly after the shockwave enters the sample (not including the anomalous peak). This small increase implies that the temperature increase within the sample is minimal, as the ratio increases with temperature. This result is expected given the design of the shock experiment and the nature of the sample. Work is underway to quantify this temperature increase.

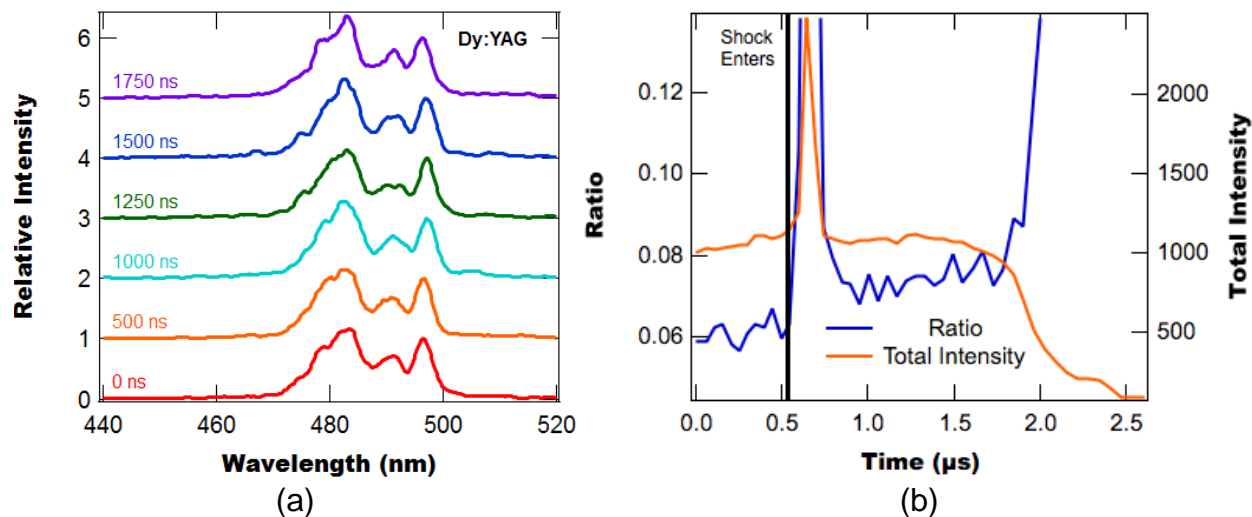


Figure 99. (a) PL spectra from Dy:YAG at different times during shock compression averaged over 50 ns. (b) Integrated intensity ratio and total intensity as a function of time during shock compression.

DYAD Shock Results

Having completed shock compression tests of our best Dy-based phosphor (Dy:YAG), we next performed a shock test on our best organic Dy-based phosphor (DYAD). This test was identical to the Dy:YAG shot, albeit with a slightly different sample size and loading concentration. Figure 100 shows the DYAD PL spectral streak during the shock test.

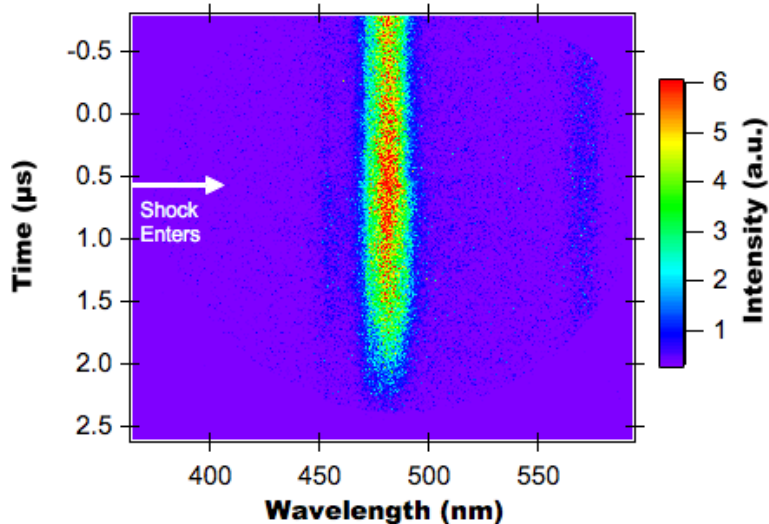


Figure 100. Spectral streak for shocked DYAD dispersed in HTPB.

From Figure 100 we find that DYAD maintains its PL emission after the shockwave enters the sample and until after the expected arrival of the edge wave. This confirms the sensor’s usefulness for shock testing to at least 3 GPa. Next, we compute the 50 ns averaged spectra, the total integrated intensity, and the integrated intensity ratio, which are shown in Figure 101.

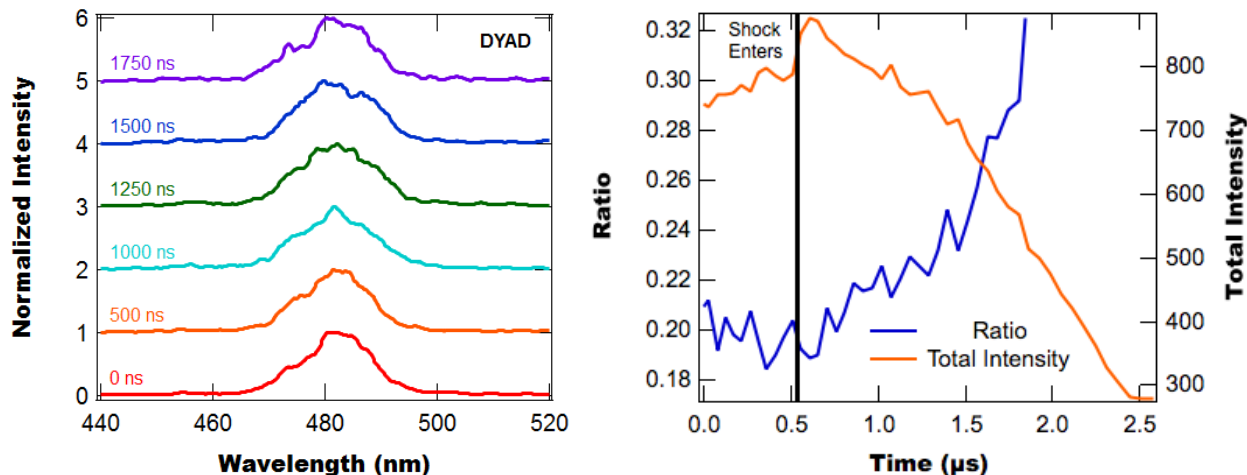


Figure 101. (a) PL spectra from DYAD at different times during shock compression averaged over 50 ns. (b) Integrated intensity ratio and total intensity as a function of time during shock compression.

Comparing the spectra in Figure 101a, we find that there isn’t an obvious difference as time increases. However, when considering the ratio in Figure 101b we find that the ratio does indeed change as time progresses after the shock enters the sample. While this increase is likely due to an increase in temperature, further work is required to quantify this temperature and determine other possible factors that could be contributing to a change in the ratio.

2019 Shock Experiments

After the successful tests of the Dy:Y(acac)₃(DPEPO) phosphor for 6 GPa loading in 2018, we next performed (in 2019) shock tests using different peak stresses (3 GPa, 6 GPa, and 9 GPa) to determine how the peak stress affects the sensors PL. Additionally, we tested the DAT dye dissolved in HTPB to see if it displays the same pressure quenching when doped in a polymer host as was displayed when dissolved in CCL₄.

Shock Samples

The samples used for shock measurements were blends of either DYAD or DAT molecular crystals dispersed in hydroxyl-terminated polybutadiene/isophorone diisocyanate/Bis(2-ethylhexyl) adipate (HTPB/IPDI/DEHA) polyurethane elastomer at a 50/50 and 30/70 crystals/polyurethane weight ratio, respectively. Polyurethane binder formulations were prepared by the addition 1% (w/w) Di-n-butyltin dilaurate (DBTL) catalyst to 10% (w/w) IPDI in HTPB solution. DEHA was then added in a 1:1 ratio to HTPB/IPDI/DBTL and stirred for several minutes. Hydroxy terminated polybutadiene prepolymer (HTPB, R-45M, Mn= 2800, hydroxyl value =0.72 meq/g) was purchase from CRS Chemicals. Isophorone diisocyanate (IPDI, L13759) curing agent, di-(2-ethylhexyl) adipate (DEHA, L10195) plasticizer, and Di-n-butyltin dilaurate (DBTL, 71130) catalyst were all purchased from Alfa Aesar. The blend of molecular crystals in polyurethane elastomer is cured between a front buffer disc and rear window disc (each 3/4" diameter) overnight at ambient temperature in a 20 mm die. Table 12 lists sample details for each shock experiment. Figure 102 shows a DYAD-elastomer shock sample and Figure 103 shows a DAT shock sample. The synthesis of the DYAD and DAT molecular crystals is described in the following sections.

Table 12. Shock Sample Details

Shot	Stress	Impact Velocity	Impactor	Front buffer	Rear window	Sample details	Thickness
(1) DYAD	3 GPa	0.41 km/s	SLG	SLG (19 mm x 3 mm)	SLG (19 mm x 3 mm)	ngAFOSR-2-27-10 50 wt % DYAD Elastomer	ISP: 177 um
(2) DYAD	6 GPa	0.71 km/s	Al	Al (19 mm x 2 mm)	z-cut quartz (19 mm x 9.5 mm)	ngAFOSR-2-45-13 50 wt % DYAD Elastomer	91 um
(3) DYAD	9 GPa	0.43 km/s	Cu	Cu (19 mm x 2 mm)	Sapphire (19 mm x 9.5 mm)	ngAFOSR-2-45-15 50 wt % DYAD Elastomer	70 um
(4) DAT	6 GPa	0.71 km/s	Al	Al (19 mm x 2 mm)	z-cut quartz (19 mm x 9.5 mm)	ngAFOSR-3-31-7 30 wt% DAT Elastomer	200 um

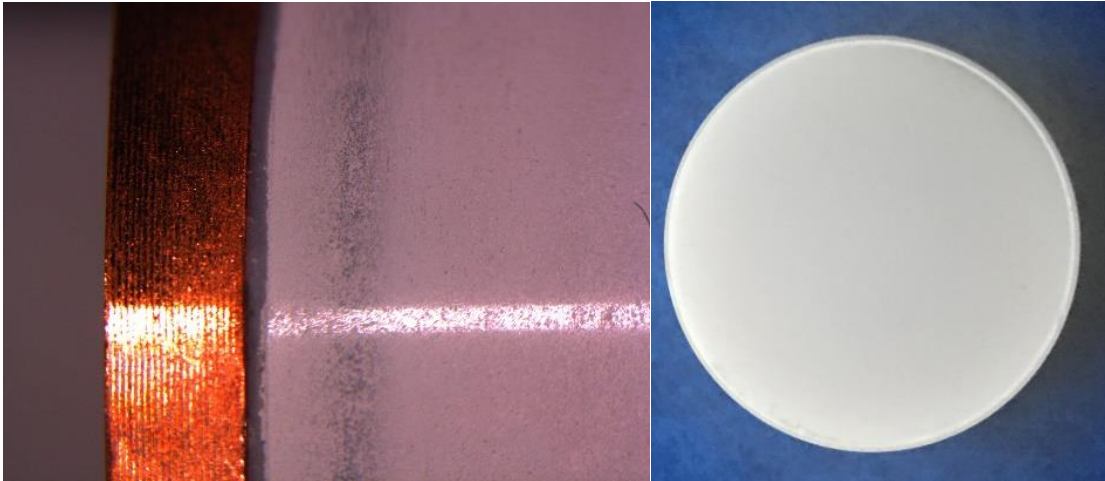


Figure 102. Side and top view of 50% DYAD/Polyurethane between a front buffer window (Cu) and a sapphire rear window.

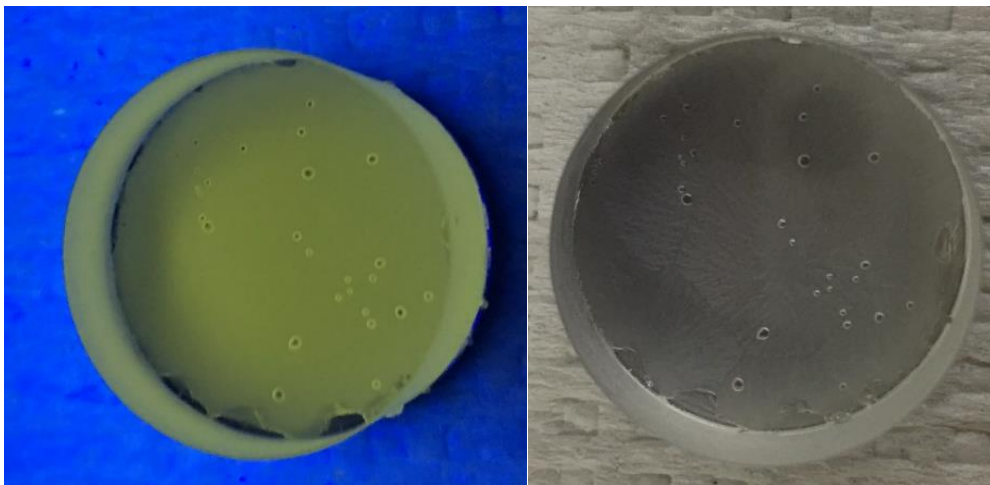


Figure 103. Top view view of DYAD/Polyurethane between a front buffer window (Cu) and a sapphire rear window.

Shock Tests Setup

For shock measurements we use a 2.5" gas gun with an impactor velocity of 0.413 km/s, with Figure 104 displaying a schematic diagram of the shock test geometry. This geometry is designed to achieve peak stresses up to 9 GPa.

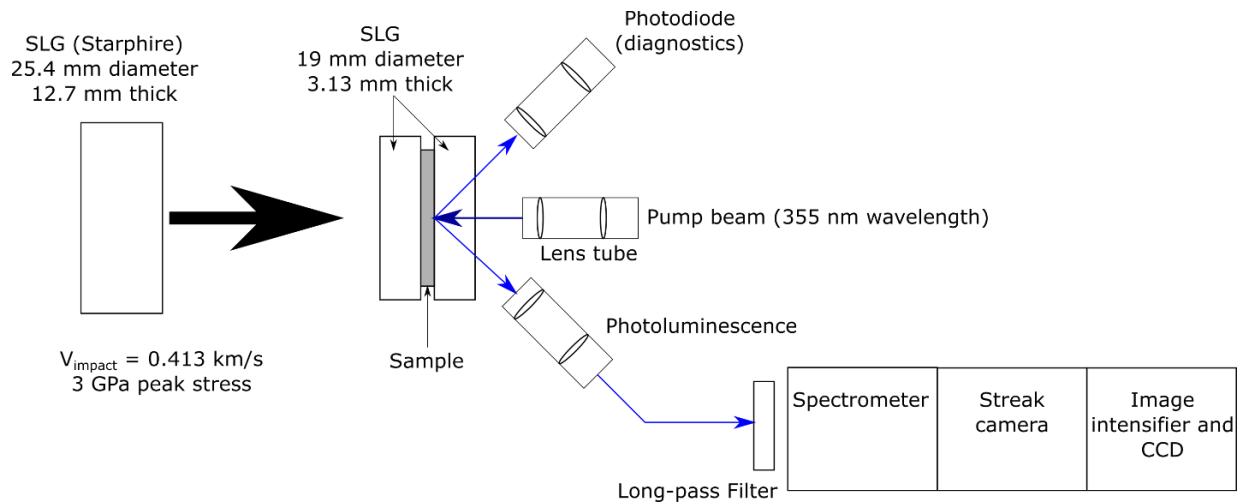


Figure 104. Diagram of shock experiment setup.

During our shock tests we excited the temperature sensors with 355 nm light from a fiber-coupled frequency-tripled Nd:YAG laser. This excitation pulse arrives at the sample shortly before impact such that the temperature sensors will be actively emitting PL as the shockwave enters the sample. The resulting PL is collected by a fiber-coupled lens tube which collects the PL emission into a spectral streak camera.

Table 13. Shock test details.

Shot	Stress	Impact velocity	Impactor	Front buffer	Rear window
(1)DYAD	3 GPa	0.41 km/s	SLG	SLG (19 mm x 3 mm)	SLG (19 mm x 3 mm)
(2)DYAD	6 GPa	0.71 km/s	Al	Al (19 mm x 2 mm)	z-cut quartz (19 mm x 9.5 mm)
(3)DYAD	9 GPa	0.43 km/s	Cu	Cu (19 mm x 2 mm)	Sapphire (19 mm x 9.5 mm)
(4)DAT	6 GPa	0.71 km/s	Al	Al (19 mm x 2 mm)	z-cut quartz (19 mm x 9.5 mm)

Test Results

The first three shots performed in 2019 used DYAD/HTPB samples with three different peak pressures (3 GPa, 6 GPa, and 9 GPa). Figure 105 shows streak camera traces from the three shots. Note that the time scale is set such that when the shock enters the sample $t = 0$. From Figure 105 we find that the samples display PL for some time after the shock wave enters the sample, with the time to quenching decreasing with increasing peak pressure.

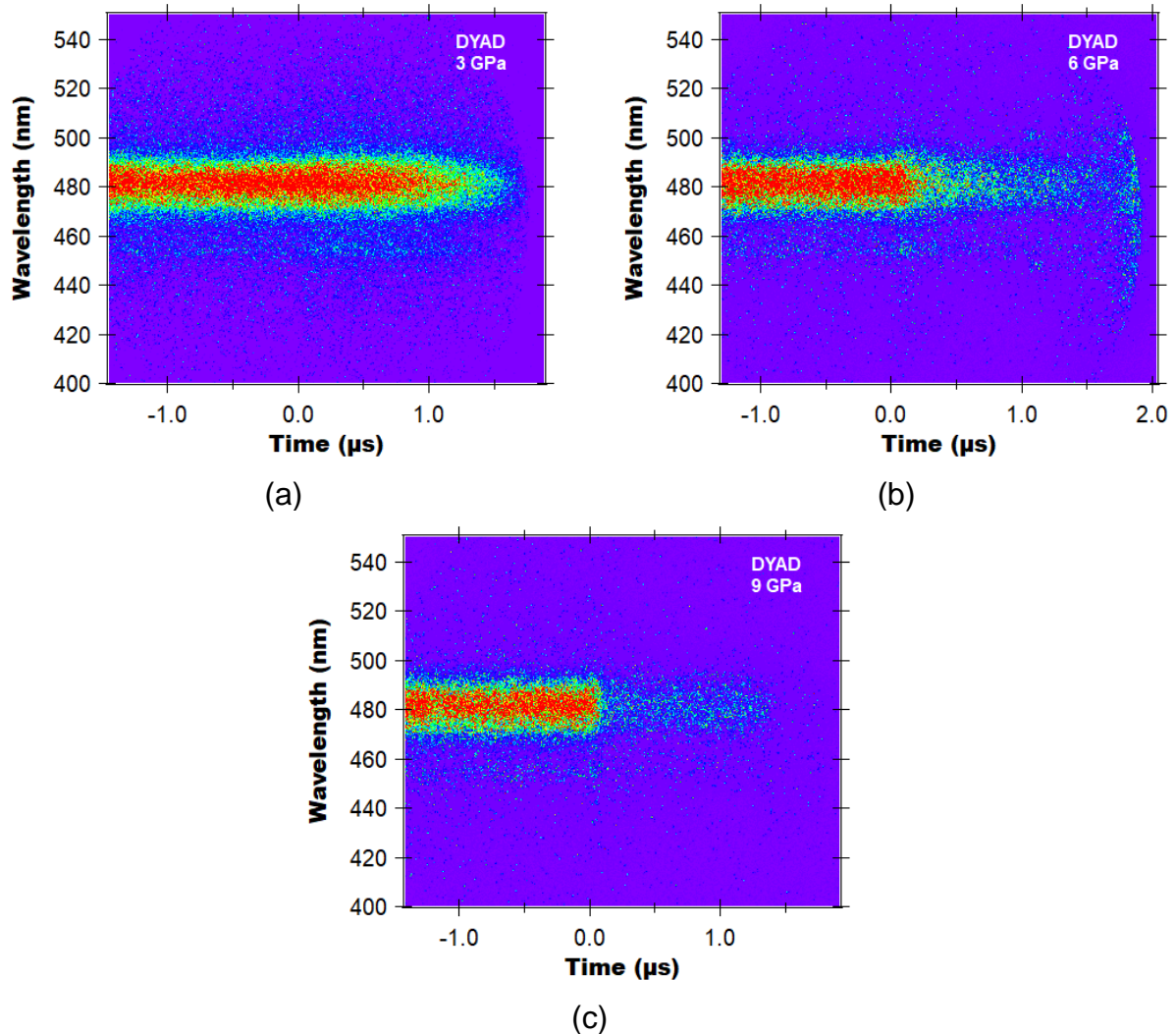


Figure 105. Streak camera traces for DYAD shots with peak pressures of 3 GPa (a), 6 GPa (b), and 9 GPa (c).

Using the streak camera traces we calculate the integrated intensity (421 nm – 520 nm) and integrated intensity ratio: $I(421 \text{ nm} \rightarrow 461 \text{ nm})/I(461 \text{ nm} \rightarrow 521 \text{ nm})$ as a function of time using 64 ns time binning, with the resulting traces shown in Figure 106. Figure 106 confirms that as the peak pressure increases the intensity quenches more quickly. Note that this quenching is not complete as we still detect PL signal out to 1.3 μs even at 9 GPa.

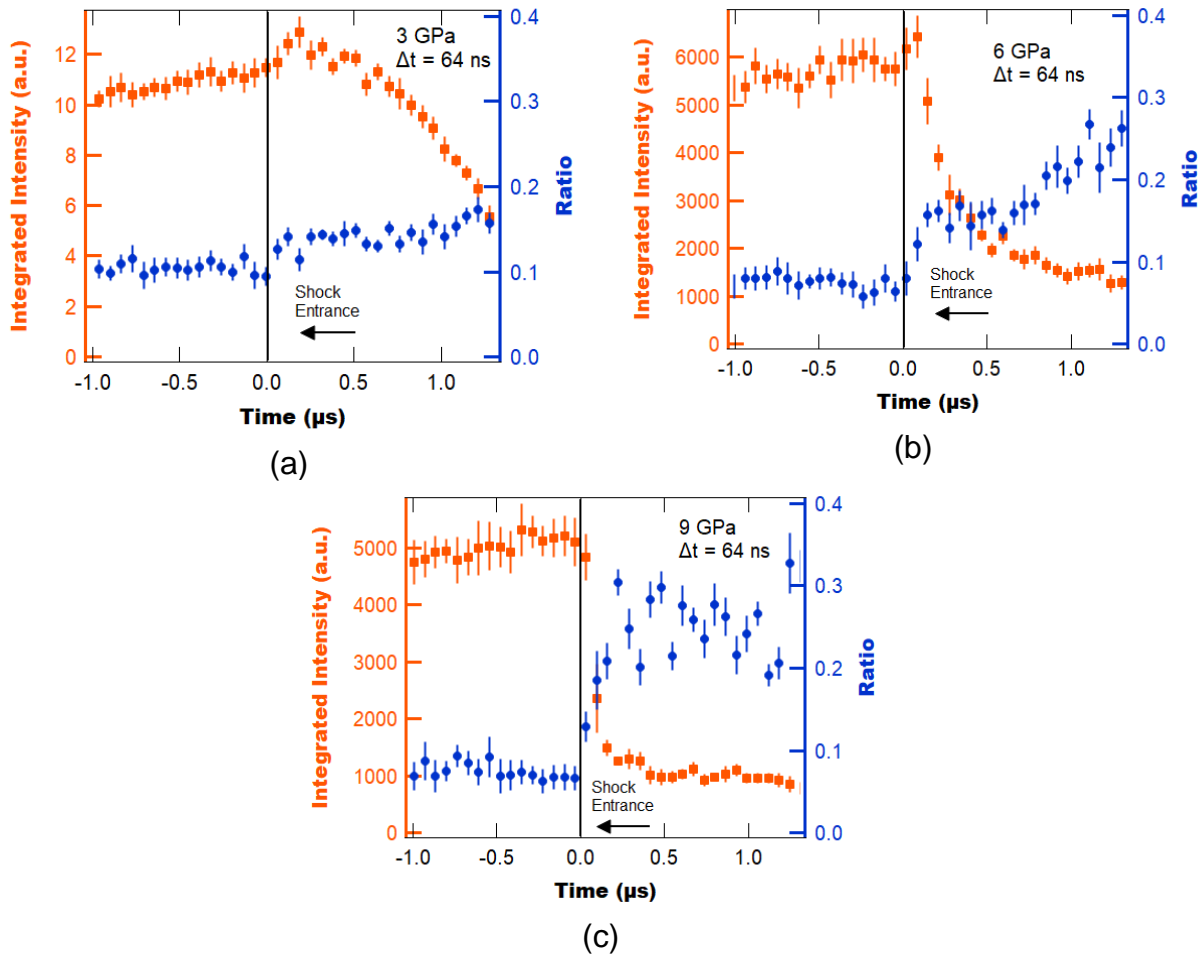


Figure 106. Integrated intensity and ratio as a function of time during shock experiments for peak pressures of 3 GPa (a), 6 GPa (b), and 9 GPa (c). Edge wave arrival times are 1.68 μs , 1.45 μs , and 1.21 μs for 3 GPa, 6 GPa, and 9 GPa, respectively.

Having computed the integrated intensity and intensity ratio for each peak pressure, we next plot these curves together to compare the influence of peak pressure as shown in Figure 107a and Figure 107b. From Figure 107b we find that upon the shock entering the sample there is a sharp jump in the intensity ratio, with the magnitude of that jump increasing with peak pressure. Interestingly, after the initial jump the ratio for 3 GPa and 6 GPa remains constant for around 700 ns before starting to increase again, while for 9 GPa the ratio appears to stay constant (within uncertainty).

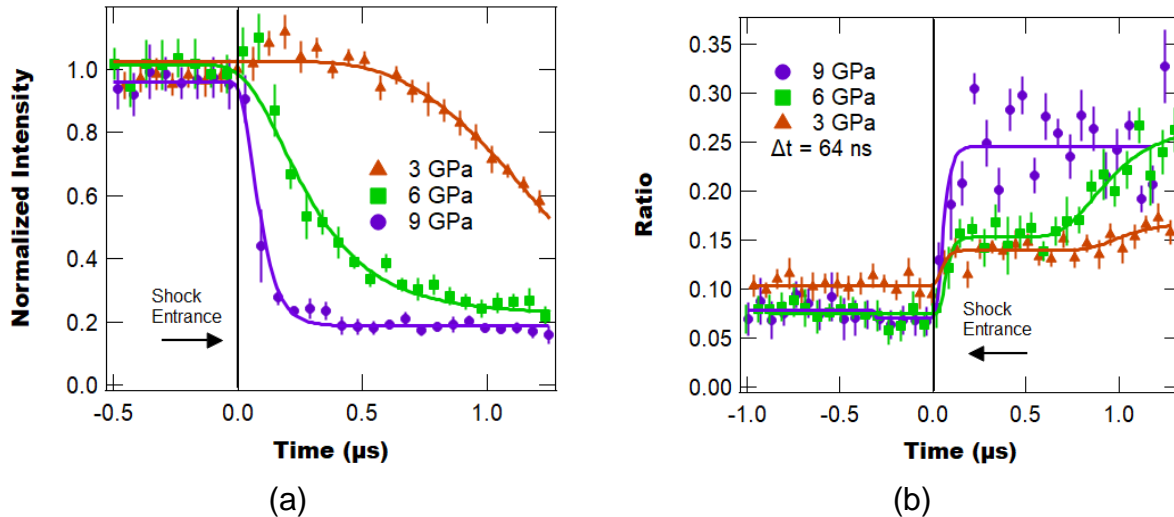


Figure 107. Normalized intensity (a) and ratio (b) as a function of time for different peak pressures. Edge wave arrival times are $1.68 \mu\text{s}$, $1.45 \mu\text{s}$, and $1.21 \mu\text{s}$ for 3 GPa, 6 GPa, and 9 GPa, respectively.

After completing our shock measurements of DYAD/HTPB samples we next performed a shot using DAT/HTPB with a peak pressure of 3 GPa, with Figure 108 showing the resulting streak camera trace. From Figure 108 we find some odd behavior in the spectral trace, with there being a short lived broad emission immediately after the shock enters the sample and a bright broad emission starting about $1.3 \mu\text{s}$ after the shock enters.

Given the odd emission we next plot spectral traces at different times using 64 ns time-binning as shown in Figure 109a. From Figure 109a we find that there is a broad background emission for all times as well as emission from the DAT. This additional background makes ratio analysis of the spectra difficult as it is hard to remove the background without knowing the underlying cause. However, we still calculate the integrated intensity and ratio as a function of time (with background included) in Figure 109b.

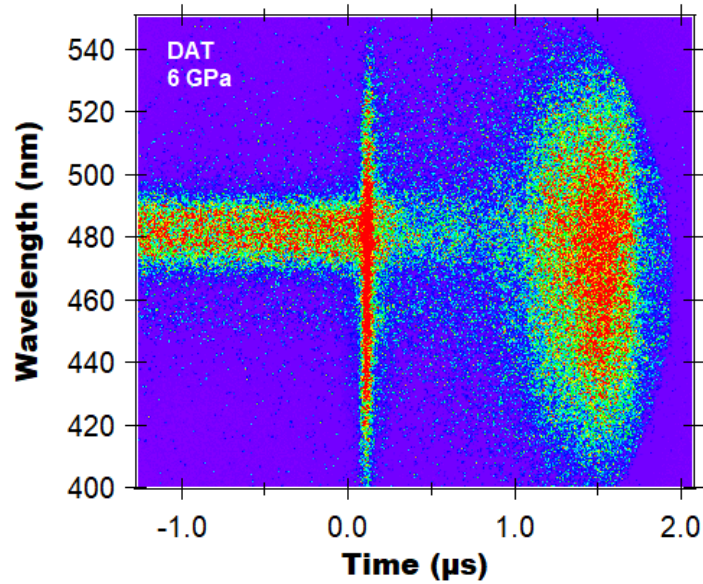


Figure 108. Streak camera trace for 6 GPa DAT shot.

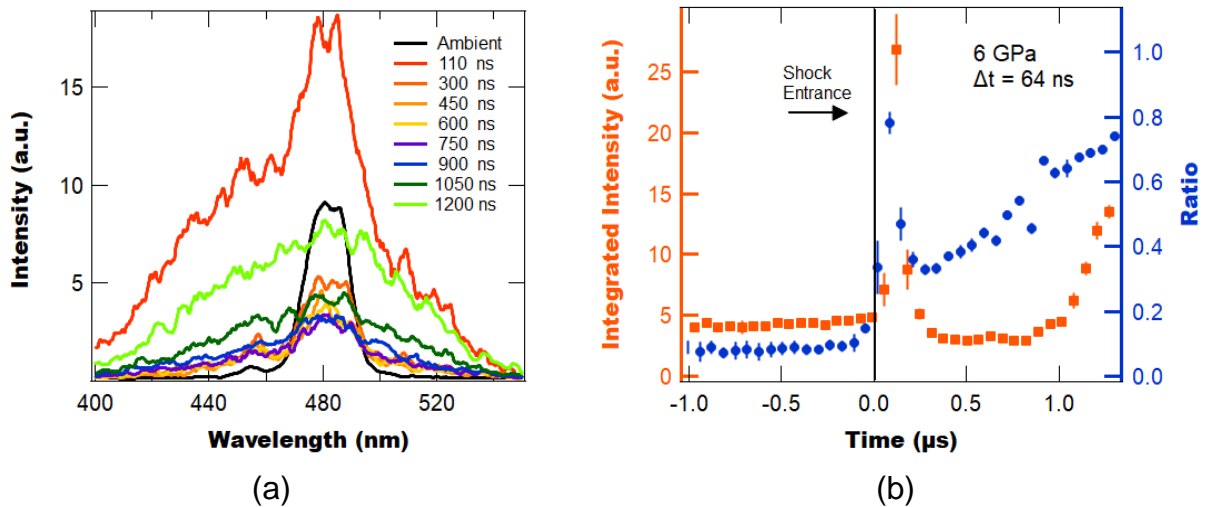


Figure 109. (a) Spectra of DAT measured at different times after the shockwave enters the sample a (averaged over 150 ns) and (b) the integrated intensity and intensity ratio as a function of time during the shock experiment with each data point averaged over 64 ns.

J. Project Publications and Presentations

1. B.R. Anderson, R. Gunawidjaja, and H. Eilers, "Two-color Thermometric Imaging of Heterogeneous Materials During Pulsed Laser Heating," *Submitted to X*.
2. B.R. Anderson, R. Gunawidjaja, and H. Eilers, "Soluble Sm-based Ternary Complexes for Non-Contact Molecular Thermometry" *J. Lumin.* 204, 341-348 (2018).
3. B.R. Anderson, R. Gunawidjaja, and H. Eilers, "Two-color thermosensors based on $[Y_{1-x}Dy_x(\text{acetylacetonate})_3(1,10\text{-phenanthroline})]$ molecular crystals," *Applied Physics B* 123, 62 (2017)
4. B.R. Anderson, R. Gunawidjaja, and H. Eilers, "Dy³⁺-doped Yttrium Complex Molecular Crystals for Two-color Thermometry in Heterogeneous Materials," *Journal of Luminescence* 188, 238-245 (2017)
5. Hergen Eilers, Benjamin R. Anderson, Ray Gunawidjaja "Temperature Sensors for the Real-Time investigation of Hot-Spots in Shocked Heterogeneous Materials," IMECE, Phoenix AZ (2016)
6. Hergen Eilers, Ray Gunawidjaja, Benjamin R. Anderson, "Luminescent Dy(III) and Sm(III) Molecular Complexes as In-Situ Temperature Sensors in Heterogeneous Materials under Shock Loading," 2016 MRS Fall Meeting, Boston MA, MB2.10.04 (2016)

VI. SUMMARY

In this project we developed Dy- and Sm-based phosphors for temperature sensing in heterogenous materials under shock loading. These sensors were split into two categories: molecular crystals and dyes, with the molecular crystals designed to be analogous to HE crystals found in PBXs and the dyes designed to be dissolvable in HTPB polymer. Based on slow heating experiments we determined that the best molecular crystal phosphor is Dy:Y(acac)₃(DPEPO), while the best dye was determined to be Sm(acac)₃(TOPO). After identifying the best phosphors for further testing we next proceeded with two different sets of experiments in parallel, the first being thermometric imaging of pulsed laser heating and the second set being shock impact experiments using gas guns.

Thermometric imaging was first demonstrated at ASL using standard machine vision cameras, but their timing accuracy was found to be too inaccurate to obtain good results. Therefore in order to obtain better timing we designed and built a thermometric imaging system consisting of a custom Splitcam device and two PI-Max 4 ICCDs. This setup allowed us to image temperature profile development of pulsed laser heating of heterogenous samples consisting of either Dy:YAG or Dy:Y(acac)₃(DPEPO) dispersed in HTPB.

While thermometric imaging experiments were occurring at ASL a second set of experiments (shock compression using a gas gun) were being carried out at ISP. These experiments consisted of shock compression of different samples whose PL spectra were captured as a function of time using a fiber and a streak camera attached to a monochromator. These experiments began by using a sample consisting of Dy(acac)₃(TOPO) dissolved in CCl₄, which has a known equation of state with the idea being to correlate the spectrally obtained temperature to the temperature predicted by the equation of state. Unfortunately, Dy(acac)₃(TOPO) was found to display strong pressure quenching and we were unable to obtain any conclusive results.

Therefore the next set of shock compression experiments were designed to use Dy-doped phosphors dispersed in HTPB (namely Dy:YAG, Dy:Y(acac)₃(DPEPO), and Dy(acac)₃(TOPO)) with the hope that these solid samples would be less prone to pressure quenching. These solid samples were found to emit adequate PL for pressures up to 9 GPa. After measuring the spectral streaks of each shock test we analyzed them to determine the spectral ratio and total intensity as a function of time. We found that during shock testing all samples display some pressure quenching, with the time until full quenching decreasing with increasing pressure. Additionally, we find that the spectral ratio increases as a function of time after impact, which is consistent with increasing temperature. However, it is difficult to determine if this effect is solely due to temperature or is also influenced by pressure as well. This question is one of the fundamental challenges to our thermometry technique that hasn't been fully resolved yet.

This project provides significant support for the use of two-color thermometric imaging in shock compression measurements as a method to possibly image temperature. These

results demonstrate that we can determine changes in the phosphors spectral ratio as a function of time during shock compression. However, there is still a fundamental question to overcome in interpreting the results and that is: how do fast pressure changes affect the spectral ratio? The answer to this question is needed to adequately separate out different effects on the spectral ratio in order to state with confidence that the phosphors are measuring temperature.

VII. APPENDECIES

A. CCl₄ Raman Measurement Tests Notes

Objective:

- The objective of this experiment was to reproduce a temperature measurement of shocked CCl₄ using a Stoke-anti-Stoke Raman measurement. The earlier measurement was done by Pangilinan and Gupta [24].

Experiment:

- Figure 110 shows schematic view (not to scale) of the target configuration. The impact velocity and the sample thickness were same as Experiments #4 and #5 (12 GPa) described in Ref. 1. The pump laser (514.5 nm wavelength, 65 mJ pulse) was focused using a pair of 24 mm focal length lenses (12 mm diameter) to produce 400 μm spot size. Raman scattered photons were collected using a pair of 18 mm focal length lenses at 45 degrees angle.
- Raman signals were recorded using detection system consisting of a spectrometer (Kaiser HoloSpec spectrometer with HSG-514.5 grating, 250 μm slit), streak camera (Imacon 500), image intensifier (Photek MCP140), and CCD (Princeton Instruments 1340x1300).

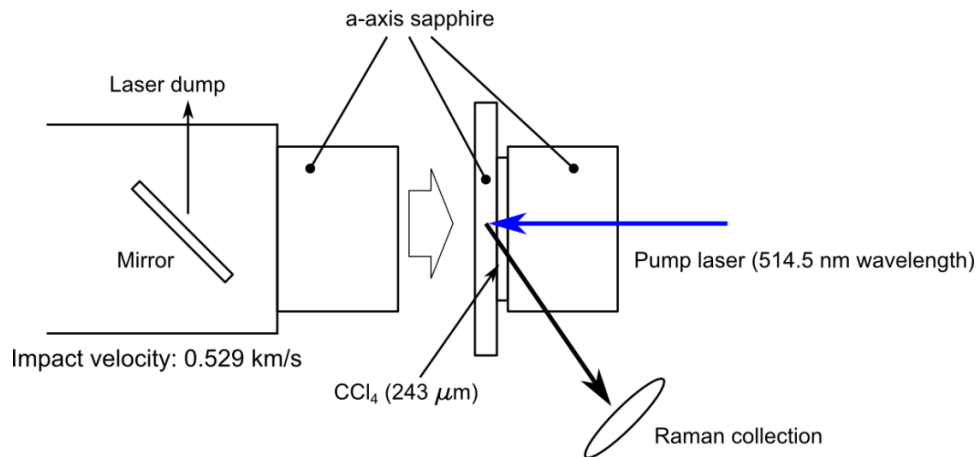


Figure 110. Schematic view of the experimental configuration (not to scale). The impact velocity and the cell thickness were same as the Pangilinan and Gupta's 12 GPa experiment [24].

Results:

- Figure 111 shows time-resolved Raman spectra obtained every 50 ns. Both the shifts and the intensity changes in Raman peaks were observed. The sample reached peak pressure ~ 600 ns after impact. Qualitatively, Figure 111 agreed well with the results presented in Ref. [24]. The three main Stoke/anti-Stoke peaks correspond to 460 cm^{-1} , 314 cm^{-1} and 217 cm^{-1} modes, respectively.
- Shifts in Raman peaks and inferred temperatures were calculated using a method described by Pangilinan and Gupta [24] and provided in Table 14. The error bars were also determined using the same approach described in Ref. [24]. Because of the perturbation from a notch filter on the 217 cm^{-1} mode peak, only 460 cm^{-1} and 314 cm^{-1} modes were used to determine the temperature.
- The result from this experiment agreed with the earlier measurements made by Pangilinan and Gupta [24] within experimental uncertainty, as expected (Table 14).

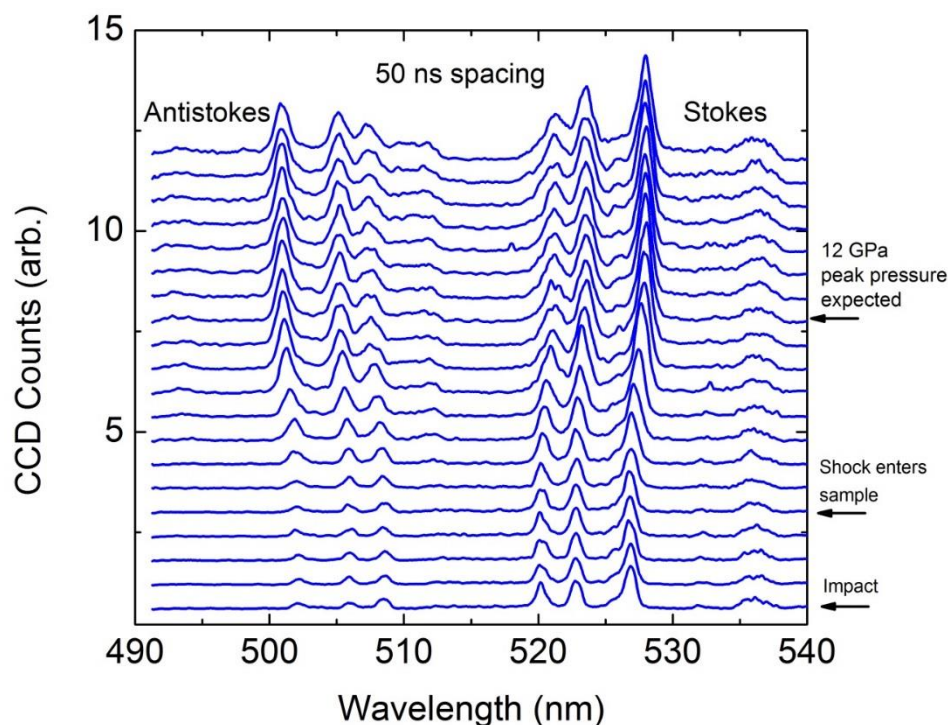


Figure 111. Time resolved CCl_4 Raman spectra (50 ns spacing).

Table 14. Experimental results

Expt.	Sample thickness (μm)	Impact velocity (m/s)	Peak pressure (GPa)	Frequency shift (cm^{-1})		Inferred temperature (K)	
				314 mode	460 mode	314 mode	460 mode
This (17-502)	243	529	12.1	29 ± 5	41 ± 5	819 ± 130	843 ± 86
(95-010) [24]	250	531	12.1	-	33 ± 9	-	728 ± 78
(96-041) [24]	254	530	12.1	28 ± 9	40 ± 9	848 ± 170	883 ± 90

VIII. REFERENCES

- [1] P. J. Rae, H. T. Goldrein, S. J. P. Palmer, J. E. Field, and A. L. Lewis, *Proc. R. Soc. a-Mathematical Phys. Eng. Sci.* **458**, 743 (2002).
- [2] M. M. Chaudhri and J. E. Field, *Proc. R. Soc. London* **340**, 113 (1974).
- [3] J. E. Field, *Acc. Chem. Res.* **25**, 489 (1992).
- [4] J. E. Field, N. K. Bourne, S. J. P. Palmer, S. M. Walley, and J. M. Smallwood, *Philos. Trans. R. Soc. London-Mathematical Phys. Eng. Sci.* **339**, 269 (1992).
- [5] A. M. Mellor, D. A. Wiegand, and K. B. Isom, *Struct. Prop. Energ. Mater.* **296**, 293 (1993).
- [6] R. E. Winter and E. A. Faber, *Proc. R. Soc. London Ser. A* **343**, 399 (1975).
- [7] Y. Q. Wu and F. L. Huang, *Mech. Mater.* **43**, 835 (2011).
- [8] R. Pokharel, J. Lind, A. K. Kanjarla, R. A. Lebensohn, S. F. Li, P. Kenesei, R. M. Suter, and A. D. Rollett, *Annu. Rev. Condens. Matter Phys.* **5**, 317 (2014).
- [9] Q. An, W. A. Goddard, S. V Zybin, A. Jaramillo-Botero, and T. T. Zhou, *J. Phys. Chem. C* **117**, 26551 (2013).
- [10] Y. A. Gruzdkov and Y. M. Gupta, *J. Phys. Chem. A* **105**, 6197 (2001).
- [11] Y. M. Gupta, *J. Phys. IV* **5**, 345 (1995).
- [12] J. E. Field, G. M. Swallowe, and S. N. Heavens, *Proc. R. Soc. London Ser. A* **382**, 231 (1982).
- [13] M. W. Chen, S. You, K. S. Suslick, and D. D. Dlott, *Rev. Sci. Instrum* **85**, 23705 (2014).
- [14] M. W. Chen, S. You, K. S. Suslick, and D. D. Dlott, *App. Phys. Lett.* **104**, 61907 (2014).
- [15] et al. K.E. Brown, *J. Appl. Phys* **112**, (2012).
- [16] A. A. Banishev, *J Appl Phys* **115**, (2014).
- [17] B. J. Jensen, S. N. Luo, D. E. Hooks, K. Fezzaa, K. J. Ramos, J. D. Yeager, K. Kwiatkowski, T. Shimada, and D. M. Dattelbaum, *AIP Adv.* **2**, (2012).
- [18] B. J. Jensen, K. J. Ramos, A. J. Iverson, J. Bernier, C. A. Carlson, J. D. Yeager, K. Fezzaa, and D. E. Hooks, *J. Phys. Conf. Ser.* **500**, 42001 (2014).
- [19] K. J. Ramos, *J. Phys. Conf. Ser.* **500**, (2014).
- [20] P. B. Glover, A. P. Bassett, P. Nockemann, B. M. Kariuki, R. Van Deun, and Z. Pikramenou, *Chem. Eur. J.* **13**, 6308 (2007).
- [21] M. Latva, H. Takalo, V.-M. Mukkala, C. Matachescu, J. C. Rodriguez-Ubis, and J. Kankare, *J. Lumin.* **75**, 149 (1997).
- [22] B. R. Anderson, R. Gunawidjaja, and H. Eilers, *J. Lumin* **188**, 245 (2017).
- [23] B. R. Anderson, R. Gunawidjaja, and H. Eilers, *App. Phys. B* **123**, 62 (2017).

-
- [24] G. I. Pangilinan and Y. M. Gupta, *J. Appl. Phys.* **81**, 6662 (1997).
- [25] B. R. Anderson, N. Gese, R. Gunawidjaja, and H. Eilers, in *Front. Opt.* (2016), p. FF5B.4.
- [26] B. R. Anderson, N. Gese, R. Gunawidjaja, and H. Eilers, Under Rev. (n.d.).
- [27] R. Gunawidjaja, B. R. Anderson, H. D. y Riega, and H. Eilers, *AIP Conf. Proc.* **1793**, 60014 (2017).
- [28] A. L. Heyes, S. Seefeldt, and J. P. Feist, *Opt. Laser Technol.* **38**, 257 (2006).
- [29] A. H. Khalid and K. Kontis, *Sensors* **8**, 5673 (2008).
- [30] G. P. Goss, A. A. Smith, and M. E. Post, *Rev. Sci. Instruments* **60**, 12 (1989).
- [31] M. R. Cates, S. W. Allison, S. L. Jaiswal, and D. L. Beshears, in *49th Int. Instrum. Symp. -- Instrumentation, Syst. Autom. Soc.* (Orlando, FL, 2003).
- [32] S.W., Allison, and G. T. Gillies, *Rev. Sci. Instruments* **68**, 2615 (1997).
- [33] K. Kontis, *Aeronaut. J.* **3162**, 495 (2007).
- [34] X. Xu, X. Sun, H. Liu, J.-G. Li, X. Li, D. Huo, and S. Liu, *J. Am. Ceram. Soc.* **95**, 3821 (2012).
- [35] D. J. L. L. Mengjiao Xu Luxiang Wang, *Mater. Res. Bull.* **70**, 691 (2015).
- [36] Y. S. X. X. X. D. W. Y. J. W. Dan Li Qianli Ma and G. Liu, *Phys. Chem. Chem. Phys.* **18**, 27536 (2016).